



Universiteit Gent  
Faculteit Wetenschappen  
Vakgroep Fysica en Sterrenkunde

<sup>2</sup> No title yet

<sup>3</sup> No sub-title neither, obviously...

---

<sup>4</sup> Alexis Fagot

5



Thesis to obtain the degree of  
Doctor of Philosophy in Physics  
Academic years 2012-2017





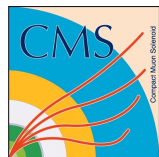


Universiteit Gent  
Faculteit Wetenschappen  
Vakgroep Fysica en Sterrenkunde

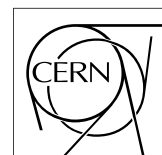
Promotoren: Dr. Michael Tytgat  
Prof. Dr. Dirk Ryckbosch

Universiteit Gent  
Faculteit Wetenschappen  
Vakgroep Fysica en Sterrenkunde  
Proeftuinstraat 86, B-9000 Gent, België  
Tel.: +32 9 264.65.28  
Fax.: +32 9 264.66.97

17



Thesis to obtain the degree of  
Doctor of Philosophy in Physics  
Academic years 2012-2017





## Acknowledgements

<sup>19</sup> Ici on remerciera tous les gens que j'ai pu croiser durant cette aventure et qui m'ont permis de passer  
<sup>20</sup> un bon moment

<sup>21</sup> *Gent, ici la super date de la mort qui tue de la fin d'écriture*  
<sup>22</sup> *Alexis Fagot*



# Table of Contents

24	<b>Acknowledgements</b>	i
25	<b>Nederlandse samenvatting</b>	vii
26	<b>English summary</b>	ix
27	<b>1 Introduction</b>	1-1
28	1.1 A story of High Energy Physics . . . . .	1-1
29	1.2 Organisation of this study . . . . .	1-1
30	<b>2 Investigating the TeV scale</b>	2-1
31	2.1 The Standard Model of Particle Physics . . . . .	2-2
32	2.1.1 A history of particle physics . . . . .	2-2
33	2.1.2 Construction and test of the model [TO SEE IF KEPT - MAYBE TOO COMPLEX] . . . . .	2-10
34	2.1.3 Investigating the TeV scale . . . . .	2-10
35	2.2 The Large Hadron Collider & the Compact Muon Solenoid . . . . .	2-10
36	2.2.1 LHC, the most powerful particle accelerator . . . . .	2-11
37	2.2.1.1 Particle acceleration . . . . .	2-12
38	2.2.1.2 LHC discoveries and LHC physics program . . . . .	2-15
39	2.2.1.3 High Luminosity LHC . . . . .	2-16
40	2.2.2 CMS, a multipurpose experiment . . . . .	2-16
41	2.3 Muon Phase-II Upgrade . . . . .	2-16
42		
43	<b>3 Physics of Resistive plate chambers</b>	3-1
44	3.1 Principle . . . . .	3-1
45	3.1.1 Electron drift velocity . . . . .	3-4
46	3.2 Rate capability and time resolution of Resistive Plate Chambers . . . . .	3-4
47	3.2.1 Operation modes . . . . .	3-4
48	3.2.2 Detector designs and performance . . . . .	3-6
49	3.2.2.1 Double-gap RPC . . . . .	3-7
50	3.2.2.2 Multigap RPC (MRPC) . . . . .	3-8
51	3.2.2.3 Charge distribution and performance limitations . . . . .	3-9
52	3.3 Signal formation . . . . .	3-12
53	3.4 Gas transport parameters . . . . .	3-12
54	<b>4 Longevity studies and Consolidation of the present CMS RPC subsystem</b>	4-1
55	4.1 Resistive Plate Chambers at CMS . . . . .	4-1
56	4.1.1 Overview . . . . .	4-1
57	4.1.2 The present RPC system . . . . .	4-2
58	4.1.3 Pulse processing of CMS RPCs . . . . .	4-3

---

59	4.2	Testing detectors under extreme conditions . . . . .	4-4
60	4.2.1	The Gamma Irradiation Facilities . . . . .	4-7
61	4.2.1.1	GIF . . . . .	4-7
62	4.2.1.2	GIF++ . . . . .	4-9
63	4.3	Preliminary tests at GIF . . . . .	4-11
64	4.3.1	Resistive Plate Chamber test setup . . . . .	4-11
65	4.3.2	Data Acquisition . . . . .	4-13
66	4.3.3	Geometrical acceptance of the setup layout to cosmic muons . . . . .	4-13
67	4.3.3.1	Description of the simulation layout . . . . .	4-14
68	4.3.3.2	Simulation procedure . . . . .	4-16
69	4.3.3.3	Results . . . . .	4-17
70	4.3.4	Photon flux at GIF . . . . .	4-17
71	4.3.4.1	Expectations from simulations . . . . .	4-17
72	4.3.4.2	Dose measurements . . . . .	4-22
73	4.3.5	Results and discussions . . . . .	4-23
74	4.4	Longevity tests at GIF++ . . . . .	4-24
75	4.4.1	Description of the Data Acquisition . . . . .	4-27
76	4.4.2	RPC current, environmental and operation parameter monitoring . . . . .	4-28
77	4.4.3	Measurement procedure . . . . .	4-29
78	4.4.4	Longevity studies results . . . . .	4-29
79	<b>5</b>	<b>Investigation on high rate RPCs</b>	<b>5-1</b>
80	5.1	Rate limitations and ageing of RPCs . . . . .	5-1
81	5.1.1	Low resistivity electrodes . . . . .	5-1
82	5.1.2	Low noise front-end electronics . . . . .	5-1
83	5.2	Construction of prototypes . . . . .	5-1
84	5.3	Results and discussions . . . . .	5-1
85	<b>6</b>	<b>Conclusions and outlooks</b>	<b>6-1</b>
86	6.1	Conclusions . . . . .	6-1
87	6.2	Outlooks . . . . .	6-1
88	<b>A</b>	<b>A data acquisition software for CAEN VME TDCs</b>	<b>A-1</b>
89	A.1	GIF++ DAQ file tree . . . . .	A-1
90	A.2	Usage of the DAQ . . . . .	A-2
91	A.3	Description of the readout setup . . . . .	A-3
92	A.4	Data read-out . . . . .	A-3
93	A.4.1	V1190A TDCs . . . . .	A-4
94	A.4.2	DataReader . . . . .	A-6
95	A.4.3	Data quality flag . . . . .	A-10
96	A.5	Communications . . . . .	A-12
97	A.5.1	V1718 USB Bridge . . . . .	A-13
98	A.5.2	Configuration file . . . . .	A-13
99	A.5.3	WebDCS/DAQ intercommunication . . . . .	A-17
100	A.5.4	Example of inter-process communication cycle . . . . .	A-18
101	A.6	Software export . . . . .	A-18

---

102	<b>B Details on the offline analysis package</b>	<b>B-1</b>
103	B.1 GIF++ Offline Analysis file tree . . . . .	B-1
104	B.2 Usage of the Offline Analysis . . . . .	B-2
105	B.2.1 Output of the offline tool . . . . .	B-3
106	B.2.1.1 ROOT file . . . . .	B-3
107	B.2.1.2 CSV files . . . . .	B-5
108	B.3 Analysis inputs and information handling . . . . .	B-6
109	B.3.1 Dimensions file and IniFile parser . . . . .	B-6
110	B.3.2 TDC to RPC link file and Mapping . . . . .	B-7
111	B.4 Description of GIF++ setup within the Offline Analysis tool . . . . .	B-9
112	B.4.1 RPC objects . . . . .	B-9
113	B.4.2 Trolley objects . . . . .	B-10
114	B.4.3 Infrastructure object . . . . .	B-11
115	B.5 Handeling of data . . . . .	B-12
116	B.5.1 RPC hits . . . . .	B-13
117	B.5.2 Clusters of hits . . . . .	B-14
118	B.6 DAQ data Analysis . . . . .	B-15
119	B.6.1 Determination of the run type . . . . .	B-16
120	B.6.2 Beam time window calculation for efficiency runs . . . . .	B-17
121	B.6.3 Data loop and histogram filling . . . . .	B-18
122	B.6.4 Results calculation . . . . .	B-19
123	B.6.4.1 Rate normalisation . . . . .	B-19
124	B.6.4.2 Rate and activity . . . . .	B-21
125	B.6.4.3 Strip masking tool . . . . .	B-23
126	B.6.4.4 Output CSV files filling . . . . .	B-25
127	B.7 Current data Analysis . . . . .	B-29



<sup>128</sup>

## Nederlandse samenvatting –Summary in Dutch–

<sup>129</sup>

<sup>130</sup> Le resume en Neerlandais (j'aurais peut-être pu apprendre la langue juste pour ça...).



<sup>131</sup>

## English summary

<sup>132</sup> Le meme résume mais en Anglais (on commencera par la hein!).



# List of Figures

133

134	2.1	Through the gold foil experiment Rutherford could show that most of the mass of atoms was contained in a positively charged nucleus and could then propose a more accurate atomic model than that of Thomson. . . . .	2-3
135			
136	2.2	Figure 2.2a: Meson octet. Figure 2.2b: Baryon octet. Figure 2.2c: Baryon decuplet. . .	2-9
137			
138	2.3	CERN accelerator complex. . . . .	2-12
139			
140	2.4	Pictures of the different accelerators. From top to bottom: first the LINAC 2 and the <i>Pb</i> source of LINAC 3. Then the Booster and the LEIR. Finally, the PS, the SPS and the LHC. . . . .	2-14
141			
142	2.5	Figure 2.5a: schematics of the LHC cryodipoles. 1: Superconducting Coils, 2: Beam pipe, 3: Heat exchanger Pipe, 4: Helium-II Vessel, 5: Superconducting Bus-bar, 6: Iron Yoke, 7: Non-Magnetic Collars, 8: Vacuum Vessel, 9: Radiation Screen, 10: Thermal Shield, 11: Auxiliary Bus-bar Tube, 12: Instrumentation Feed Throughs, 13: Protection Diode, 14: Quadrupole Bus-bars, 15: Spool Piece Bus-bars. Figure 2.5b: magnetic field and resulting motion force applied on the beam particles. . .	2-15
143			
144	2.6	Figure 2.6a: picture of the LHC quadrupoles. Figure 2.6b: magnetic fields and resulting focussing force applied on the beam by 2 consecutive quadrupoles. . . . .	2-15
145			
150	2.7	Absorbed dose in the CMS cavern after an integrated luminosity of 3000 fb. R is the transverse distance from the beamline and Z is the distance along the beamline from the Interaction Point at Z=0. . . . .	2-16
151			
152	2.8	A quadrant of the muon system, showing DTs (yellow), RPCs (light blue), and CSCs (green). The locations of new forward muon detectors for Phase-II are contained within the dashed box and indicated in red for GEM stations (ME0, GE1/1, and GE2/1) and dark blue for improved RPC (iRPC) stations (RE3/1 and RE4/1). . . . .	2-17
153			
154	2.9	RMS of the multiple scattering displacement as a function of muon $p_T$ for the proposed forward muon stations. All of the electromagnetic processes such as bremsstrahlung and magnetic field effect are included in the simulation. . . . .	2-18
155			
156			
157	3.1	Different phases of the avalanche development in the RPC gas volume subjected to a constant electric field $E_0$ . a) An avalanche is initiated by the primary ionisation caused by the passage of a charged particle through the gas volume. b) Due to its growing size, the avalanche starts to locally influence the electric field. c) The electrons, lighter than the cations reach the anode first. d) The ions reach the cathode. While the charges have not recombined, the electric field in the small region around the avalanche stays affected and locally blind the detector. . . . .	3-2
158			
159	3.2	Effeciency (circles and stars with 30 mV and 100 mV thresholds respectively) and streamer probability (opened circles) as function of the operating voltatge of a 2 mm single gap HPL RPC flushed with a gas mixture containing (a) 5%, (b) 2%, (c) 1% and (d) no $SF_6$ [33]. . . . .	3-3
160			
161			
162			
163			
164			
165			
166			
167			
168			
169			
170			

171	3.3 Movement of the charge carriers in an RPC. Figure 3.3a: Voltage across an RPC whose electrode have a relative permittivity of 5 at the moment the tension s applied. Figure 3.3b: After the charge carriers moved, the electrodes are charged and there is no voltage drop over the electrodes anymore. The full potential is applied on the gas gap only. Figure 3.3c: The streamer discharge initiated by a charged particle transports electrons and cations towards the anode and cathode respectively. . . . .	3-5
172		
173		
174		
175		
176		
177	3.4 Typical oscilloscope pulses in streamer mode (Figure 3.4a) and avalanche mode(Figure 3.4b). In the case of streamer mode, the very small avalanche signal is visible. . . . .	3-5
178		
179		
180		
181		
182	3.5 Rate capability comparison for the streamer and avalanche mode of operation. An order of magnitude in rate capability for a maximal efficiency drop of 10% is gained by using the avalanche mode over the streamer mode. . . . .	3-6
183		
184		
185		
186		
187		
188	3.6 Possible double-gap RPC layouts: a) "standard" 1D double-gap RPC, as used in CMS experiment, where the anodes are facing each other and a 1D read-out plane is sandwiched in between them, b) double read-out double-gap RPC as used in AT-LAS experiment, where the cathodes are facing each other and 2 read-out planes are used on the outer surfaces. This last layout can offer the possibility to use a 2D reconstruction by using orthogonal read-out planes. . . . .	3-7
189		
190		
191	3.7 Comparison of performance of CMS double and single gap RPCs using cosmic muons [44]. Figure 3.7a: Comparison of efficiency sigmoids. Figure 3.7b: Voltage distribution at 95% of maximum efficiency. Figure 3.7c: $\Delta_{10\%}^{90\%}$ distribution. . . .	3-7
192		
193		
194		
195	3.8 Presentation of ALICE MRPC using 250 $\mu\text{m}$ gas gaps, 620 $\mu\text{m}$ outer glass electrodes and 550 $\mu\text{m}$ inner floating electrodes. More details on the labels are given in [45]. . .	3-8
196		
197		
198	3.9 Particle identification applied to electrons in the STAR experiment. The identification is performed combining ToF and $dE/dx$ measurements [50]. . . . .	3-9
199		
200		
201	3.10 Comparison of the detector performance of ALICE ToF MRPC [51] at fixed applied voltage (in blue) and at fixed effective voltage (in red). The effective voltage is kept fixed by increasing the applied voltage accordingly to the current drawn by the detector.	3-9
202		
203		
204		
205	3.11 Ratio between total induced and drifting charge have been simulated for single gap, double-gap and multigap layouts [52]. The total induced charge for a double-gap RPC is a factor 2 higher than for a multigap. . . . .	3-10
206		
207		
208	3.12 Charge spectra have been simulated for single gap, double-gap and multigap layouts [52]. It appears that when single gap shows a decreasing spectrum, double and multigap layouts exhibit a spectrum whose peak is detached from the origin. The detachment gets stronger as the number of gaps increases. . . . .	3-11
209		
210		
211		
212	3.13 The maximal theoretical efficiency is simulated for single gap, double-gap and multi-gap layouts [52] at a constant gap thickness of 2 mm and using an effective Townsend coefficient of 9 $\text{mm}^{-1}$ . . . . .	3-11
213		
214		
215		
216		
217		
218		
219		
220		
221		
222		
223		
224		
225		
226		
227		
228		
229		
230		
231		
232		
233		
234		
235		
236		
237		
238		
239		
240		
241		
242		
243		
244		
245		
246		
247		
248		
249		
250		
251		
252		
253		
254		
255		
256		
257		
258		
259		
260		
261		
262		
263		
264		
265		
266		
267		
268		
269		
270		
271		
272		
273		
274		
275		
276		
277		
278		
279		
280		
281		
282		
283		
284		
285		
286		
287		
288		
289		
290		
291		
292		
293		
294		
295		
296		
297		
298		
299		
300		
301		
302		
303		
304		
305		
306		
307		
308		
309		
310		
311		
312		
313		
314		
315		
316		
317		
318		
319		
320		
321		
322		
323		
324		
325		
326		
327		
328		
329		
330		
331		
332		
333		
334		
335		
336		
337		
338		
339		
340		
341		
342		
343		
344		
345		
346		
347		
348		
349		
350		
351		
352		
353		
354		
355		
356		
357		
358		
359		
360		
361		
362		
363		
364		
365		
366		
367		
368		
369		
370		
371		
372		
373		
374		
375		
376		
377		
378		
379		
380		
381		
382		
383		
384		
385		
386		
387		
388		
389		
390		
391		
392		
393		
394		
395		
396		
397		
398		
399		
400		
401		
402		
403		
404		
405		
406		
407		
408		
409		
410		
411		
412		
413		
414		
415		
416		
417		
418		
419		
420		
421		
422		
423		
424		
425		
426		
427		
428		
429		
430		
431		
432		
433		
434		
435		
436		
437		
438		
439		
440		
441		
442		
443		
444		
445		
446		
447		
448		
449		
450		
451		
452		
453		
454		
455		
456		
457		
458		
459		
460		
461		
462		
463		
464		
465		
466		
467		
468		
469		
470		
471		
472		
473		
474		
475		
476		
477		
478		
479		
480		
481		
482		
483		
484		
485		
486		
487		
488		
489		
490		
491		
492		
493		
494		
495		
496		
497		
498		
499		
500		
501		
502		
503		
504		
505		
506		
507		
508		
509		
510		
511		
512		
513		
514		
515		
516		
517		
518		
519		
520		
521		
522		
523		
524		
525		
526		
527		
528		
529		
530		
531		
532		
533		
534		
535		
536		
537		
538		
539		
540		
541		
542		
543		
544		
545		

212	4.2	Description of the principle of a CFD. A comparison of threshold triggering (left) 213 and constant fraction triggering (right) is shown in Figure 4.2a. Constant fraction 214 triggering is obtained thanks to zero-crossing technique as explained in Figure 4.2b. 215 The signal arriving at the input of the CFD is split into three components. A first 216 one is delayed and connected to the inverting input of a first comparator. A sec- 217 ond component is connected to the noninverting input of this first comparator. A 218 third component is connected to the noninverting input of another comparator along 219 with a threshold value connected to the inverting input. Finally, the output of both 220 comparators is fed through an AND gate. . . . .	4-4
221	4.3	(4.3a) Extrapolation from 2016 data of single hit rate per unit area in the barrel 222 region. (4.3b) Extrapolation from 2016 data of single hit rate per unit area in the 223 endcap region. . . . .	4-6
224	4.4	Background Fluka simulation compared to 2016 Data at $L = 10^{34} \text{ cm}^{-2} \cdot \text{s}^{-1}$ in 225 the fourth endcap disk region. A mismatch in between simulation and data can be 226 observed. [To be understood.] . . . . .	4-7
227	4.5	Layout of the test beam zone called X5c GIF at CERN. Photons from the radioactive 228 source produce a sustained high rate of random hits over the whole area. The zone is 229 surrounded by 8 m high and 80 cm thick concrete walls. Access is possible through 230 three entry points. Two access doors for personnel and one large gate for material. 231 A crane allows installation of heavy equipment in the area. . . . .	4-8
232	4.6	$^{137}\text{Cs}$ decays by $\beta^-$ emission to the ground state of $^{137}\text{Ba}$ (BR = 5.64%) and via the 233 662 keV isomeric level of $^{137}\text{Ba}$ (BR = 94.36%) whose half-life is 2.55 min. . . . .	4-9
234	4.7	Floor plan of the GIF++ facility. When the facility downstream of the GIF++ takes 235 electron beam, a beam pipe is installed along the beam line (z-axis). The irradiator 236 can be displaced laterally (its center moves from $x = 0.65$ m to 2.15 m), to increase 237 the distance to the beam pipe. . . . .	4-9
238	4.8	Simulated unattenuated current of photons in the xz plane (Figure 4.8a) and yz plane 239 (Figure 4.8b) through the source at $x = 0.65$ m and $y = 0$ m. With angular correction 240 filters, the current of 662 keV photons is made uniform in xy planes. . . . .	4-10
241	4.9	Description of the RPC setup. Dimensions are given in mm. A tent containing RPCs 242 is placed at 1720 mm from the source container. The source is situated in the center 243 of the container. RE-4-2-BARC-161 chamber is 160 mm inside the tent. This way, 244 the distance between the source and the chambers plan is 2060 mm. Figure 4.9a 245 provides a side view of the setup in the xz plane while Figure 4.9b shows a top view 246 in the yz plane. . . . .	4-11
247	4.10	RE-4-2-BARC-161 chamber is inside the tent as described in Figure 4.9. In the top 248 right, the two scintillators used as trigger can be seen. This trigger system has an 249 inclination of 10° relative to horizontal and is placed above half-partition B2 of the 250 RPCs. PMT electronics are shielded thanks to lead blocks placed in order to protect 251 them without stopping photons from going through the scintillators and the chamber.	4-12
252	4.11	Hit distributions over all 3 partitions of RE-4-2-BARC-161 chamber is showed on 253 these plots. Top, middle and bottom figures respectively correspond to partitions A, 254 B, and C. These plots show that some events still occur in other half-partitions than 255 B2, which corresponds to strips 49 to 64, in front of which the trigger is placed, con- 256 tributing to the inefficiency of detection of cosmic muons. In the case of partitions 257 A and C, the very low amount of data can be interpreted as noise. On the other hand, 258 it is clear that a little portion of muons reach the half-partition B1, corresponding to 259 strips 33 to 48. . . . .	4-13

260	4.12 Results are derived from data taken on half-partition B2 only. On the 18 <sup>th</sup> of June 261 data has been taken on chamber RE-2-BARC-161 at building 904 (Prevessin 262 Site) with cosmic muons providing us a reference efficiency plateau of $(97.54 \pm$ 263 $0.15)\%$ represented by a black curve. A similar measurement has been done at GIF 264 on the 21 <sup>st</sup> of July with the same chamber giving a plateau of $(78.52 \pm 0.94)\%$ 265 represented by a red curve. . . . .	4-14
266	4.13 Representation of the layout used for the simulations of the test setup. The RPC is 267 represented as a yellow trapezoid while the two scintillators as blue cuboids looking 268 at the sky. A green plane corresponds to the muon generation plane within the sim- 269 ulation. Figure 4.9a shows a global view of the simulated setup. Figure 4.9b shows 270 a zommed view that allows to see the 2 scintillators as well as the full RPC plane. . . . .	4-15
271	4.14 $\gamma$ flux $F(D)$ is plot using values from table 4.1. As expected, the plot shows similar 272 attenuation behaviours with increasing distance for each absorption factors. . . . .	4-18
273	4.15 Figure 4.15a shows the linear approximation fit done via formulae 4.7 on data from 274 table 4.2. Figure 4.15b shows a comparison of this model with the simulated flux 275 using a and b given in figure 4.15a in formulae 4.4 and the reference value $D_0 =$ 276 $50\text{cm}$ and the associated flux for each absorption factor $F_0^{ABS}$ from table 4.1 . . . . .	4-20
277	4.16 Dose measurements has been done in a plane corresponding to the tents front side. 278 This plan is 1900 mm away from the source. As explained in the first chapter, a 279 lens-shaped lead filter provides a uniform photon flux in the vertical plan orthogonal 280 to the beam direction. If the second line of measured fluxes is not taken into account 281 because of lower values due to experimental equipments in the way between the 282 source and the tent, the uniformity of the flux is well showed by the results. . . . .	4-22
283	4.17 . . . . .	4-23
284	4.18 Evolution of the maximum efficiency for RE2 (4.18a) and RE4 (4.18b) chambers 285 with increasing extrapolated $\gamma$ rate per unit area at working point. Both irradiated 286 (blue) and non irradiated (red) chambers are shown. . . . .	4-25
287	4.19 Evolution of the working point for RE2 (4.19a) and RE4 (4.19b) with increasing 288 extrapolated $\gamma$ rate per unit area at working point. Both irradiated (blue) and non 289 irradiated (red) chambers are shown. . . . .	4-25
290	4.20 Evolution of the maximum efficiency at HL-LHC conditions, i.e. a background hit 291 rate per unit area of $300\text{Hz/cm}^2$ , with increasing integrated charge for RE2 (4.20a) 292 and RE4 (4.20b) detectors. Both irradiated (blue) and non irradiated (red) chambers 293 are shown. The integrated charge for non irradiated detectors is recorded during test 294 beam periods and stays small with respect to the charge accumulated in irradiated 295 chambers. . . . .	4-26
296	4.21 Comparison of the efficiency sigmoid before (triangles) and after (circles) irradiation 297 for RE2 (4.21a) and RE4 (4.21b) detectors. Both irradiated (blue) and non irradiated 298 (red) chambers are shown. . . . .	4-26
299	4.22 Evolution of the Bakelite resistivity for RE2 (4.22a) and RE4 (4.22b) detectors. Both 300 irradiated (blue) and non irradiated (red) chambers are shown. . . . .	4-27
301	4.23 Evolution of the noise rate per unit area for the irradiated chamber RE2-2-BARC-9 302 only. . . . .	4-27
303	A.1 (A.1a) View of the front panel of a V1190A TDC module [58]. (A.1b) View of the 304 front panel of a V1718 Bridge module [59]. (A.1c) View of the front panel of a 6U 305 6021 VME crate [60]. . . . .	A-3
306	A.2 Module V1190A <i>Trigger Matching Mode</i> timing diagram [58]. . . . .	A-4

307	A.3 Structure of the ROOT output file generated by the DAQ. The 5 branches ( <code>EventNumber</code> ,	
308	<code>number_of_hits</code> , <code>Quality_flag</code> , <code>TDC_channel</code> and <code>TDC_TimeStamp</code> ) are visible on	
309	the left panel of the ROOT browser. On the right panel is visible the histogram cor-	
310	responding to the variable <code>nHits</code> . In this specific example, there were approximately	
311	50k events recorded to measure the gamma irradiation rate on the detectors. Each	
312	event is stored as a single entry in the <code>TTree</code> . . . . .	A-10
313	A.4 The effect of the quality flag is explained by presenting the content of <code>TBranch</code>	
314	<code>number_of_hits</code> of a data file without <code>Quality_flag</code> in Figure A.4a and the con-	
315	tent of the same <code>TBranch</code> for data corresponding to a <code>Quality_flag</code> where all TDCs	
316	were labelled as <code>GOOD</code> in Figure A.4b taken with similar conditions. It can be noted	
317	that the number of entries in Figure A.4b is slightly lower then in Figure A.4a due	
318	to the excluded events. . . . .	A-12
319	A.5 Using the same data as previously showed in Figure A.4, the effect of the quality	
320	flag is explained by presenting the reconstructed hit multiplicity of a data file with-	
321	out <code>Quality_flag</code> in Figure A.5a and the reconstructed content of the same RPC	
322	partition for data corresponding to a <code>Quality_flag</code> where all TDCs were labelled as	
323	<code>GOOD</code> in Figure A.5b taken with similar conditions. The artificial high content of bin	
324	0 is completely suppressed. . . . .	A-12
325	A.6 WebDCS DAQ scan page. On this page, shifters need to choose the type of scan	
326	(Rate, Efficiency or Noise Reference scan), the gamma source configuration at the	
327	moment of data taking, the beam configuration, and the trigger mode. These in-	
328	formation will be stored in the DAQ ROOT output. Are also given the minimal	
329	measurement time and waiting time after ramping up of the detectors is over before	
330	starting the data acquisition. Then, the list of HV points to scan and the number of	
331	triggers for each run of the scan are given in the table underneath. . . . .	A-14
332	B.1 Example of expected hit time distributions in the cases of efficiency (Figure B.1a)	
333	and noise/gamma rate per unit area (Figure B.1b) measurements as extracted from	
334	the raw ROOT files. The unit along the x-axis corresponds to ns. The fact that	
335	"the" muon peak is not well defined in Figure B.1a is due to the contribution of all	
336	the RPCs being tested at the same time that don't necessarily have the same signal	
337	arrival time. Each individual peak can have an offset with the ones of other detectors.	
338	The inconsistancy in the first 100 ns of both time distributions is an artefact of the	
339	TDCs and are systematically rejected during the analysis. . . . .	B-16
340	B.2 The effect of the quality flag is explained by presenting the reconstructed hit multi-	
341	plicity of a data file without <code>Quality_flag</code> . The artificial high content of bin 0 is the	
342	effect of corrupted data. . . . .	B-19
343	B.3 Display of the masking tool page on the webDCS. The window on the left allows the	
344	shifter to edit <code>ChannelsMapping.csv</code> . To mask a channel, it only is needed to set the	
345	3rd field corresponding to the strip to mask to 0. It is not necessary for older mapping	
346	file formats to add a 1 for each strip that is not masked as the code is versatile and	
347	the default behaviour is to consider missing mask fields as active strips. The effect	
348	of the mask is directly visible for noisy channels as the corresponding bin turns red.	
349	The global effect of masking strips will be an update of the rate value showed on the	
350	histogram that will take into consideration the rejected channels. . . . .	B-24



# List of Tables

351

352	3.1	Properties of the most used electrode materials for RPCs. . . . .	3-4
353	4.1	Total photon flux ( $E\gamma \leq 662$ keV) with statistical error predicted considering a $^{137}\text{Cs}$ activity of 740 GBq at different values of the distance $D$ to the source along the x-axis of irradiation field [55]. . . . .	4-17
354	4.2	Correction factor $c$ is computed thanks to formulae 4.5 taking as reference $D_0 = 50$ cm and the associated flux $F_0^{ABS}$ for each absorption factor available in table 4.1.	4-19
355	4.3	The data at $D_0$ in 1997 is taken from [55]. In a second step, using Equations 4.8 and 4.9, the flux at $D$ can be estimated in 1997. Then, taking into account the attenuation of the source activity, the flux at $D$ can be estimated at the time of the tests in GIF in 2014. Finally, assuming a sensitivity of the RPC to $\gamma$ $s = 2 \cdot 10^{-3}$ , an estimation of the hit rate per unit area is obtained. . . . .	4-21
363	A.1	Inter-process communication cycles in between the webDCS and the DAQ through file string signals. . . . .	A-19
364			



# List of Acronyms

365

366

## List of Acronyms

367

368

### A

369

370

371 AFL

Almost Full Level

372

373

### B

374

375

376 BARC

Bhabha Atomic Research Centre

377 BLT

Block Transfer

378 BNL

Brookhaven National Laboratory

379 BR

Branching Ratio

380

381

### C

382

383

384 CAEN

Costruzioni Apparecchiature Elettroniche Nucleari S.p.A.

385 CERN

European Organization for Nuclear Research

386 CFD

Constant Fraction Discriminator

387 CMS

Compact Muon Solenoid

388 CSC

Cathode Strip Chamber

389

390

### D

391

392

393 DAQ

Data Acquisition

394 DCS

Detector Control Software

395 DQM

Data Quality Monitoring

396 DT

Drift Tube

397

398

### F

399

400

401	<b>FEE</b>	Front-End Electronics
402	<b>FEB</b>	Front-End Board
403		
404		
405	<b>G</b>	
406		
407	<b>GE-/-</b>	Find a good description
408	<b>GE1/1</b>	Find a good description
409	<b>GE2/1</b>	Find a good description
410	<b>GEANT</b>	GEometry ANd Tracking - a series of software toolkit platforms developed by CERN
411		
412	<b>GEM</b>	Gas Electron Multiplier
413	<b>GIF</b>	Gamma Irradiation Facility
414	<b>GIF++</b>	new Gamma Irradiation Facility
415		
416		
417	<b>H</b>	
418		
419	<b>HL-LHC</b>	High Luminosity LHC
420	<b>HPL</b>	High-pressure laminate
421	<b>HV</b>	High Voltage
422		
423		
424	<b>I</b>	
425		
426	<b>iRPC</b>	improved RPC
427	<b>IRQ</b>	Interrupt Request
428	<b>ISR</b>	Intersecting Storage Rings
429		
430		
431	<b>L</b>	
432		
433	<b>LEIR</b>	Low Energy Ion Ring
434	<b>LEP</b>	Large Electron-Positron
435	<b>LHC</b>	Large Hadron Collider
436	<b>LS1</b>	First Long Shutdown
437	<b>LS3</b>	Third Long Shutdown
438	<b>LV</b>	Low Voltage
439	<b>LVDS</b>	Low-Voltage Differential Signaling
440		
441		
442	<b>M</b>	
443		
444	<b>MC</b>	Monte Carlo

445	MCNP	Monte Carlo N-Particle
446	ME-/	Find good description
447	ME0	Find good description
448	MRPC	Multigap RPC
449		
450		
451	<b>N</b>	
452		
453	NIM	Nuclear Instrumentation Module logic signals
454		
455		
456	<b>P</b>	
457		
458	PS	Proton Synchrotron
459	PMT	PhotoMultiplier Tube
460		
461		
462	<b>Q</b>	
463		
464	QCD	Quantum Chromodynamics
465	QED	Quantum Electrodynamics
466		
467		
468	<b>R</b>	
469		
470	RE-/	Find a good description
471	RE2/2	Find a good description
472	RE3/1	Find a good description
473	RE3/2	Find a good description
474	RE4/1	Find a good description
475	RE4/2	Find a good description
476	RE4/3	Find a good description
477	RMS	Root Mean Square
478	ROOT	a framework for data processing born at CERN
479	RPC	Resistive Plate Chamber
480		
481		
482	<b>S</b>	
483		
484	SC	Synchrocyclotron
485	SLAC	Stanford Linear Accelerator Center
486	SM	Standard Model
487	SPS	Super Proton Synchrotron

488		
489		
490	<b>T</b>	
491		
492	TDC	Time-to-Digital Converter
493	ToF	Time-of-flight
494		
495		
496	<b>W</b>	
497		
498	webDCS	Web Detector Control System

# 1

## Introduction

499

500

<sup>501</sup> **1.1 A story of High Energy Physics**

<sup>502</sup> **1.2 Organisation of this study**



# 2

503

504

## Investigating the TeV scale

505 „We may regard the present state of the universe as the effect of the  
506 past and the cause of the future. An intellect which at any given mo-  
507 ment knew all of the forces that animate nature and the mutual posi-  
508 tions of the beings that compose it, if this intellect were vast enough  
509 to submit the data to analysis, could condense into a single formula  
510 the movement of the greatest bodies of the universe and that of the  
511 lightest atom; for such an intellect nothing could be uncertain and  
512 the future just like the past would be present before its eyes.”

513

514 - Pierre Simon de Laplace, *A Philosophical Essay on Probabilities*, 1814

515 Throughout history, physics experiment became more and more powerful in order to investigate  
516 finer details of nature and helped understanding the elementary blocks of matter and the fundamental  
517 interactions that bond them in the microscopic world. Nowadays, the Standard Model (SM) of  
518 particle physics is the most accurate theory designed to explain the behaviour of particles and was  
519 able to make very precise predictions that are constantly verified, although some hints of new physics  
520 are visible as bricks are still missing to have a global comprehension of the Universe.

521 To highlight the limits of the SM and test the different alternative theories, ever more powerful  
522 machines are needed. This is in this context that the Large Hadron Collider (LHC) has been thought  
523 and built to accelerate and collide particles at energies exceeding anything that had been done before.  
524 Higher collision energies and high pile-up imply the use of enormous detectors to measure the  
525 properties of the interaction products. The Compact Muon Solenoid (CMS) is a multipurpose ex-  
526 periment that have been designed to study the proton-proton collisions of the LHC and give answers  
527 on various high energy physics scenari. Nevertheless, the luminosity delivered by the collider will  
528 in the future be increased to levels beyond the original plans to improve its discovery potential giv-  
529 ing no choice to experiments such as CMS to upgrade their technologies to cope with the increased  
530 radiation levels and detection rates.

## 531 **2.1 The Standard Model of Particle Physics**

532 In this early 21<sup>st</sup> century it is now widely accepted that matter is made of elementary blocks referred  
533 to as *elementary particles*. The physics theory that classifies and describes the best the behaviour  
534 and interaction of such elementary particles is the so called Standard Model that formalizes 3 of  
535 the 4 fundamental interactions (electromagnetic, weak and strong interactions). It's development  
536 took place during the 20<sup>th</sup> century thanks to a strong collaboration in between the theoretical and  
537 experimental physicists.

### 538 **2.1.1 A history of particle physics**

539 The idea that nature is composed of elementary bricks, called *atomism*, is not contemporary as it  
540 was already discussed by Indian or Greek philosophers during antiquity. In Greece, atomism has  
541 been rejected by Aristotelianism as the existance of *atoms* would imply the existance of a void that  
542 would violate the physical principles of Aristotle philosophy. Aristotelianism has been considered  
543 as a reference in the european area until the 15<sup>th</sup> century and the italian *Rinascimento* where antic  
544 text and history started to be more deeply studied. The re-discovery of Platon's philosophy would  
545 allow to open the door to alternative theories and give a new approach to natural sciences where  
546 experimentation would become central. A new era of knowledge was starting. By the begining of  
547 the 17<sup>th</sup> century, atomism was re-discovered by philosophers and the very first attempt to estimate  
548 an *atom* size would be provided by Magnetus in 1646. Although his *atoms* correspond to what would  
549 nowadays be called *molecules*, Magnetus achieved feats by calculating that the number of molecules  
550 in a grain of incense would be of the order of  $10^{18}$  simply by considering the time necessary to smell  
551 it everywhere in a large church after the stick was lit on. It is now known that this number only falls  
552 short by 1 order of magnitude.

553 An alternative philosophy to atomism popularized by Descartes was corpuscularianism. Built on  
554 ever divisible corpuscles, contrary to atoms, it's principles would be mainly used by alchemists like  
555 Newton who would later develop a corpuscular theory of light. Boyle would combine together ideas  
556 of both atomism or corpuscularianism leading to mechanical philosophy. The 18<sup>th</sup> century have

seen the development of engineering providing philosophical thought experiments with repeatable demonstration and a new point of view to explain the composition of matter and Lavoisier would greatly contribute to chemistry and atomism by publishing in 1789 a list of 33 chemical elements corresponding to what is now called *atoms*. In the early 19<sup>th</sup> century Dalton would summarize the knowledge on composition of matter and Fraunhofer would invent the spectrometer and discover the spectral lines. The rise of atomic physics, chemistry and mathematical formalism would unravel the different atomic elements and ultimately, the 20<sup>th</sup> century would see the very first sub-atomic particles.

**Discovery of the inner structure of the atom**

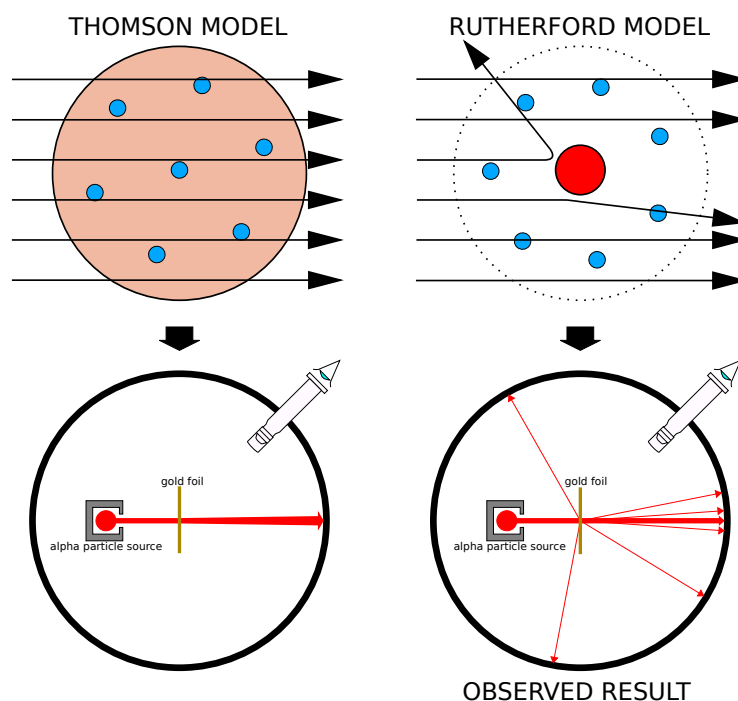


Figure 2.1: Through the gold foil experiment Rutherford could show that most of the mass of atoms was contained in a positively charged nucleus and could then propose a more accurate atomic model than that of Thomson.

The negative *electron* would be the first to be discovered in 1897 by Thomson after 3 decades of research on cathode rays by proving that the electrification observed in an electroscope, as reported by Perrin, was due to the rays themselves and that they had to be composed of electrically charged particles. In 1900, Becquerel would show the *beta rays* emitted by radium had the same charge over mass ratio than what measured by Thomson for cathode rays, pointing to electrons as a constituent of atoms. In 1907, Rutherford and Royds showed that *alpha* particles, once captured in a tube and subjected to an electric spark causing an electron avalanche, where helium ions as they could combine with 2 electrons to form a  ${}^4\text{He}$ . This discovery was directly followed by the constraint of the atom structure in 1909 through the gold foil experiment in which the deflection angle of alpha particles fired at a very thin gold foil was measured and highlighted atoms where mainly empty with

576 nearly all its mass contained into a tiny positively charged *nucleus*. With these two observations,  
 577 he could formulate the Rutherford model of the atom in 1911, shown together with the Thomson  
 578 plum pudding model in Figure 2.1. The link in between atomic number and number of positive and  
 579 negative charges contained into the atoms would fast be understood and the different kind of element  
 580 transmutation appeared to be purely nuclear processes making clear that the electromagnetic nature  
 581 of chemical transformation could not possibly change nuclei. Thus a new branch in physics appeared  
 582 to study nuclei exclusively: the nuclear physics.

583 Moreover, in 1913 quantum physics would be introduced into the atomic model by Bohr based  
 584 on the assumptions of Plank to explain spectral lines, and other observed quantum effects. The same  
 585 year, Moseley would confirm Borh's model and Debye would extend it by introducing elliptical  
 586 orbits.

587 By studying alpha emission and the product of their interaction with nitrogen gas, Rutherford  
 588 reported in 1919 the very first nuclear reaction leading to the discovery that the hydrogen nucleus was  
 589 composed of a single positively charged particle that was later baptised *proton*. This idea came from  
 590 1815 Prout's hypothesis proposing that all atoms are composed of "*protyles*" (i.e. hydrogen atoms).  
 591 By using scintillation detectors, Rutherford could highlight typical hydrogen nuclei signature and  
 592 understand that the impact of alpha particles with nitrogen would knock out an hydrogen nucleus  
 593 and produce an oxygen 17, as explicated in Formula 2.1 and would then postulate that protons are  
 594 building bricks of all elements.



595 With this assumption and the discovery of isotopes together with Aston, elements with identical  
 596 atomic number but different masses, Rutherford would propose that all elements' nuclei but hydrogen's are composed of both charged particles, protons, and of chargeless particles, which he called  
 597 *neutrons*, and that these neutral particles would help maintaining nuclei as one, as charged protons  
 598 were likely to electrostatically repulse each other, and introduced the idea of a new force, a *nuclear*  
 599 force. Though the first idea concerning neutrons was a bond state of protons and electrons as it was  
 600 known that the beta decay, emitting electrons, was taking place in the nucleus, it was then showed  
 601 that such a model would hardly be possible due to Heisenberg's uncertainty principle and by the  
 602 recently measured *spin* of both protons and electrons. The spin, discovered through the study of  
 603 the emission spectrum of alkali metals, would be understood as a "two-valued quantum degree of  
 604 freedom" and formalized by Pauli and extended by Dirac, to take the relativist case into account.  
 605 Measured to be  $\frac{1}{2}\hbar$  for both, it was impossible to arrange an odd number of half integer spins and  
 606 obtain a global nucleus spin that would be integer. Finally, in 1932, following the discovery of a new  
 607 neutral radiation, Chadwick could discover the neutron as an uncharged particle with a mass similar  
 608 to that of the proton whose half integer spin would reveal to be the solution to explain the nuclear  
 609 spin.  
 610

### 611 Development of the Quantum Electrodynamics

612 Historically, the development of the quantum theory revolved around the question of emission and  
 613 absorption of discrete amount of energy through light. Einstein used the initial intuition of Plank  
 614 about the black-body radiation to develop in 1905 a model to explain the photoelectric effect in  
 615 which light was described by discrete quanta now called *photons*. For this model, Einstein introduced  
 616 the concept of wave-particle duality as classical theory was not able to describe the phenomenon.  
 617 With the new understanding of atoms and of their structure, classical theories also proved unable

618 to explain atoms stability. Indeed, using classical mechanics, electrons orbiting around a nucleus  
 619 should radiate an energy proportional to their angular momentum and thus lose energy through  
 620 time and the spectrum of energy emission should then be continuous, but it was known since the  
 621 19<sup>th</sup> century and the discovery of spectral lines that the emission spectrum of material was discrete.

622 This was Bohr who first suggested that a quantum description of the atom was necessary in 1913.  
 623 Using the correspondence principle stating that at large enough numbers the quantum calculations  
 624 should give the same results than the classical theory, he proposed the very first quantum model  
 625 of the hydrogen atom explaining the line spectrum by introducing the principal quantum number  
 626  $n$  describing the electron shell. This model would then be improved by Sommerfeld that would  
 627 quantize the z-component of the angular momentum, leading to the second and third quantum  
 628 numbers, or azimuthal and magnetic quantum number,  $l$  and  $m$  defining for the second the orbital  
 629 angular momentum of the electrons on their shells and thus, the shape of the orbital, and for the third  
 630 the available orbital on the subshell for each electron. Nevertheless, although the model was not only  
 631 limited to spherical orbitals anymore, making the atom more realistic, the Zeeman effect couldn't be  
 632 completely explained by just using  $n$ ,  $l$  and  $m$ . A solution would be brought after the discovery of  
 633 Pauli in 1924, as Uhlenbeck, Goudsmit, and Kramers proposed in 1925 the idea of intrinsic rotation  
 634 of the electron, introducing a new angular momentum vector associated to the particle itself, and  
 635 not to the orbital, and associated to a new quantic number  $s$ , the *spin* projection quantum number  
 636 explaining the lift of degeneracy to an even number of energy levels.

637 The introduction of the *spin* happened 1 year after another attempt of improvement of the theory  
 638 was made by De Broglie in his PhD thesis. The original formulation of the quantum theory only  
 639 considered photons as energy quanta behaving as both waves and particles. De Broglie proposed  
 640 that all matter are described by waves and that their momentum is proportional to the oscillation of  
 641 quantized electromagnetic field oscillators. This interpretation was able to reproduce the previous  
 642 version of the quantum energy levels by showing that the quantum condition involves an integer  
 643 multiple of  $2\pi$ , as shown by Formula 2.2.

$$p = \hbar k \Leftrightarrow \int pdx = \hbar \int kdx = 2\pi\hbar n \quad (2.2)$$

644 Although the intuition of De Broglie about the wave-particle duality of all matter, his interpretation  
 645 was semiclassical and it's in 1926 that the first fully quantum mechanical wave-equation would  
 646 be introduced by Schrödinger to describe electron-like particles, reproducing the previous semiclassical  
 647 formulation without inconsistencies. This complexe equation describes the evolution of the  
 648 wave function  $\Psi$  of the quantum system, defined by its position vector  $\mathbf{r}$  and time  $t$  as an energy  
 649 conservation law, in which the hamiltonian of the system  $\hat{H}$  is explicit, by solving the Equation 2.3.

$$i\hbar \frac{\partial}{\partial t} |\Psi(\mathbf{r}, t)\rangle = \hat{H} |\Psi(\mathbf{r}, t)\rangle \quad (2.3)$$

650 In 1927, Dirac would go further in his paper about emission and absorption of radiation by  
 651 proposing a second quantization not only of the physical process at play but also of the electromagnetic  
 652 field, providing the ingredients to the first formulation of *Quantum Electrodynamics (QED)*  
 653 and the description of photon emission by electrons dropping into a lower energy state in which the  
 654 final number of particles is different than the initial one. To complete this model to the many-body  
 655 wave functions of identical particles, Jordan included creation and annihilation operators for fields  
 656 obeying Fermi-Dirac statistics leading to a model describing particles that would be referred to as  
 657 *fermions*. Nevertheless, in order to properly treat electromagnetism, the incorporation of the relativ-

ity theory developed by Einstein. Including gravity into quantum physics still is a challenge nowadays, but in 1928 Pauli and Jordan would show that special relativity's coordinate transformations could be applied to quantum fields as the field commutators were Lorentz invariant. Finally derived the same year, the Dirac equation, shown as Equation 2.4, similarly to Schrödinger's equation, is a single-particle equation but it incorporates special relativity in addition to quantum mechanics rules. It features the  $4 \times 4$  gamma matrices  $\gamma^\mu$  built using  $2 \times 2$  Pauli matrices and unitary matrix, the 4-gradient  $\partial_\mu$ , the rest mass  $m$  of any half integer spin massive particle described by the wave function  $\psi(x, t)$ , also called a Dirac spinor, and the speed of light  $c$ . In addition to perfectly reproduce the results obtained with quantum mechanics so far, it also provided with *negative-energy solutions* that would later be interpreted as a new form of matter, *antimatter* and give a theoretical justification to the Pauli equation that was phenomenologically constructed to account for the spin as in the non-relativistic limit, the Dirac equation is similar.

$$i\hbar\gamma^\mu\partial_\mu\psi - mc\psi = 0 \quad (2.4)$$

The successes of the QED was soon followed with theoretical problems as computations of any physical process involving photons and charged particles were showed to be only reliable at the first order of perturbation theory. At higher order of the theory, divergent contributions were appearing giving nonsensical results. Only two effects were contributing to these infinities.

- The self-energy of the electron (or positron), the energy that the particle has due its own interaction with its environment.
- The vacuum polarization, virtual electron–positron pairs produced by a background electromagnetic field in the vacuum which is not an "empty" space. These virtual pairs affect the charge and current distributions generated by the original electromagnetic field.

Solving this apparent problem was done by carefully defining the concepts of each observables, for example mass or charge, as these quantities are understood within the context of a non-interacting field equation, and that from the experiment point of view, they are abstractions as what is measured are "renormalized observables" shifted from there "bare" value by the interaction taking place in the measuring process. The infinities needed to be connected to corrections of mass and charge as those are fixed to finite values by experiment. This was the intuition of Bethe in 1947 who successfully computed the effect of such *renormalization* in the non-relativist case. Fully covariant formulations of QED including renormalization was achieved by 1949 by Tomonaga, Schwinger, Feynman and Dyson and Feynman is now famous for his association of diagrams to the term of the scattering matrix, greatly simplifying the representation and computation of interactions as the diagrams directly corresponded the measurable physical processes and would then be used in every quantum field theories. With the resolution of infinities, QED had mostly reached its final form, being still today the most accurate physical theory and would serve as a model to build all other quantum field theories.

### 693 The Weak interaction and the Electroweak unification

694 The weak interaction is the process that causes radioactive decays. Thanks to the neutron discovery,  
 695 Fermi could explain in 1934 the beta radiations through the beta decay process in which the neutron  
 696 decays into a proton by emitting an electron. Though the missing energy observed during this  
 697 process triggered a huge debate about the apparent non conservation of energy, momentum and spin

698 of the process, Fermi, as Pauli before him, proposed that the missing energy was due to a neutral  
 699 not yet discovered particle that would then be baptised *neutrino*. The impossibility to detect such  
 700 a particle would leave some members of the scientific community sceptical, but hints of energy  
 701 conservation and of the existence of the neutrino were provided by measuring the energy spectrum  
 702 of electrons emitted through beta decay, as there was a strict limit on their energy. It's only 30 years  
 703 later in 1953 that it would be discovered by the team of Cowan and Reines using the principle of  
 704 inverse beta decay described through Formula 2.5. The experiment consisted in placing water tanks  
 705 sandwiched in between liquid scintillators near a nuclear reactor with an estimated neutrino flux of  
 706  $5 \times 10^{13} \text{ s}^{-1} \text{ cm}^{-2}$ . However, in order to explain the absence of some reactions in the experiment  
 707 of Cowan and Reines, and constraint the beta decay theory of Fermi and extend it to the case of  
 708 the muon, Konopinski and Mahmoud proposed in 1953 that the muon decay would eject a particle  
 709 similar to the neutrino and thus predicted the existence of a muon neutrino that would be different  
 710 than the one involved in the beta decay, related to the electron. With this, the idea of lepton number  
 711 would arise. The muon neutrino would successfully be detected in 1962 by Lederman, Schwartz and  
 712 Steinberger.

$$\bar{\nu} + p \rightarrow n + e^+ \quad (2.5)$$

713 The theory could not be valid though as the probability of interaction, called cross-section, would  
 714 have been increasing without bond with the square of the energy. Fermi assumed in a two vector  
 715 current coupling but Lee and Yang noted that an axial current could appear and would violate parity.  
 716 The experiment of Wu in 1956 would confirm the parity violation and Gamow and Teller would try to  
 717 account for it by describing Fermi's interaction through allowed (parity-violating) and superallowed  
 718 (parity-conserving) decays.

## 719 Development of the Higgs mechanism

## 720 Development of the quark model and Quantum Chromodynamics

721 To explain the nuclear force that holds *nucleons* (protons and neutrons) together, Yukawa theoretically  
 722 proposed in 1934 the existence of a force carrier called *meson* due to its predicted mass in  
 723 the range in between the electron and nucleon masses. Discovered in 1936 by Anderson and Neddermeyer,  
 724 and confirmed using bubble chambers in 1937 by Street and Stevenson, a first meson candidate was observed in the decay products of cosmic rays. Assuming it had the same electric  
 725 charge than electrons and protons, this particle was observed to have a curvature due to magnetic  
 726 field that was sharper than protons but smoother than electrons resulting in a mass in between that  
 727 of electrons and protons. But its properties were not compatible with Yukawa's theory, which was  
 728 emphasized by the discovery of a new candidate in 1947, again in cosmic ray products using photographic  
 729 emulsions.

730 This new candidate, although it had a similar mass than the already believed *meson*, would rather  
 731 decay into it. For distinction, the first candidate would then be renamed "*mu meson*" when the second  
 732 would be the "*pi meson*". The *mu meson* was behaving like a heavy electron and didn't participate  
 733 in the strong interaction whereas the pion was believed to be the carrier of the nuclear interaction.  
 734 This lead to classify the *mu* in a new category of particles called *leptons* together with the electron  
 735 that shared similar properties and the neutrino, and be renamed *muon*. The *pi meson* was finally  
 736 found to be a triplet of particles: a positively charged, a negatively charged, and a neutral particle.  
 737 The neutral *pi meson* has been more difficult to identify as it wouldn't leave tracks on emulsions nor

<sup>739</sup> on bubble chambers and needed to be studied via its decay products. It was ultimately identified in  
<sup>740</sup> University of California's cyclotron in 1950 through the observation of its decay into 2 photons.

<sup>741</sup> Also discovered in 1947 but in cloud chamber photographs, the *K meson* has also been an im-  
<sup>742</sup> portant step towards the establishment of the Standard Model. A triplet of particle, 2 charged and a  
<sup>743</sup> neutral, with a mass roughly half that of a proton, were reported. These particles were baptised *K*  
<sup>744</sup> *meson* in contrast to the "light" *pi* and *mu* "L-mesons". The particularity of the *K* were there very  
<sup>745</sup> slow decays with a typical lifetime of the order of  $10^{-10}$ s much greater than the  $10^{-23}$ s of *pi*-proton  
<sup>746</sup> reactions. The concept of *strangeness*, a new quantum number was then introduced by Pais as an  
<sup>747</sup> attempt to explain this phenomenon as *strange* particles appeared as a pair production of a strange  
<sup>748</sup> and anti-strange particle.

<sup>749</sup> With the development of synchrotrons, the particle *zoo* would grow to several dozens during the  
<sup>750</sup> 1950s as higher energies were reachable through acceleration. In 1961, a first classification system,  
<sup>751</sup> called Eightfold Way, was proposed by Gell-Mann and finding its roots in the Gell-Mann–Nishijima  
<sup>752</sup> formula, which relates the electric charge *Q*, the third component of the isospin *I*<sub>3</sub>, the *baryon*  
<sup>753</sup> number *B* and the strangeness *S*, as explicated in Formula 2.6. The isospin was a quantum number  
<sup>754</sup> introduced in 1932 to explain symmetries of the newly discovered neutron using representation  
<sup>755</sup> theory of SU(2). The baryon number, was introduced by Nishijima as a quantum number for baryons,  
<sup>756</sup> i.e. particles of the same family as nucleons. The mesons were classified in an octet and baryons of  
<sup>757</sup> spin  $\pm \frac{1}{2}$  and  $\pm \frac{3}{2}$  were respectively classified into an octet and a decuplet, as shown in Figure 2.2. To  
<sup>758</sup> complete the baryon decuplet, Gell-Mann predicted the existence of baryon  $\Omega^-$  which would later  
<sup>759</sup> be discovered in 1964.

$$Q = I_3 + \frac{1}{2}(B + S) \quad (2.6)$$

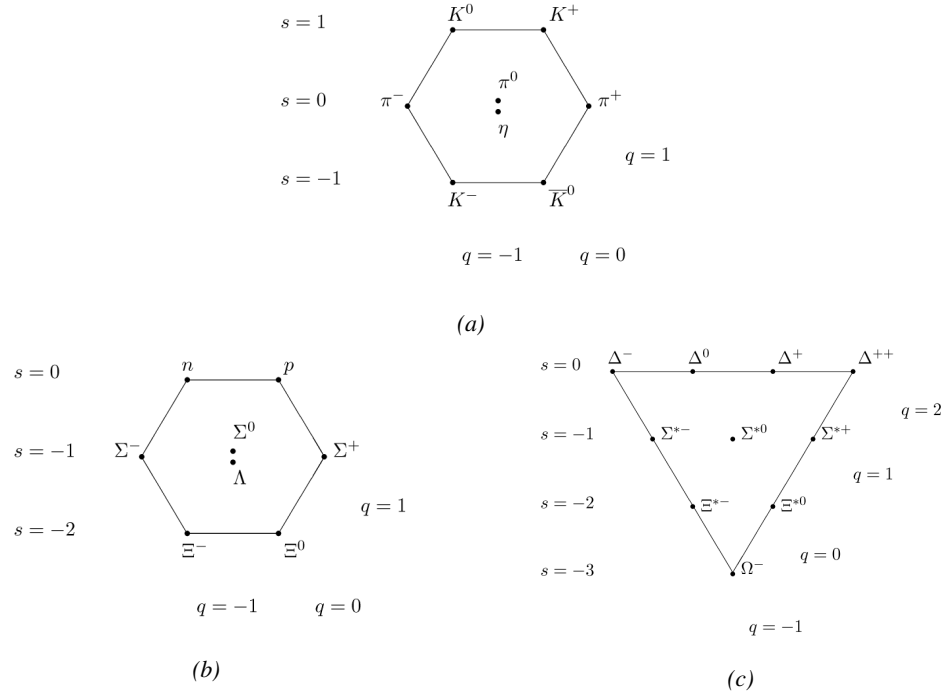


Figure 2.2: Figure 2.2a: Meson octet. Figure 2.2b: Baryon octet. Figure 2.2c: Baryon decuplet.

Strong of this classification using an SU(3) flavor symmetry, Gell-Mann, and independently Zweig, would propose a full theoretical model in which *hadrons* (strongly interacting particles, i.e. mesons and baryons) were not elementary particles anymore. They would rather be composed with 3 flavors of particles called *quarks* and there anti-particles. The 3 flavors were called *up*, *down* and *strange*. *Up* and *down* would be used to explain the nucleons and non-strange mesons, while *strange* would come into the composition of hadrons showing strangeness. *Up* and *down* flavors would be discovered in 1968 thanks to the deep inelastic scattering experiments conducted at the Stanford Linear Accelerator Center (SLAC), and *strange* could only be indirectly validated even though it provided a robust explanation to *kaon* ( $K$ ) and *pion* ( $\pi$ ). However, in the decade following the Gell-Mann-Zweig quark model proposition, several improvement to the model were brought, first by Glashow and Bjorken the same year that predicted the existence of a fourth quark flavor, the *charm*, that would equalize the then known number of quarks and leptons and finally in 1973 by Kobayashi and Maskawa that would increase the number of quarks to 6 to explain the experimental observation of CP violation. These two quarks would be referred to as *top* and *bottom* for the first time in 1975. It's only after these additions to the quark model that finally the *charm* would be discovered in 1974 at both SLAC and Brookhaven National Laboratory (BNL). A meson where the *charm* was bound with an *anti-charm*, called  $J/\psi$ , would help convince the physics community of the validity of the model. The *top* would be discovered soon after in 1977 in Fermilab and indicate the existence of the *bottom* that would resist to discovery until Fermilab's experiments CDF and D $\emptyset$  in 1995 due to its very large mass and the energy needed to produce it.

As remarked by Struminsky, the original quark model proposal composed of 3 quarks should possess an additional quantum number due to mesons such as  $\Omega^-$  or  $\Delta^{++}$ . Indeed, these mesons are composed of 3 identical quarks, respectively 3 *strange* and *up* quark, with parallel spins, which

should be forbidden by the exclusion principle. Independentle, Greenberg and Han-Nambu proposed an additional SU(3) degree of freedom possessed by the quarks, that would later be refered to as *color charge gauge*, that could interact through *gluons*, the gauge boson octet corresponding to this degree of freedom. Nevertheless, as observing free quarks proved to be impossible, two visions of the quarks were argued mainly due to the failures to observe these particles free to prove their existence. On one side, Gell-Mann proposed to see quarks as mathematical construct instead of real particles, as they are always confined, implying that quantum field theory would not describe entirely the strong interaction. Opposed to this vision, Feynman on the contrary argued that quarks were real particles, that he would call *partons*, that should be described as all other particles by a distribution of position and momentum. The implications of quarks as point-like particles would be verified at SLAC and the concept of *color* would be added to the quark model in 1973 by Fritzsch and Leutwyler together with Gell-Mann to propose a description of the strong interaction through the theory of Quantum Chromodynamics (QCD). The discovery the same year of asymptotic freedom within the QCD by Groos, Politzer and Wilczek, allowed for very precise predictions thanks to the perturbation theory. Nowadays, the confinement of quarks is studied in experiments such as ALICE, through exploration of the quark-gluon plasma.

### 2.1.2 Construction and test of the model [TO SEE IF KEPT - MAYBE TOO COMPLEX]

$$\mathcal{L}_{QCD} = \bar{\psi}_i (i(\gamma^\mu D_\mu)_{ij} - m\delta_{ij}) \psi_j - \frac{1}{4} G_{\mu\nu}^a G_a^{\mu\nu} \quad (2.7)$$

The QCD Lagragian is given in Formula 2.7, where  $\psi_i(x)$  is the quark field in the fundamental representation of the SU(3) gauge group,  $D_\mu$  is the gauge covariant derivative, the  $\gamma^\mu$  are Dirac matrices.  $G_{\mu\nu}^a$  represents the gauge invariant gluon field strength tensor, analogous to the electromagnetic field strength tensor,  $F^{\mu\nu}$ , in QED and is described by Formula 2.8.

$$G_{\mu\nu}^a = \partial_\mu A_\nu^a - \partial_\nu A_\mu^a + g f^{abc} A_\mu^b A_\nu^c \quad (2.8)$$

$A_\mu^a(x)$  are the gluon fields, in the adjoint representation of the SU(3) gauge group, and  $f_{abc}$  are the structure constants of SU(3). Finally, the variables  $m$  and  $g$  correspond to the quark mass and coupling of the theory, respectively, which are subject to renormalization.

### 2.1.3 Investigating the TeV scale

## 2.2 The Large Hadron Collider & the Compact Muon Solenoid

Throughout its history, CERN has played a leading role in high energy particle physics. Large regional facilities such as CERN were thought after the second world war in an attempt to increase international scientific collaboration and allows scientists to share the forever increasing costs of experiment facilties required due to the need for increasing the energy in the center of mass to deeper probe matter. The construction of the first accelerators at the end of the 50s, the Synchro-cyclotron (SC) and the Proton Synchrotron (PS), was directly followed by the first observation of antinuclei in 1965 [1]. Strong from the experience of the Intersecting Storage Rings (ISR), the very first proton-proton collider that showed hints that protons are not elementary particles, the Super Proton Synchrotron (SPS) was built in the 70s to investigate the structure of protons, the preference for matter over antimatter, the state of matter in the early universe or exotic particles, and lead to

820 the discovery in 1983 of the W and Z bosons [2–5]. These newly discovered particles and the elec-  
821 troweak interaction would then be studied in details by the Large Electron-Positron (LEP) collider  
822 that will help to prove in 1989 that there only are three generations of elementary particles [6]. The  
823 LEP would then be dismantled in 2000 to allow for the LHC to be constructed in the existing tunnel.

824 **2.2.1 LHC, the most powerful particle accelerator**

825 The LHC has always been considered as an option to the future of CERN. At the moment of the  
826 construction of the LEP beneath the border between France and Switzerland, the tunnel was built in  
827 order to accomodate what would be a Large Hadron Collider with a dipole field of 10 T and a beam  
828 energy in between 8 and 9 TeV [7] directly followed in 1985 with the creation of a 'Working Group  
829 on the Scientific and Technological Future of CERN' to investigate such a collider [8]. The decision  
830 was finally taken almost 10 years later, in 1994, to construct the LHC in the LEP tunnel [9] and the  
831 approval of the 4 main experiments that would take place at the 4 interaction points would come in  
832 1997 [10] and 1998 [11]:

833 • ALICE [12] has been designed in the purpose of studying quark-gluon plasma that is believed  
834 to have been a state of matter that existed in the very first moment of the universe.

835 • ATLAS [13] and CMS [14] are general purpose experiments that have been designed with  
836 the goal of continuing the exploration of the Standard Model and investigate new physics.

837 • LHCb [15] has been designed to investigate the preference of matter over antimatter in the  
838 universe through the CP violation.

839 These large scale experiments, as well as the full CERN accelerator complex, are displayed on  
840 Figure 2.3.

### CERN's Accelerator Complex

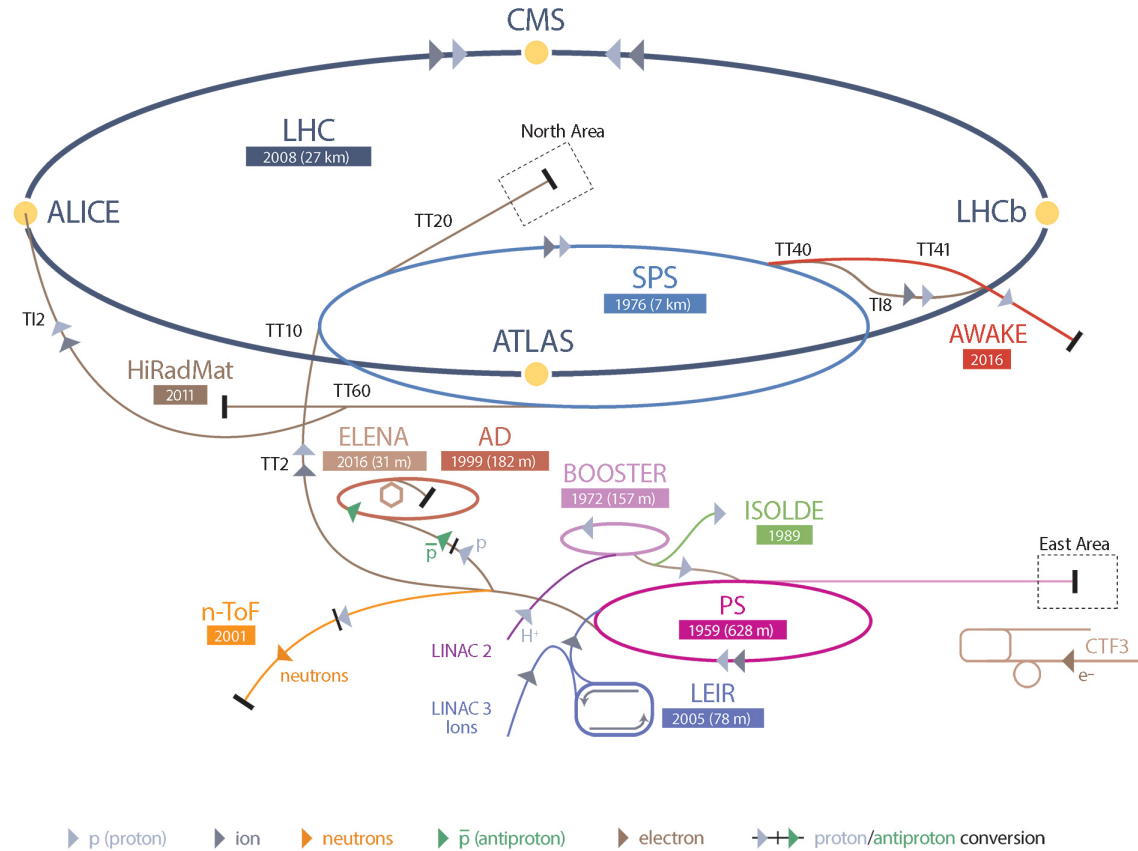


Figure 2.3: CERN accelerator complex.

The LHC is a 27 km long hadron collider and the most powerful accelerator used for particle physics since 2008 [16]. The LHC was originally designed to collide protons at a center-of-mass energy of 14 TeV and luminosity of  $10^{34} \text{ cm}^{-2}\text{s}^{-1}$ , as well as  $Pb$  ions at a center-of-mass energy of 2.8 TeV/A with a peak luminosity of  $10^{27} \text{ cm}^{-2}\text{s}^{-1}$ . Run 1 of LHC, when the center-of-mass energy only was half of the nominal LHC energy, was enough for both CMS and ATLAS to discover the Higgs boson [17] and for LHCb to discover pentaquarks [18] and confirm the existence of tetraquarks [19]. Nevertheless, after the Third Long Shutdown (LS3) (2024-2026), the accelerator will be in the so called High Luminosity LHC (HL-LHC) configuration [20], increasing its instantaneous luminosity to  $10^{35} \text{ cm}^{-2}\text{s}^{-1}$  for  $pp$  collisions and to  $4.5 \times 10^{27} \text{ cm}^{-2}\text{s}^{-1}$ , boosting the discovery potential of the LHC.

#### 2.2.1.1 Particle acceleration

The LHC is the last of a long series of accelerating devices. Before being accelerated by the LHC, the particles need to pass through different acceleration stages. All these acceleration stages are

854 visible on Figure 2.3 and pictures of the accelerators are showed in Figure 2.4.

855

856       The story of accelerated protons at CERN starts with a bottle of hydrogen gas injected into the  
857 source chamber of the linear particle accelerator *LINAC 2* in which a strong electric field strips the  
858 electron off the hygrogen molecules only to keep their nuclei, the protons. The cylindrical conductors,  
859 alternatively positively or negatively charged by radiofrequency cavities, accelerate protons by  
860 pushing them from behing and pulling them from the front and ultimately give them an energy of  
861 50 MeV, increasing their mass by 5% in the process.

862

863       When exiting the LINAC 2, the protons are divided into 4 bunches and injected into the 4 su-  
864 perimposed synchrotron rings of the *Booster* where they are then accelerated to reach an energy of  
865 1.4 GeV before being injected into the *PS*. Before the Booster was operational in 1972, the protons  
866 were directly injected into the PS from the LINAC 2 but the low injection energy limited the amount  
867 of protons that could be accelerated at once by the PS. With the Booster, the PS accepts approxi-  
868 mately 100 times more particles.

869

870       The 4 proton bunches are thus sent as one to the PS where their energy eventually reaches  
871 26 GeV. Since the 70s, the main goal of this 628 m circumference synchrotron has been to sup-  
872 ply other machines with accelerated particles. Nowadays, not only the PS accelerates protons, it also  
873 accelerates heavy ions from the *Low Energy Ion Ring (LEIR)*. Indeed, the LHC experiments are not  
874 only designed to study *pp*-collisions but also *Pb*-collisions. Lead is first injected into the dedicated  
875 linear collider *LINAC 3*, that accelerate the ions using the same principle than LINAC 2. Electrons  
876 are striped off the lead ions all along the acceleration process and eventually, only bare nuclei are  
877 injected in the LEIR whose goal is to transform the long ion pulses received into short dense bunches  
878 for LHC. Ions injected and stored in the PS were aceelerated by the LEIR from 4.2 MeV to 72 MeV.

879

880       Directly following the PS, is finally the last acceleration stage before the LHC, the 7 km long  
881 *SPS*. The SPS accelerates the protons to 450 GeV and inject proton in both LHC accelerator rings  
882 that will increase their energy up to 7 TeV. When the LHC runs with heavy lead ions for ALICE  
883 and LHCb, ions are injected and accelerated to reach the energy of 2.8 TeV/A.

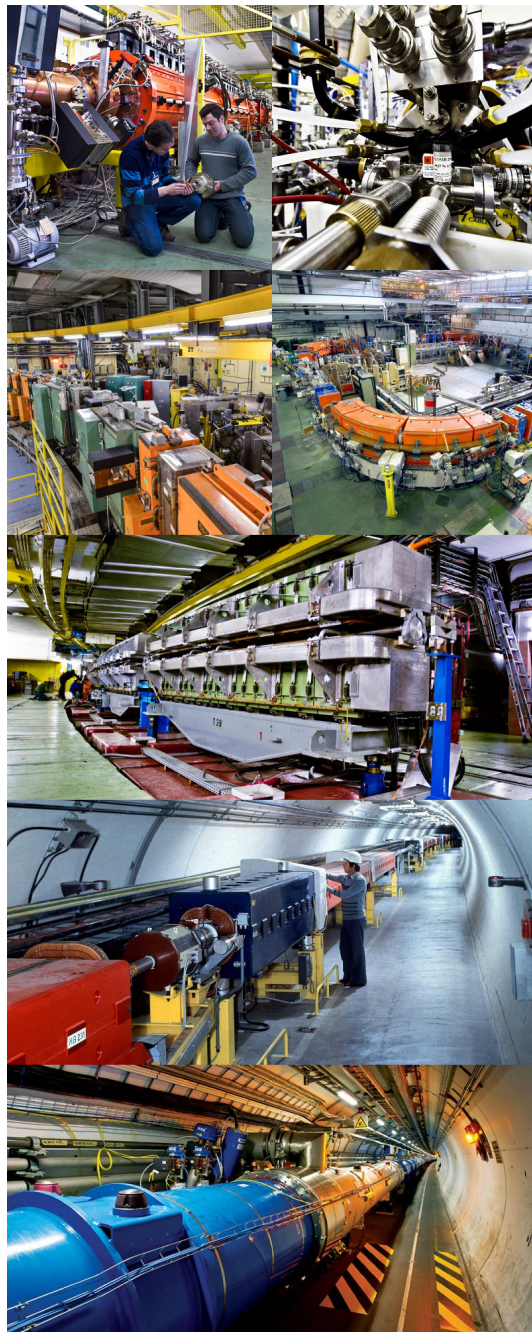


*Figure 2.4: Pictures of the different accelerators. From top to bottom: first the LINAC 2 and the Pb source of LINAC 3. Then the Booster and the LEIR. Finally, the PS, the SPS and the LHC.*

884      The LHC beams are not continuous and are rather organised in bunches of particles. When in  $pp$ -  
 885      collision mode, the beams are composed of 2808 bunches of  $1.15 \times 10^{11}$  protons separated by 25 ns.  
 886      When in  $Pb$  collision mode, the 592  $Pb$  bunches are on the contrary composed of  $2.2 \times 10^8$  ions  
 887      separated by 100 ns. The two parallel proton beams of the LHC are contained in a single twin-

bore magnet due to the space restriction in the LEP tunnel. Indeed, building 2 completely separate accelerator rings next to each other was impossible. The dipoles of the 1232 twin-bore magnets are showed in Figure 2.5 alongside the magnetic field generated along the dipole section to accelerate the particles. The dipoles generate a nominal field of 8.33 T, needed to give protons and lead nucleons their nominal energy. Some 392 quadrupoles, presented in Figure 2.6, are also used to focus the beams, as well as other multipoles to correct smaller imperfections.

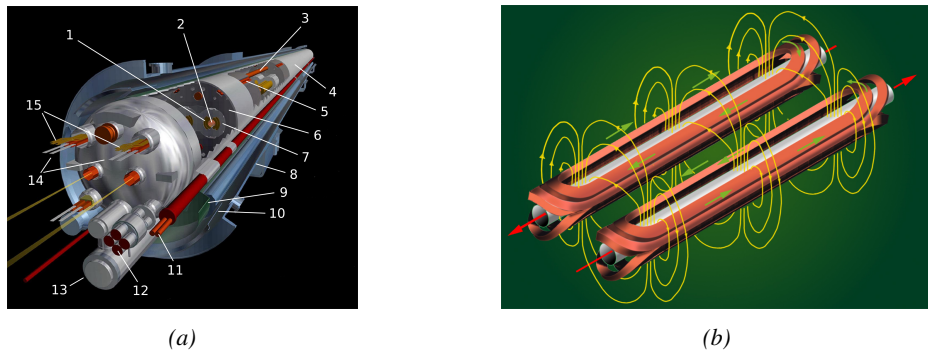


*Figure 2.5: Figure 2.5a: schematics of the LHC cryodipoles. 1: Superconducting Coils, 2: Beam pipe, 3: Heat exchanger Pipe, 4: Helium-II Vessel, 5: Superconducting Bus-bar, 6: Iron Yoke, 7: Non-Magnetic Collars, 8: Vacuum Vessel, 9: Radiation Screen, 10: Thermal Shield, 11: Auxiliary Bus-bar Tube, 12: Instrumentation Feed Throughs, 13: Protection Diode, 14: Quadrupole Bus-bars, 15: Spool Piece Bus-bars. Figure 2.5b: magnetic field and resulting motion force applied on the beam particles.*

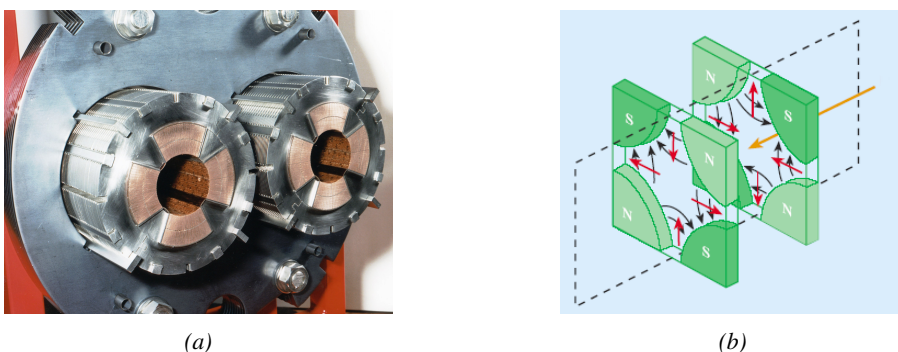


*Figure 2.6: Figure 2.6a: picture of the LHC quadrupoles. Figure 2.6b: magnetic fields and resulting focussing force applied on the beam by 2 consecutive quadrupoles.*

### 894 2.2.1.2 LHC discoveries and LHC physics program

895 The very first proton beam successfully circulated in the LHC in September 2008 directly followed  
 896 by an incident leading to mechanical damage that would delay the LHC program for a year until  
 897 November 2009.

898 **2.2.1.3 High Luminosity LHC**

899 **2.2.2 CMS, a multipurpose experiment**

900 **2.3 Muon Phase-II Upgrade**

901 After the more than two years lasting First Long Shutdown (LS1), the Large Hadron Collider (LHC)  
 902 delivered its very first Run-II proton-proton collisions early 2015. LS1 gave the opportunity to the  
 903 LHC and to the its experiments to undergo upgrades. The accelerator is now providing collisions  
 904 at center-of-mass energy of 13 TeV and bunch crossing rate of 40 MHz, with a peak luminosity  
 905 exceeding its design value. During the first and upcoming second LHC Long Shutdown, the Compact  
 906 Muon Solenoid (CMS) detector is also undergoing a number of upgrades to maintain a high system  
 907 performance [21].

908 From the LHC Phase-2 or High Luminosity LHC (HL-LHC) period onwards, i.e. past the Third  
 909 Long Shutdown (LS3), the performance degradation due to integrated radiation as well as the average  
 910 number of inelastic collisions per bunch crossing, or pileup, will rise substantially and become a  
 911 major challenge for the LHC experiments, like CMS that are forced to address an upgrade program  
 912 for Phase-II [22]. Simulations of the expected distribution of absorbed dose in the CMS detector  
 913 under HL-LHC conditions, show in figure 4.16 that detectors placed close to the beamline will have  
 914 to withstand high irradiation, the radiation dose being of the order of a few tens of Gy.

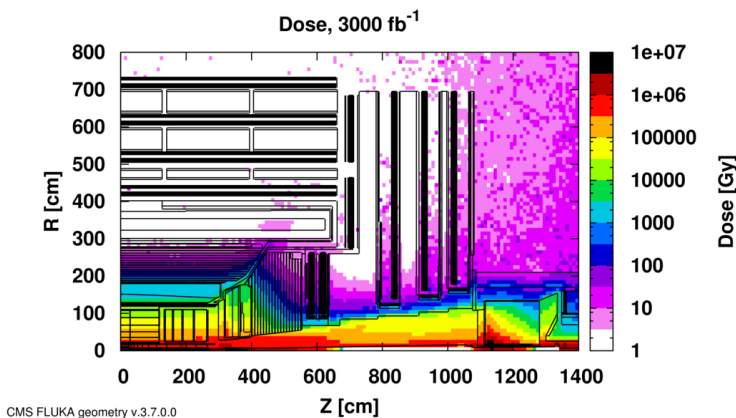


*Figure 2.7: Absorbed dose in the CMS cavern after an integrated luminosity of 3000 fb. R is the transverse distance from the beamline and Z is the distance along the beamline from the Interaction Point at Z=0.*

915 The measurement of small production cross-section and/or decay branching ratio processes, such  
 916 as the Higgs boson coupling to charge leptons or the  $B_s \rightarrow \mu^+ \mu^-$  decay, is of major interest and  
 917 specific upgrades in the forward regions of the detector will be required to maximize the physics  
 918 acceptance on the largest possible solid angle. To ensure proper trigger performance within the  
 919 present coverage, the muon system will be completed with new chambers. In figure 2.8 one can  
 920 see that the existing Cathode Strip Chambers (CSCs) will be completed by Gas Electron Multipliers  
 921 (GEMs) and Resistive Plate Chambers (RPCs) in the pseudo-rapidity region  $1.6 < |\eta| < 2.4$  to  
 922 complete its redundancy as originally scheduled in the CMS Technical Proposal [23].

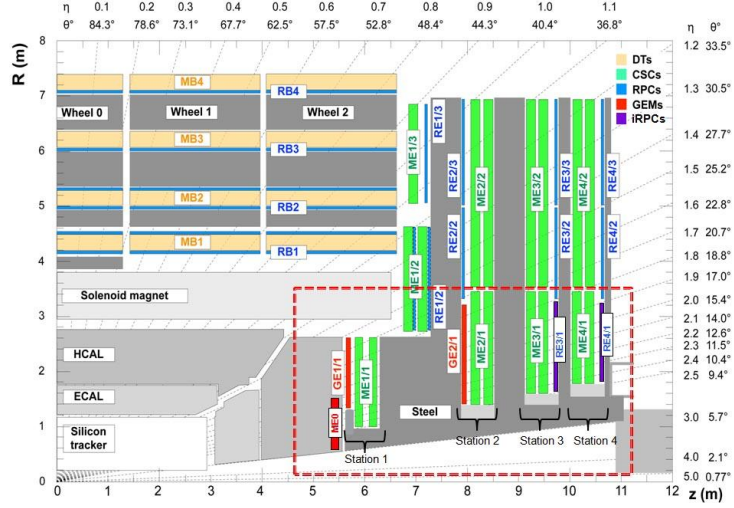
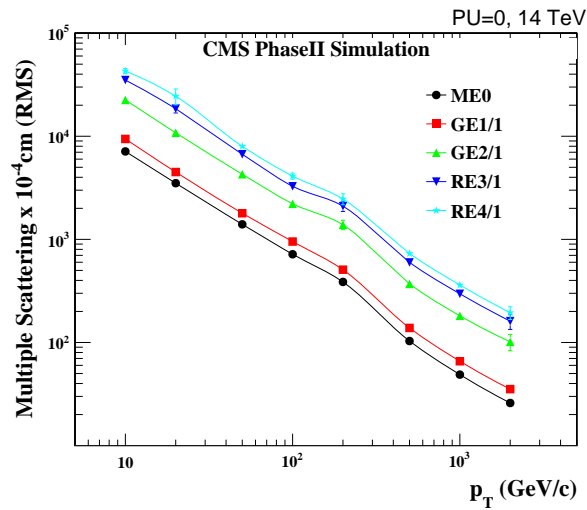


Figure 2.8: A quadrant of the muon system, showing DTs (yellow), RPCs (light blue), and CSCs (green). The locations of new forward muon detectors for Phase-II are contained within the dashed box and indicated in red for GEM stations (ME0, GE1/1, and GE2/1) and dark blue for improved RPC (iRPC) stations (RE3/1 and RE4/1).

923        RPCs are used by the CMS first level trigger for their good timing performances. Indeed, a very  
 924        good bunch crossing identification can be obtained with the present CMS RPC system, given their  
 925        fast response of the order of 1 ns. In order to contribute to the precision of muon momentum mea-  
 926        surements, muon chambers should have a spatial resolution less or comparable to the contribution  
 927        of multiple scattering [21]. Most of the plausible physics is covered only considering muons with  
 928         $p_T < 100$  GeV thus, in order to match CMS requirements, a spatial resolution of  $\mathcal{O}(\text{few mm})$  the  
 929        proposed new RPC stations, as shown by the simulation in figure 2.9. According to preliminary  
 930        designs, RE3/1 and RE4/1 readout pitch will be comprised between 3 and 6 mm and 5  $\eta$ -partitions  
 931        could be considered.



*Figure 2.9: RMS of the multiple scattering displacement as a function of muon p<sub>T</sub> for the proposed forward muon stations. All of the electromagnetic processes such as bremsstrahlung and magnetic field effect are included in the simulation.*

# 3

932

933

## Physics of Resistive plate chambers

934 A Resistive Plate Chamber (RPC) is a gaseous detector using the same physical processes described  
935 in Chapter 3. It has been developed in 1981 by Santonico and Cardarelli [24], under the name of  
936 *Resistive Plate Counter*, as an alternative to the local-discharge spark counters proposed in 1978  
937 by Pestov and Fedotovich [25, 26]. Working with spark chambers implied using high-pressure gas  
938 and high mechanical precision which the RPC simplified by formerly using a gas mixture of argon  
939 and butane flowed at atmospheric pressure and a constant and uniform electric field propagated  
940 in between two parallel electrode plates. Moreover, a significant increase in rate capability was  
941 introduced by the use of electrode plate material with high bulk resistivity, preventing the discharge  
942 from growing throughout the whole gas gap. Indeed, the effect of using resistive electrodes is that  
943 the constant electric field is locally canceled out by the development of the discharge, limiting its  
944 growth.

945 Through its development history, different operating modes [27–29] and new detector designs [30–  
946 32] have been discovered, leading to further improvement of the rate capability of such a detector.  
947 Moreover, the addition of  $SF_6$  into the gas mix improved the stability of operation of the RPC [33,  
948 34].

949 The low developing costs and easily achievable large detection areas offered by RPCs, as well as  
950 the wide range of possible designs, made them a natural choice to as muon chambers and/or trigger  
951 detectors in multipurpose experiments such as CMS [21] or ATLAS [35], time-of-flight detectors in  
952 ALICE [36], calorimeter with CALICE [37] or even detectors for volcanic muography with ToMu-  
953 Vol [38].

### 954 3.1 Principle

955 RPCs are ionisation detectors composed of two parallel resistive plate electrodes in between which  
956 a constant electric field is set. The space in between the electrodes, referred as *gap*, is filled with a  
957 dense gas that is used to generate primary ionization into the gas volume. The free charge carriers  
958 (electrons and cations) created by the ionization of the gas molecules are then accelerated towards

959 the electrodes by the electric field, as shown in Figure 3.1 [39].

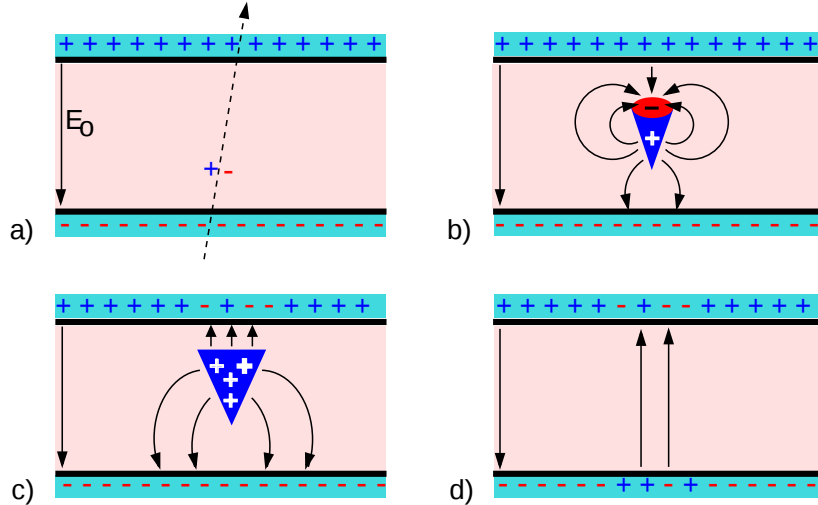


Figure 3.1: Different phases of the avalanche development in the RPC gas volume subjected to a constant electric field  $E_0$ . a) An avalanche is initiated by the primary ionisation caused by the passage of a charged particle through the gas volume. b) Due to its growing size, the avalanche starts to locally influence the electric field. c) The electrons, lighter than the cations reach the anode first. d) The ions reach the cathode. While the charges have not recombined, the electric field in the small region around the avalanche stays affected and locally blind the detector.

960     RPCs being passive detectors, a current on pick-up copper read-out placed outside of the gas  
 961     volume is induced by the charge accumulation during the growth of the avalanche. As a result,  
 962     the time resolution of the detector is substantially increased as the output signal is generated while  
 963     the electrons are still in movement. The advantage of a constant electric field, over multi-wire  
 964     proportional chambers, is that the electrons are being fully accelerated from the moment charge  
 965     carriers are freed and feel the full strength of the electric field that doesn't depend on the distance to  
 966     the readout and that the output signal doesn't need for the electrons to be physically collected.

967     The typical gas mixture RPCs are operated with is generally composed of 3 gas compounds.

- 968     ● Tetrafluoroethane ( $C_2F_4H_2$ ), also referred to as *Freon*, is the principal compound of the RPC  
 969     gas mixtures, with a typical fraction above 90%. It is used for it's high effective Townsend  
 970     coefficient and the great average fast charge that allows to operate the detector with a high  
 971     threshold with respect to argon, for example, that has similar effective Townsend coefficient  
 972     but suffers from a lower fast charge. To operate with similar conditions, argon would require a  
 973     higher electric field leading to a higher fraction of streamers, thus limiting the rate capability  
 974     of the detector [40].
- 975     ● Isobutane (i- $C_4H_{10}$ ), only present in a few percent in the gas mixtures, is used for its UV  
 976     quenching properties [41] helping to prevent streamers due to UV photon emission during the  
 977     avalanche growth.
- 978     ● Sulfur hexafluoride, ( $SF_6$ ), referred to simply as *SF6*, is used in very little quantities for its  
 979     high electronegativity. Excess of electrons are being absorbed by the compound and streamers

are suppressed [34]. Nevertheless, a fraction of  $SF_6$  higher than 1% will not bring any extra benefit in terms of streamer cancelation power but will lead to higher operating voltage [33], as can be understood through Figure 3.2.

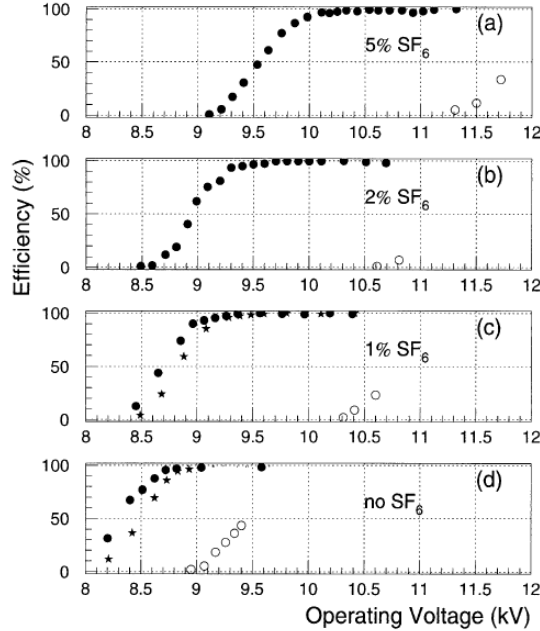


*Figure 3.2: Effeciency (circles and stars with 30 mV and 100 mV thresholds respectively) and streamer probability (opened circles) as function of the operating voltatge of a 2 mm single gap HPL RPC flushed with a gas mixture containing (a) 5%, (b) 2%, (c) 1% and (d) no  $SF_6$  [33].*

After an avalanche developed in the gas, a time long compared to the development of a discharge is needed to recombine the charge carriers in the electrode material due to their resistivity. This property has the advantage of affecting the local electric field and avoiding sparks in the detector but, on the other hand, the rate capability is intrinsically limited by the time constant  $\tau_{RPC}$  of the detector. Using a quasi-static approximation of Maxwell's equations for weakly conducting media, it can be shown that the time constant  $\tau_{RPC}$  necessary to the charge recombination at the interface in between the electrode and the gas volume is given by the Formula 3.1 [42].

$$\tau_{RPC} = \frac{\epsilon_{electrode} + \epsilon_{gas}}{\sigma_{electrode} + \sigma_{gas}} \quad (3.1)$$

A gas can be assimilated to vacuum, leading to  $\epsilon_{gas} = \epsilon_0$  and  $\sigma_{gas} = 0$ , and the electrodes permittivity and conductivity can be written as  $\epsilon_{electrode} = \epsilon_r \epsilon_0$  and  $\sigma_{electrode} = 1/\rho_{electrode}$ , showing the strong dependence of the time constant to the electrodes resistivity in Formula 3.2.

$$\tau_{RPC} = (\epsilon_r + 1)\epsilon_0 \times \rho_{electrode} \quad (3.2)$$

Very few materials with a low enough resistivity exist in nature. The resistivity targeted to build RPCs ranges from  $10^9$  to  $10^{12} \Omega \cdot \text{cm}$ . The most common RPC electrode materials are displayed in Table 3.1. When the doped glass and ceramics can offer short time constants of the order of 1 ms,

996 the developing cost of such materials is quite high due to the very low demand. Thus, High-pressure  
 997 laminate (HPL) is often the choice for high rate experiments using very large RPC detection areas.  
 998 Other experiments working at cosmic muon fluxes can safely operate with ordinary float glass.

Material	$\rho_{electrode}$ ( $\Omega \cdot \text{cm}$ )	$\epsilon_r$	$\tau_{RPC}$ (ms)
Float glass	$10^{12}$	$\sim 7$	$\sim 700$
High-pressure laminate	$10^{10}$ to $10^{12}$	$\sim 6$	$\sim 6$ to 600
Doped glass (LR S)	$10^9$ to $10^{11}$	$\sim 10$	$\sim 1$ to 100
Doped ceramics (SiN/SiC)	$10^9$	$\sim 8.5$	$\sim 1$
Doped ceramics (Ferrite)	$10^8$ to $10^{12}$	$\sim 20$	$\sim 0.2$ to 2000

Table 3.1: Properties of the most used electrode materials for RPCs.

### 999 3.1.1 Electron drift velocity

1000 Talk about the electron drift velocity and mention the time resolution of RPCs.

## 1001 3.2 Rate capability and time resolution of Resistive Plate Cham- 1002 bers

1003 As already previously discussed, the electrode material plays a key role in the max intrinsic rate  
 1004 capability of RPCs. R&D is being done to develop at always cheaper costs material with lower  
 1005 resistivity. Nevertheless, the amount of charge released, i.e. the size of the discharge, if reduced  
 1006 leads to a smaller blind area in the detector, increasing the rate capability of the detector.

### 1007 3.2.1 Operation modes

1008 RPCs where developed early 1980s. At that time it was using an operating mode now referred to  
 1009 as *streamer mode*. Streamers are large discharges that develop in between the 2 electrodes enough  
 1010 to locally discharge the electrodes. If the electric field inside of the gas volume is strong enough,  
 1011 with electrons being fast compared to ions, a large and dense cloud of positive ions will develop  
 1012 nearby the anode and extend toward the cathode while the electrons are being collected, eventually  
 1013 leading to a streamer discharge due to the increase of field seen at the cathode. the field is then strong  
 1014 enough so that electrons are pulled out of the cathode. Electrodes, though they are a unique volume  
 1015 of resistive material, can be assimilated to capacitors. At the moment an electric field is applied in  
 1016 between their outer surfaces, the charge carriers inside of the volume will start moving leading to  
 1017 a situation where there is no voltage across the electrodes and a higher density of negative charges,  
 1018 i.e. electrons, on the inner surface of the cathode. Finally, when a streamer discharge occurs, these  
 1019 electrons are partially released in the gas volume contributing to increase the discharge strength until  
 1020 the formation of a conductive plasma, the streamer. This can be understood through Figure 3.3 [27].  
 1021 Streamer signals are very convenient in terms of read-out as no amplification is required with output  
 1022 pulses amplitudes of the order of a few tens to few hundreds of mV as can be seen on Figure 3.4.

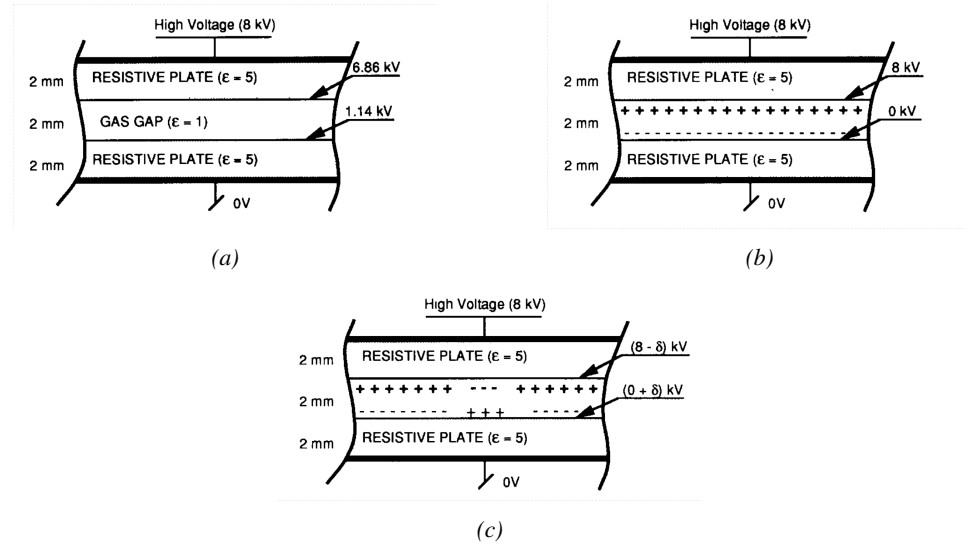


Figure 3.3: Movement of the charge carriers in an RPC. Figure 3.3a: Voltage across an RPC whose electrode have a relative permittivity of 5 at the moment the tension is applied. Figure 3.3b: After the charge carriers moved, the electrodes are charged and there is no voltage drop over the electrodes anymore. The full potential is applied on the gas gap only. Figure 3.3c: The streamer discharge initiated by a charged particle transports electrons and cations towards the anode and cathode respectively.

When the electric field is reduced though, the electronic gain is small until the electrons get close enough to the anode and the positive ion cloud is much smaller. The electric field cannot rise to the point a field emission of electrons on the cathode is possible. The resulting signal is weak, of the order of a few mv as shown on Figure 3.4, and requires amplification. This is the *avalanche mode* of RPC operation.

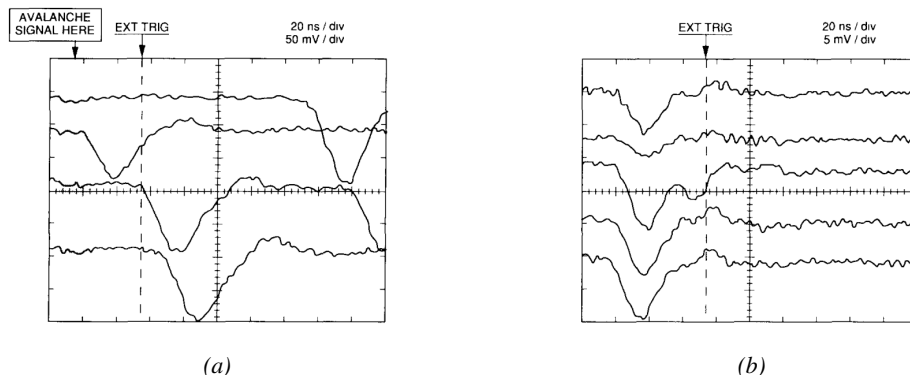


Figure 3.4: Typical oscilloscope pulses in streamer mode (Figure 3.4a) and avalanche mode (Figure 3.4b). In the case of streamer mode, the very small avalanche signal is visible.

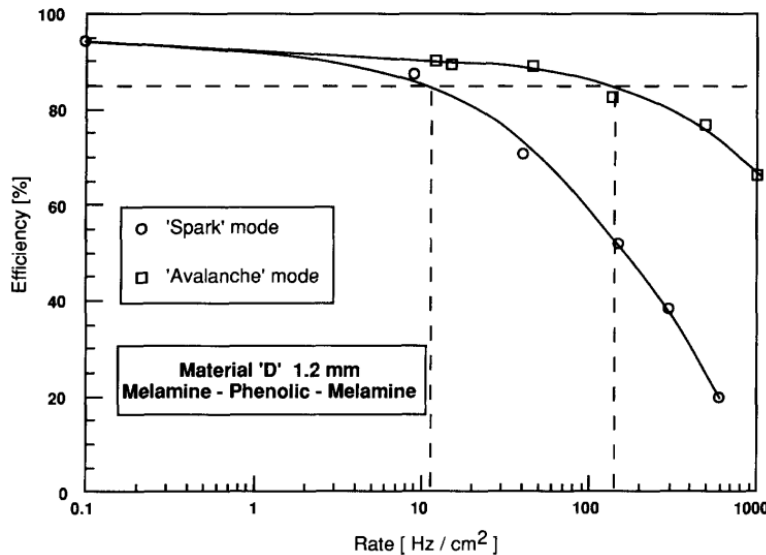


Figure 3.5: Rate capability comparison for the streamer and avalanche mode of operation. An order of magnitude in rate capability for a maximal efficiency drop of 10% is gained by using the avalanche mode over the streamer mode.

This mode offers a higher rate capability by providing smaller discharges that don't affect the electrodes charge and are more locally contained in the gas volume as was demonstrated by Crotty with Figure 3.5 [27]. The detector only stays locally blind the time the charge carriers are recombined and there is no need for electrode recharge which is a long process affecting a large portion of the detector. Another advantage of avalanche signals over streamer is the great time consistency. Figure 3.4 shows very clearly that avalanche signals have a very small time jitter. This is a natural choice for high rate experiments.

### 3.2.2 Detector designs and performance

Different RPC design have been used and each of them present its own advantages. Historically, the first type of RPC to have been developed is what is referred now to *narrow gap* RPC [24, 43]. After the avalanche mode has been discovered [27], it has been proven that increasing the width of the gas gap lead to higher rate capability, due to lower charge deposition per avalanche, and lower power dissipation [43]. Nevertheless, by increasing the gas gap width, the time resolution of the detector decreases. This is a natural result if the increase of active gas volume in the detector is taken into account. Indeed, for a given threshold, only the small fraction of gas closest to the cathode will provide enough gain to have a detectable signal. In the case of a wider gas volume, the active region is then larger and a larger time jitter is introduced with the variation of starting position of the avalanche, as discussed in [30]. To solve improve both the time resolution and the rate capability, different methods were used trying to get advantages of both narrow and wide gap RPCs.

### 3.2.2.1 Double-gap RPC

Double-gap RPCs are made out of 2 narrow RPC detectors. The 2 RPC gaps are stacked on top of each other as shown in Figure 3.6. This detector layout, popularized by the two multipurpose experiments CMS [21] and ATLAS [35] at LHC, can be used as an OR system in which each individual chamber participates in the output signal. The gain of such a detector is greatly reduced with respect to single-gap RPCs with an efficiency plateau reached at lower voltage, as visible on Figure 3.7.

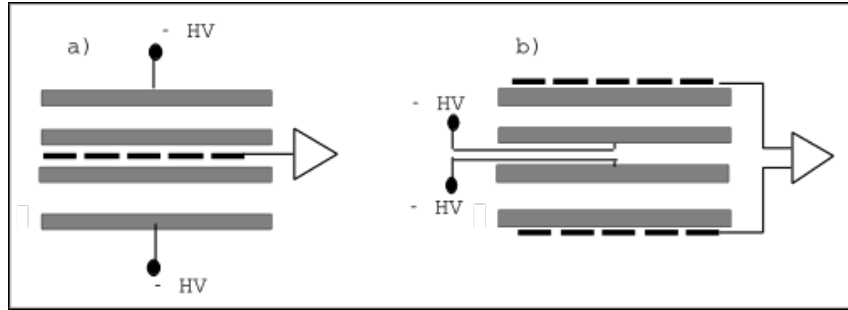


Figure 3.6: Possible double-gap RPC layouts: a) "standard" 1D double-gap RPC, as used in CMS experiment, where the anodes are facing each other and a 1D read-out plane is sandwiched in between them, b) double read-out double-gap RPC as used in ATLAS experiment, where the cathodes are facing each other and 2 read-out planes are used on the outer surfaces. This last layout can offer the possibility to use a 2D reconstruction by using orthogonal read-out planes.

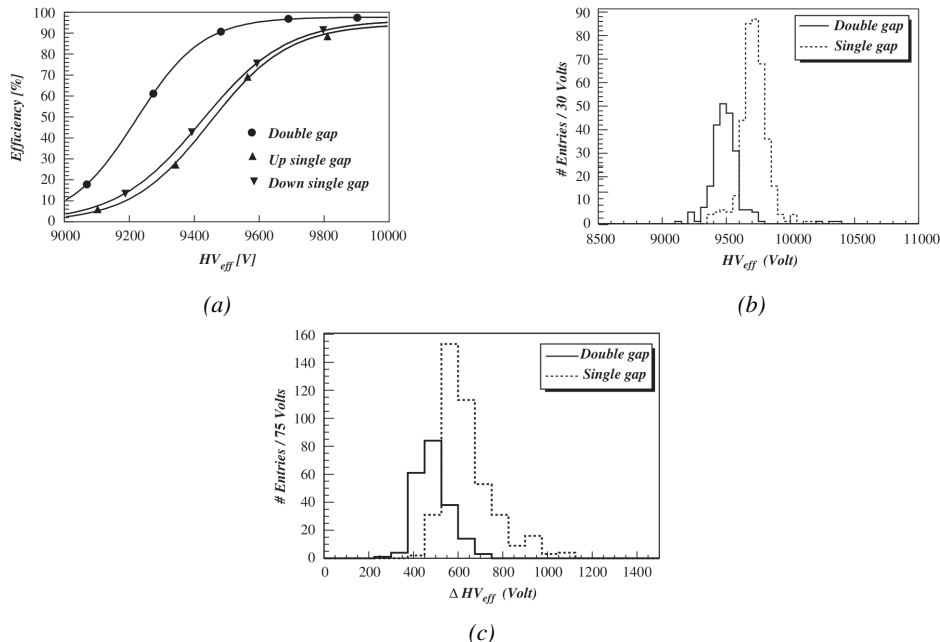


Figure 3.7: Comparison of performance of CMS double and single gap RPCs using cosmic muons [44]. Figure 3.7a: Comparison of efficiency sigmoids. Figure 3.7b: Voltage distribution at 95% of maximum efficiency. Figure 3.7c:  $\Delta_{10\%}^{90\%}$  distribution.

1053 **3.2.2.2 Multigap RPC (MRPC)**

1054 MRPCs are layouts in which floating sub electrode plates are placed into a wide gap RPC to divide  
 1055 the gas volume and create a sum of narrow gaps [30, 31]. The time resolution of such a detector can  
 1056 reach of few tens of ps, with gas gaps of the order of a few hundred  $\mu\text{m}$  as shown in Figure 3.8  
 1057 representing ALICE Time-of-flight (ToF) MRPCs.

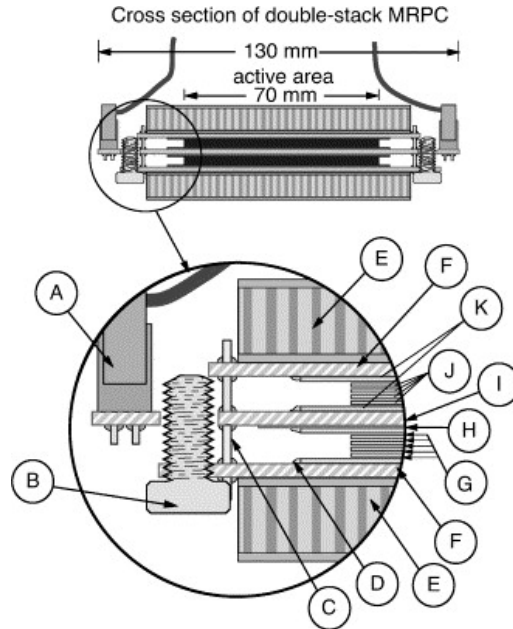


Figure 3.8: Presentation of ALICE MRPC using  $250 \mu\text{m}$  gas gaps,  $620 \mu\text{m}$  outer glass electrodes and  $550 \mu\text{m}$  inner floating electrodes. More details on the labels are given in [45].

1058 Sometimes used as a double multigap RPC, taking advantage of the OR of double gap RPCs,  
 1059 the MRPC is mainly used as ToF detector [45–49] due to its excellent timing properties that allow  
 1060 to perform particle identification as explained by Williams in [50]. The principle of particle iden-  
 1061 tification using ToF is simply the measurement of the velocity of a particle. Indeed, particles are  
 1062 defined by their mass (for the parameter of interest here, their electric charge being measured using  
 1063 the bending angle of the particles traveling through a magnetic field) and this mass can be calculated  
 1064 by measuring the velocity  $\beta$  and momentum of the particle:

$$\beta = \frac{p}{\sqrt{p^2 + m^2}} \quad (3.3)$$

1065 Intuitively, it is trivial to understand that 2 different particles having the same momentum will  
 1066 have a different velocity due to the mass difference and thus a different flight time  $T_1$  and  $T_2$  through  
 1067 the detector and this is used to separate and identify particles. The better the time resolution of the  
 1068 ToF system used, the stronger will the separation be:

$$T = \frac{L}{v} = \frac{L}{c \cdot \beta}, \quad \Delta T = T_1 - T_2 = \frac{L}{c} \left( \sqrt{1 + m_1^2/p^2} - \sqrt{1 + m_2^2/p^2} \right) \cong (m_1^2 - m_2^2) \frac{L}{2cp^2} \quad (3.4)$$

1069 An example of particle identification is given for the case of STAR experiment in Figure 3.9.

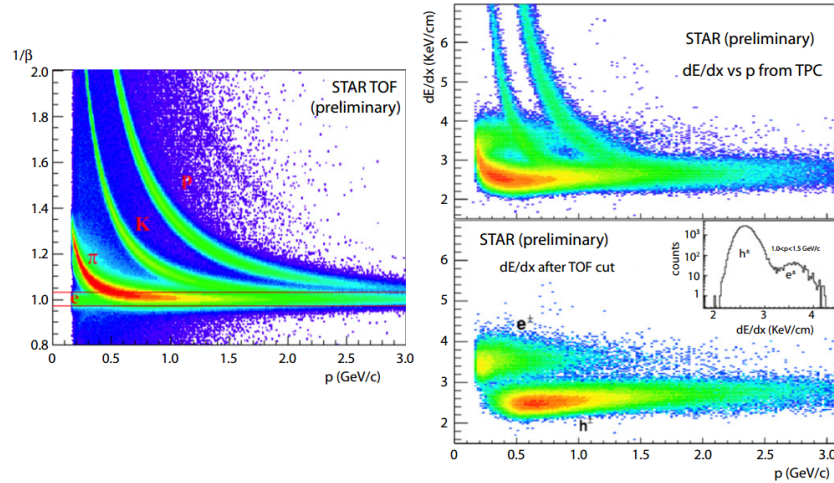


Figure 3.9: Particle identification applied to electrons in the STAR experiment. The identification is performed combining ToF and  $dE/dx$  measurements [50].

1070 Another benefice of using such small gas gaps is the strong reduction of the average avalanche  
1071 volume and thus of the blind spot on MRPCs leading to an improved rate capability. Multigaps can  
1072 sustain backgrounds of several kHz/cm<sup>2</sup> as demonstrated in Figure 3.10.

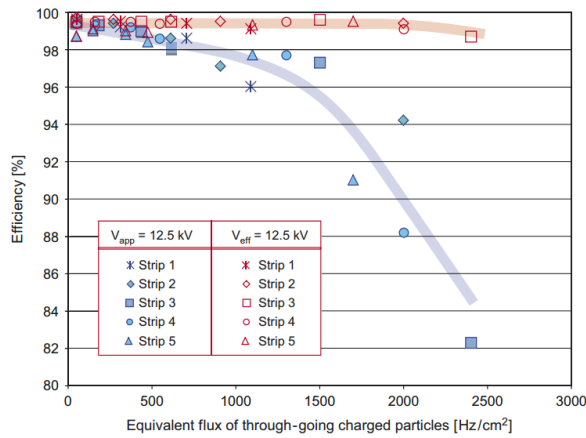


Figure 3.10: Comparison of the detector performance of ALICE ToF MRPC [51] at fixed applied voltage (in blue) and at fixed effective voltage (in red). The effective voltage is kept fixed by increasing the applied voltage accordingly to the current drawn by the detector.

### 1073 3.2.2.3 Charge distribution and performance limitations

1074 The direct consequence of the different RPC layouts is a variation of intrinsic time resolution of the  
1075 RPC as the gap size decreases. An advantage is given to multigaps whose design use sub-millimeter  
1076 gas volumes providing very consistent signals.

1077 On the charge spectrum point of view, each layout has its own advantages. When the double-gap  
 1078 has the highest induced over drifting charge ratio, as seen in Figure 3.11, the multigap has a charge  
 1079 spectrum strongly detached from the origin, as visible in Figure 3.12. A high induced over drifting  
 1080 charge ratio means that the double gap can be safely operated at high threshold or that at similar  
 1081 threshold it can be operated with a twice smaller drifting charge, meaning a higher rate capability.  
 1082 On the other hand, the strong detachment of the charge spectrum from the origin in the MRPC case  
 1083 allows to reach a higher efficiency with increasing threshold as most of the induced charge is not low  
 1084 due to the convolution of several single gap spectra. The range of stable efficiency increases with  
 1085 the number of gap, as presented in Figure 3.13.

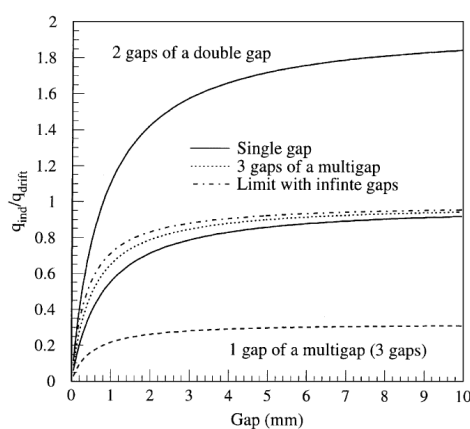


Figure 3.11: Ratio between total induced and drifting charge have been simulated for single gap, double-gap and multigap layouts [52]. The total induced charge for a double-gap RPC is a factor 2 higher than for a multigap.

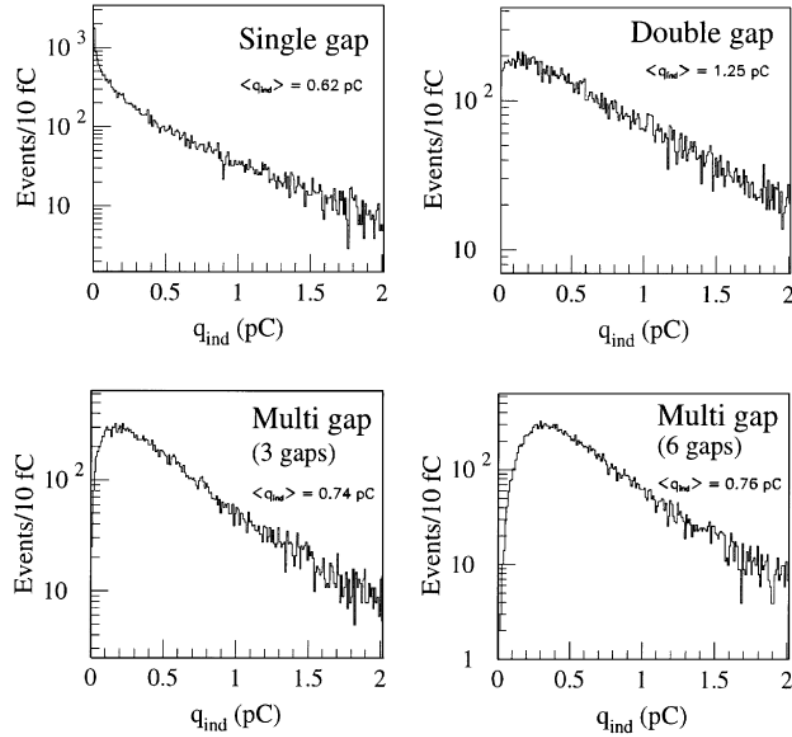


Figure 3.12: Charge spectra have been simulated for single gap, double-gap and multigap layouts [52]. It appears that when single gap shows a decreasing spectrum, double and multigap layouts exhibit a spectrum whose peak is detached from the origin. The detachment gets stronger as the number of gaps increases.

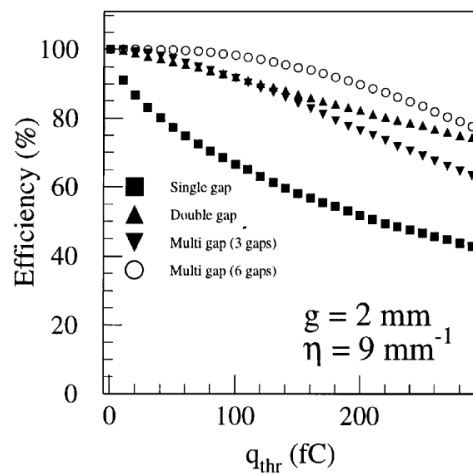


Figure 3.13: The maximal theoretical efficiency is simulated for single gap, double-gap and multigap layouts [52] at a constant gap thickness of 2 mm and using an effective Townsend coefficient of  $9 \text{ mm}^{-1}$ .

<sup>1086</sup> **3.3 Signal formation**

<sup>1087</sup> **3.4 Gas transport parameters**

# 4

1088

1089

1090

## Longevity studies and Consolidation of the present CMS RPC subsystem

### 4.1 Resistive Plate Chambers at CMS

#### 4.1.1 Overview

1093 The Resistive Plate Chambers (RPC) system, located in both barrel and endcap regions, provides a  
1094 fast, independent muon trigger with a looser  $p_T$  threshold over a large portion of the pseudorapidity  
1095 range ( $|\eta| < 1.6$ ) [add reconstruction].

1096

1097 During High-Luminosity LHC (HL-LHC) operations the expected conditions in terms of back-  
1098 ground and pile-up will make the identification and correct  $P_T$  assignment a challenge for the Muon  
1099 system. The goal of RPC upgrade is to provide additional hits to the Muon system with precise tim-  
1100 ing. All these informations will be elaborated by the trigger system in a global way enhancing the  
1101 performance of the trigger in terms of efficiency and rate control. The RPC Upgrade is based on two  
1102 projects: an improved Link Board System and the extension of the RPC coverage up to  $|\eta| = 2.4$ .  
1103 [FIXME 2.4 or 2.5?]

1104 The Link Board system, that will be described in section xxx, is responsible to process, syn-  
1105 chronize and zero-suppress the signals coming from the RPC front end boards. The Link Board  
1106 components have been produced between 2006 and 2007 and will be subjected to aging and failure  
1107 in the long term. The upgraded Link Board system will overcome the aging problems described in  
1108 section xxx and will allow for a more precise timing information to the RPC hits from 25 to 1 ns [ref  
1109 section xxx].

1110 The extension of the RPC system up to  $|\eta| = 2.1$  was already planned in the CMS TDR [ref  
1111 cmstdr] and staged because of budget limitations and expected background rates higher than the rate  
1112 capability of the present CMS RPCs in that region. An extensive R&D program has been done in  
1113 order to develop an improved RPC that fulfills the CMS requirements. Two new RPC layers in the  
1114 innermost ring of stations 3 and 4 will be added with benefits to the neutron-induced background

1115 reduction and efficiency improvement for both trigger and offline reconstruction.

### 1116 4.1.2 The present RPC system

1117 The RPC system is organized in 4 stations called RB1 to RB4 in the barrel region, and RE1 to RE4  
 1118 in the endcap region. The innermost barrel stations, RB1 and RB2, are instrumented with 2 layers  
 1119 of RPCs facing the innermost (RB1in and RB2in) and outermost (RB1out and RB2out) sides of the  
 1120 DT chambers. Every chamber is then divided from the read-out point of view into 2 or 3  $\eta$  partitions  
 1121 called “rolls”. The RPC system consist of 480 barrel chambers and 576 endcap chambers. Details  
 1122 on the geometry are discussed in the paper [ref to geo paper].

1123 The CMS RPC chamber is a double-gap, operated in avalanche mode to ensure reliable operation  
 1124 at high rates. Each RPC gap consists of two 2-mm-thick resistive High-Pressure Laminate (HPL)  
 1125 plates separated by a 2-mm-thick gas gap. The outer surface of the HPL plates is coated with a thin  
 1126 conductive graphite layer, and a voltage is applied. The RPCs are operated with a 3-component,  
 1127 non-flammable gas mixture consisting of 95.2% freon ( $C_2H_2F_4$ , known as R134a), 4.5% isobutane  
 1128 ( $i-C_4H_{10}$ ), and 0.3% sulphur hexafluoride ( $SF_6$ ) with a relative humidity of 40% - 50%. Readout  
 1129 strips are aligned in  $\eta$  between the 2 gas gaps. [\[Add a sentence on FEBs.\]](#)

1130 The discriminated signals coming from the Front End boards feed via twisted cables (10 to 20 m  
 1131 long) the Link Board System located in UXC on the balconies around the detector. The Link System  
 1132 consist of the 1376 Link Boards (LBs) and the 216 Control Boards (CBs), placed in 108 Link Boxes.  
 1133 The Link Box is a custom crate (6U high) with 20 slots (for two CBs and eighteen LBs). The Link  
 1134 Box contains custom backplane to which the cables from the chambers are connected, as well as the  
 1135 cables providing the LBs and CBs power supply and the cables for the RPC FEBs control with use  
 1136 of the I2C protocol (trough the CB). The backplane itself contains only connectors (and no any other  
 1137 electronic devices).

1138 The Link Board has 96 input channels (one channel corresponds to one RPC strip). The input  
 1139 signals are the  $\sim 100$  ns binary pulses which are synchronous to the RPC hits, but not to the LHC  
 1140 clock (which drives the entire CMS electronics). Thus the first step of the FEB signals processing  
 1141 is synchronization, i.e. assignment of the signals to the BXes (25 ns periods). Then the data are  
 1142 compressed with a simple zero-suppressing algorithm (the input channels are grouped into 8 bit  
 1143 partitions, only the partitions with at least one nonzero bit are selected for each BX). Next, the non-  
 1144 empty partitions are time-multiplexed i.e. if there are more than one such partition in a given BX,  
 1145 they are sent one-by-one in consecutive BXes. The data from 3 neighbouring LBs are concentrated  
 1146 by the middle LB which contains the optical transmitter for sending them to the USC over a fiber at  
 1147 1.6 Gbps.

1148 The Control Boards provide the communication of the control software with the LBs via the  
 1149 FEC/CCU system. The CBs are connected into token rings, each ring consists of 12 CBs of one  
 1150 detector tower and a FEC mezzanine board placed on the CCS board located in the VME crate in  
 1151 the USC. In total, there are 18 rings in the entire Link System. The CBs also perform automatic  
 1152 reloading of the LB's firmware which is needed in order to avoid accumulation of the radiation  
 1153 induced SEUs in the LBs firmware.

1154 Both LBs and CB are based on the Xilinx Spartan III FPGAs, the CB additionally contains  
 1155 radiation-tolerant (FLASH based) FPGA Actel ProAsicPlus.

1156 The High Voltage power system is located in USC, not exposed to radiation and easily accessible  
 1157 for any reparation. A single HV channel powers 2 RPC chambers both in the barrel and endcap  
 1158 regions. The Low Voltage boards are located in UXC on the balconies and provide the voltage to the

<sup>1159</sup> front end electronics.

### <sup>1160</sup> 4.1.3 Pulse processing of CMS RPCs

<sup>1161</sup> Signals induced by cosmic particle in the RPC strips are shaped by standard CMS RPC Front-End  
<sup>1162</sup> Electronics (FEE) following the scheme of Figure 4.1. On a first stage, analogic signals are amplified  
<sup>1163</sup> and then sent to the Constant Fraction Discriminator (CFD) described in Figure 4.2. At the end of  
<sup>1164</sup> the chain, 100 ns long pulses are sent in the LVDS output. These output signal are sent on one side to  
<sup>1165</sup> a V1190A Time-to-Digital Converter (TDC) module from CAEN and on the other to an OR module  
<sup>1166</sup> to count the number of detected signals. Trigger and hit coïncidences are monitored using scalers.  
<sup>1167</sup> The TDC is used to store the data into ROOT files. These files are thus analysed to understand the  
<sup>1168</sup> detectors performance.

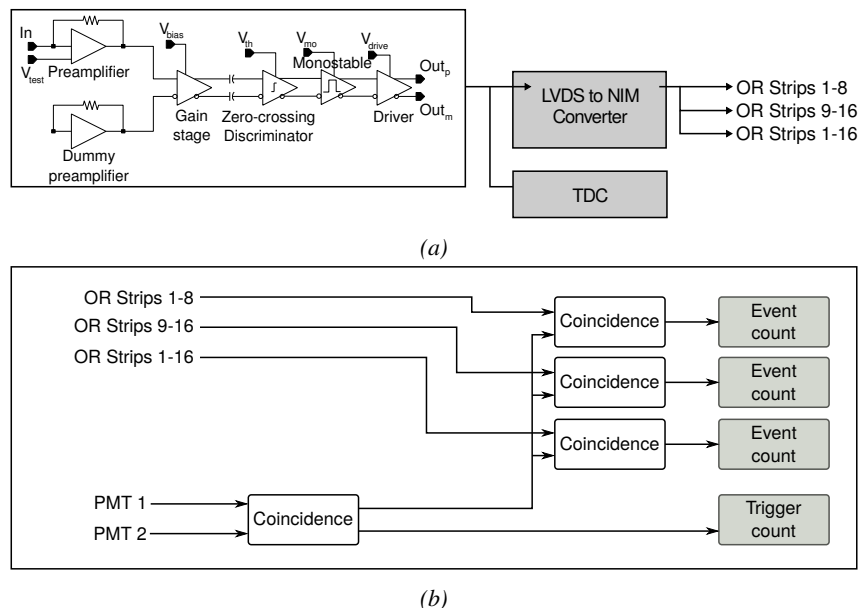


Figure 4.1: Signals from the RPC strips are shaped by the FEE described on Figure 4.1a. Output LVDS signals are then read-out by a TDC module connected to a computer or converted into NIM and sent to scalers. Figure 4.1b describes how these converted signals are put in coincidence with the trigger.

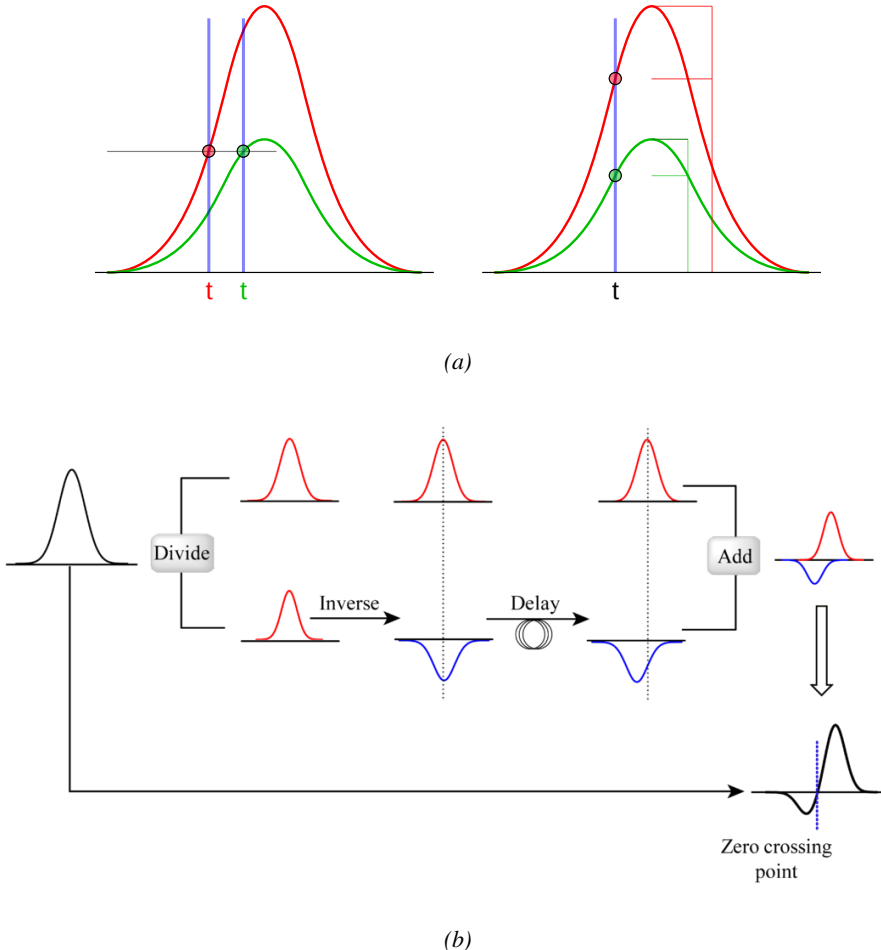


Figure 4.2: Description of the principle of a CFD. A comparison of threshold triggering (left) and constant fraction triggering (right) is shown in Figure 4.2a. Constant fraction triggering is obtained thanks to zero-crossing technique as explained in Figure 4.2b. The signal arriving at the input of the CFD is split into three components. A first one is delayed and connected to the inverting input of a first comparator. A second component is connected to the noninverting input of this first comparator. A third component is connected to the noninverting input of another comparator along with a threshold value connected to the inverting input. Finally, the output of both comparators is fed through an AND gate.

## 4.2 Testing detectors under extreme conditions

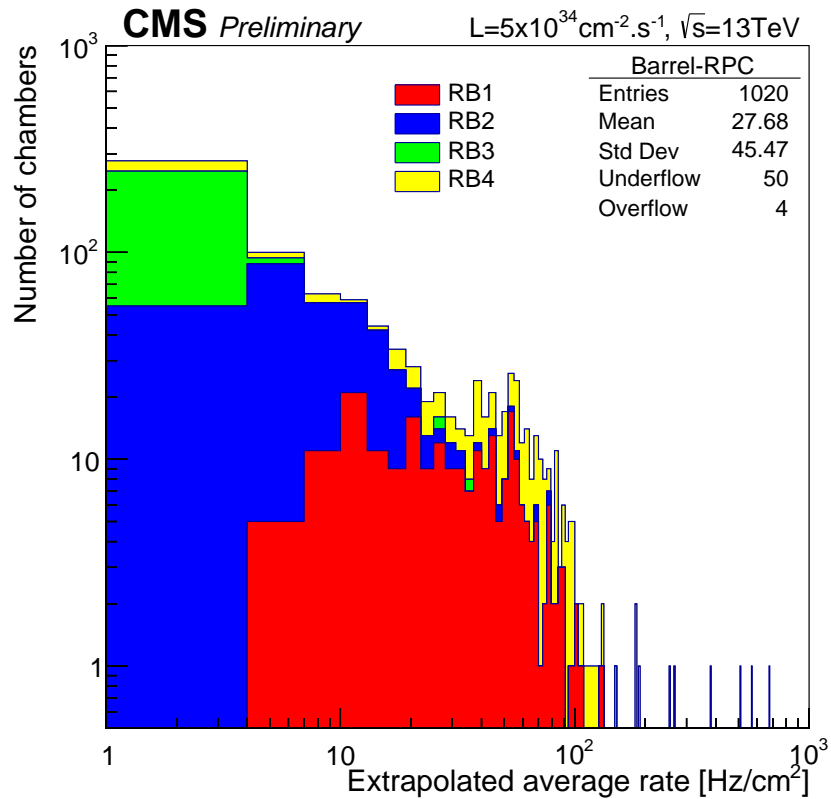
The upgrade from LHC to HL-LHC will increase the peak luminosity from  $10^{34} \text{ cm}^{-2} \text{ s}^{-1}$  to reach  $5 \times 10^{34} \text{ cm}^{-2} \text{ s}^{-1}$ , increasing in the same way the total expected background to which the RPC system will be subjected to. Composed of low energy gammas and neutrons from  $p\text{-}p$  collisions, low momentum primary and secondary muons, puch-through hadrons from calorimeters, and particles produced in the interaction of the beams with collimators, the background will mostly affect the regions of CMS that are the closest to the beam line, i.e. the RPC detectors located in the endcaps.

[To update.]

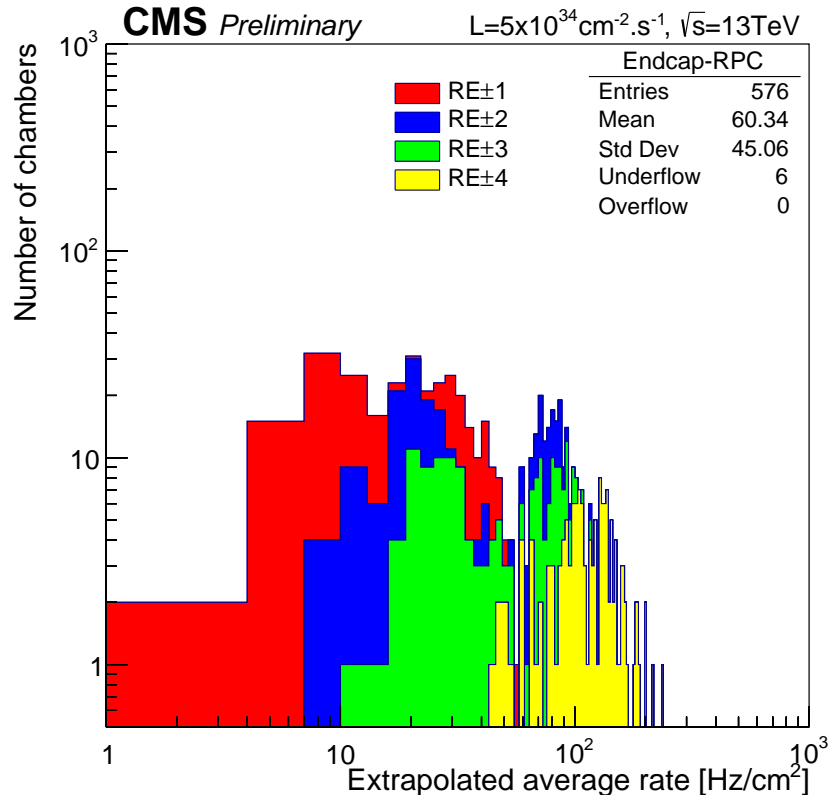
1177

1178       The 2016 data allowed to study the values of the background rate in all RPC system. In Fig-  
1179       ure 4.3, the distribution of the chamber background hit rate per unit area is shown at a luminosity  
1180       of  $5 \times 10^{34} cm^{-2}.s^{-1}$  linearly extrapolating from data collected in 2016 [ref mentioning the linear  
1181       dependency of rate vs lumi]. The maximum rate per unit area at HL-LHC conditions is expected to  
1182       be of the order of  $600 Hz/cm^2$  (including a safety factor 3). Nevertheless, Fluka simulations have  
1183       conducted in order to understand the background at HL-LHC conditions. The comparison to the  
1184       data has shown, in Figure 4.4, a discrepancy of a factor 2 even though the order of magnitude is  
1185       consistent. [Understand mismatch.]

1186



(a)



(b)

Figure 4.3: (4.3a) Extrapolation from 2016 data of single hit rate per unit area in the barrel region. (4.3b) Extrapolation from 2016 data of single hit rate per unit area in the endcap region.

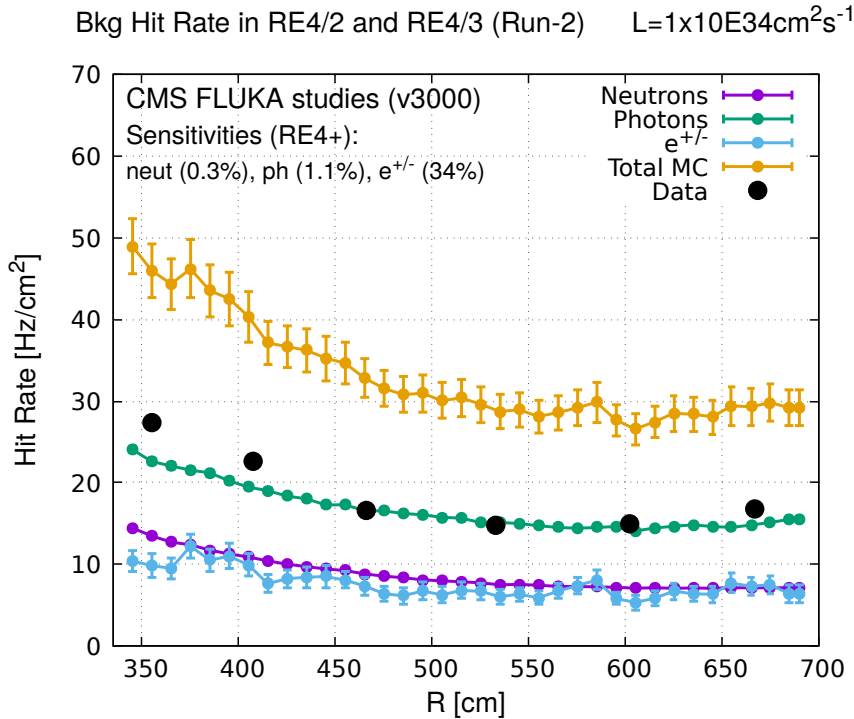


Figure 4.4: Background Fluka simulation compared to 2016 Data at  $L = 10^{34} \text{ cm}^{-2} \cdot \text{s}^{-1}$  in the fourth endcap disk region. A mismatch in between simulation and data can be observed. [\[To be understood.\]](#)

In the past, extensive long-term tests were carried out at several gamma and neutron facilities certifying the detector performance. Both full size and small prototype RPCs have been irradiated with photons up to an integrated charge of  $\sim 0.05 \text{ C}/\text{cm}^2$  and  $\sim 0.4 \text{ C}/\text{cm}^2$ , respectively [53, 54]. During Run-I, the RPC system provided stable operation and excellent performance and did not show any aging effects for integrated charge of the order of  $0.01 \text{ C}/\text{cm}^2$ . Projections on currents from 2016 Data, has allowed to determine that the total integrated charge, by the end of HL-LHC, would be of the order of  $1 \text{ C}/\text{cm}^2$  (including a safety factor 3). [\[Corresponding figure needed.\]](#)

1194

## 1195 4.2.1 The Gamma Irradiation Facilities

### 1196 4.2.1.1 GIF

1197 Located in the SPS West Area at the downstream end of the X5 test beam, the Gamma Irradiation  
 1198 Facility (GIF) was a test area in which particle detectors were exposed to a particle beam in presence  
 1199 of an adjustable gamma background [55]. Its goal was to reproduce background conditions these  
 1200 detectors would suffer in their operating environment at LHC. GIF layout is shown in Figure 4.5.  
 1201 Gamma photons are produced by a strong  $^{137}\text{Cs}$  source installed in the upstream part of the zone  
 1202 inside a lead container. The source container includes a collimator, designed to irradiate a  $6 \times 6 \text{ m}^2$   
 1203 area at 5 m maximum to the source. A thin lens-shaped lead filter helps providing with a uniform  
 1204 outgoing flux in a vertical plane, orthogonal to the beam direction. The principal collimator hole  
 1205 provides a pyramidal aperture of  $74^\circ \times 74^\circ$  solid angle and provides a photon flux in a pyramidal vol-

ume along the beam axis. The photon rate is controled by further lead filters allowing the maximum rate to be limited and to vary within a range of four orders of magnitude. Particle detectors under test are then placed within the pyramidal volume in front of the source, perpendicularly to the beam line in order to profit from the homogeneous photon flux. Adjusting the background flux of photons can then be done by using the filters and choosing the position of the detectors with respect to the source.

1211

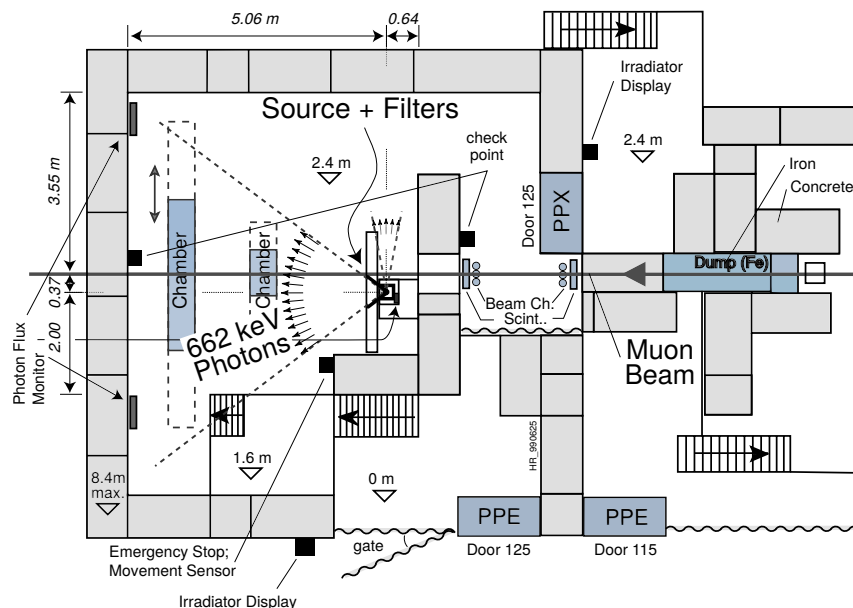


*Figure 4.5: Layout of the test beam zone called X5c GIF at CERN. Photons from the radioactive source produce a sustained high rate of random hits over the whole area. The zone is surrounded by 8 m high and 80 cm thick concrete walls. Access is possible through three entry points. Two access doors for personnel and one large gate for material. A crane allows installation of heavy equipment in the area.*

As described on Figure 4.6, the  $^{137}\text{Cs}$  source emits a 662 keV photon in 85% of the decays. An activity of 740 GBq was measured on the 5<sup>th</sup> March 1997. To estimate the strength of the flux in 2014, it is necessary to consider the nuclear decay through time assiciated to the Cesium source whose half-life is well known ( $t_{1/2} = (30.05 \pm 0.08)$  y). The GIF tests where done in between the 20<sup>th</sup> and the 31<sup>st</sup> of August 2014, i.e. at a time  $t = (17.47 \pm 0.02)$  y resulting in an attenuation of the activity from 740 GBq in 1997 to 494 GBq in 2014.

1218

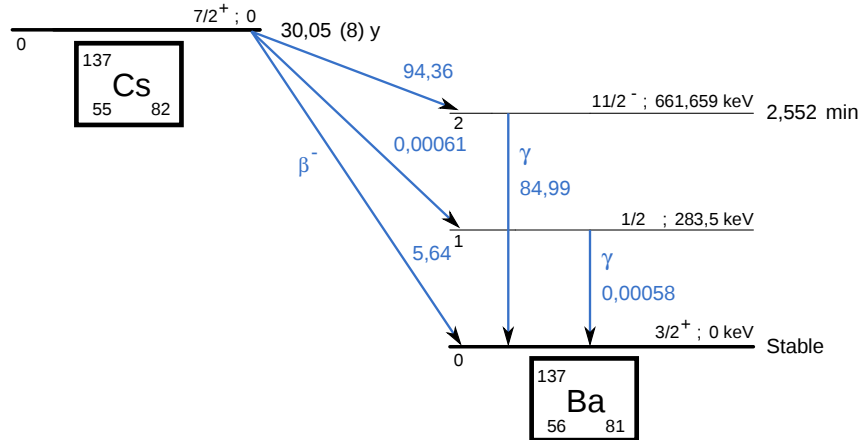


Figure 4.6:  $^{137}\text{Cs}$  decays by  $\beta^-$  emission to the ground state of  $^{137}\text{Ba}$  ( $BR = 5.64\%$ ) and via the 662 keV isomeric level of  $^{137}\text{Ba}$  ( $BR = 94.36\%$ ) whose half-life is 2.55 min.

#### 4.2.1.2 GIF++

The new Gamma Irradiation Facility (GIF++), located in the SPS North Area at the downstream end of the H4 test beam, has replaced its predecessor during LS1 and has been operational since spring 2015 [56]. Like GIF, GIF++ features a  $^{137}\text{Cs}$  source of 662 keV gamma photons, their fluence being controlled with a set of filters of various attenuation factors. The source provides two separated large irradiation areas for testing several full-size muon detectors with continuous homogeneous irradiation, as presented in Figure 4.7.

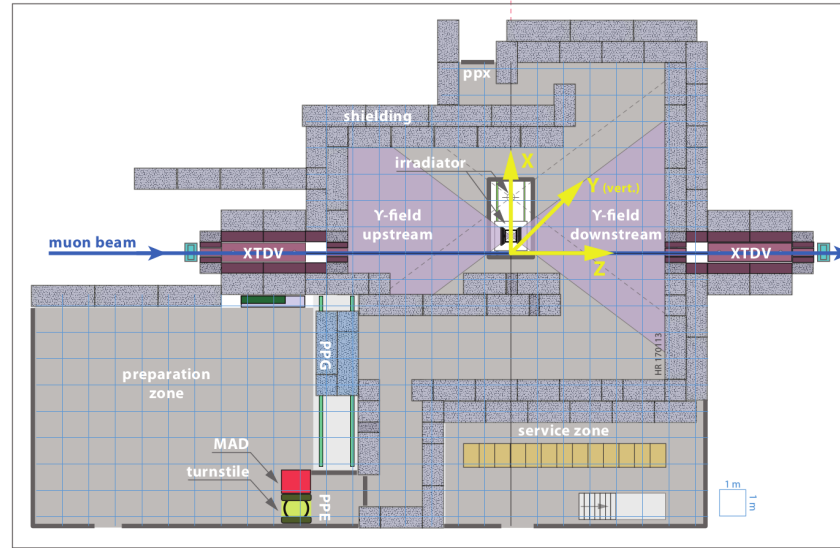


Figure 4.7: Floor plan of the GIF++ facility. When the facility downstream of the GIF++ takes electron beam, a beam pipe is installed along the beam line ( $z$ -axis). The irradiator can be displaced laterally (its center moves from  $x = 0.65$  m to 2.15 m), to increase the distance to the beam pipe.

1227 The source activity was measured to be about 13.5 TBq in March 2016. The photon flux being  
 1228 far greater than HL-LHC expectations, GIF++ provides an excellent facility for accelerated aging  
 1229 tests of muon detectors.

1230

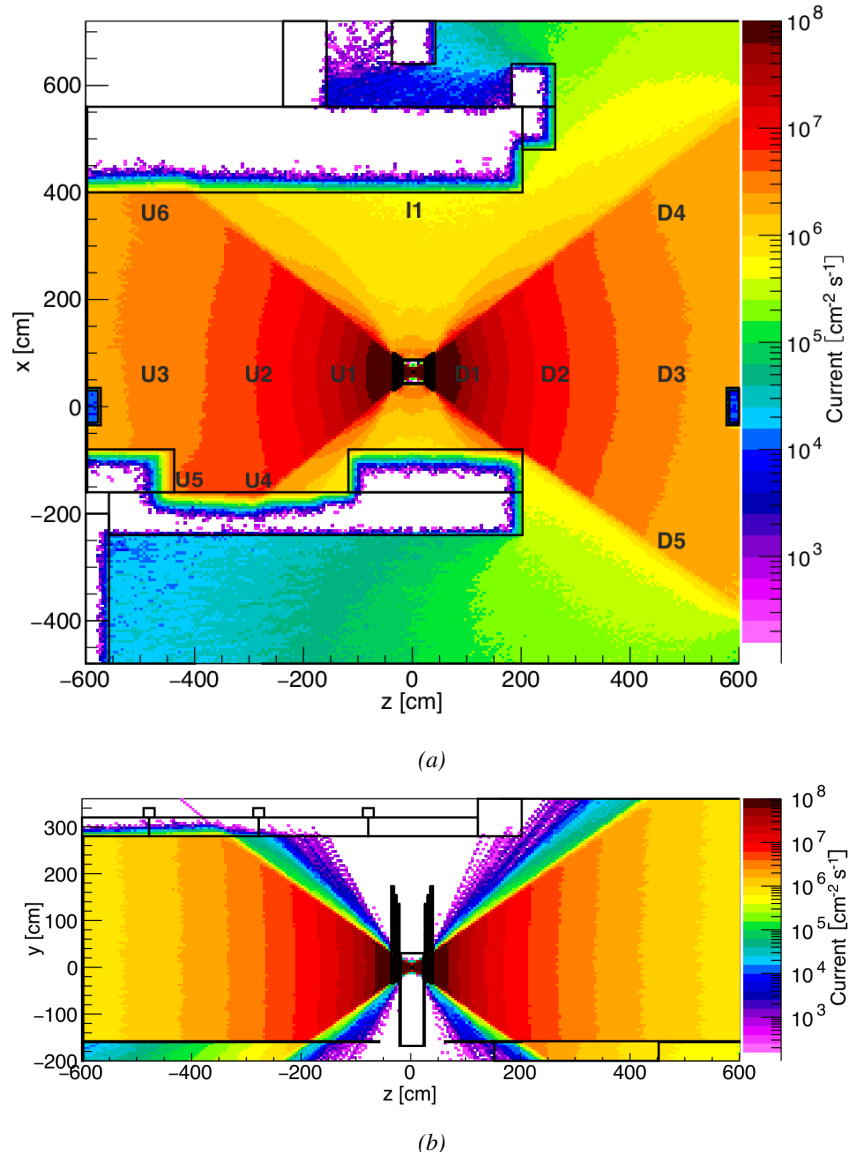


Figure 4.8: Simulated unattenuated current of photons in the xz plane (Figure 4.8a) and yz plane (Figure 4.8b) through the source at  $x = 0.65 \text{ m}$  and  $y = 0 \text{ m}$ . With angular correction filters, the current of 662 keV photons is made uniform in xy planes.

1231 The source is situated in the muon beam line with the muon beam being available a few times a  
 1232 year. The H4 beam, composed of muons with a momentum of about 150 GeV/c, passes through the  
 1233 GIF++ zone and is used to study the performance of the detectors. Its flux is of  $104 \text{ particles/s/cm}^2$

1234 focused in an area similar to  $10 \times 10 \text{ cm}^2$ . Therefore, with properly adjusted filters, one can imitate  
 1235 the HL-LHC background and study the performance of muon detectors with their trigger/readout  
 1236 electronics in HL-LHC environment.

1237

## 1238 4.3 Preliminary tests at GIF

### 1239 4.3.1 Resistive Plate Chamber test setup

1240 During summer 2014, preliminary tests have been conducted in the GIF area on a newly produced  
 1241 RE4/2 chamber labelled RE-4-2-BARC-161. This chamber has been placed into a trolley covered  
 1242 with a tent. The position of the RPC inside the tent and of the tent related to the source is described  
 1243 in Figure 4.9. To test this CMS RPC, three different absorber settings were used. First of all,  
 1244 measurements were done with fully opened source. Then, to complete this preliminary study, the  
 1245 gamma flux has been attenuated from a factor 2 and a factor 5. The expected gamma flux at the level  
 1246 of our detector will be discussed in subsection ??.

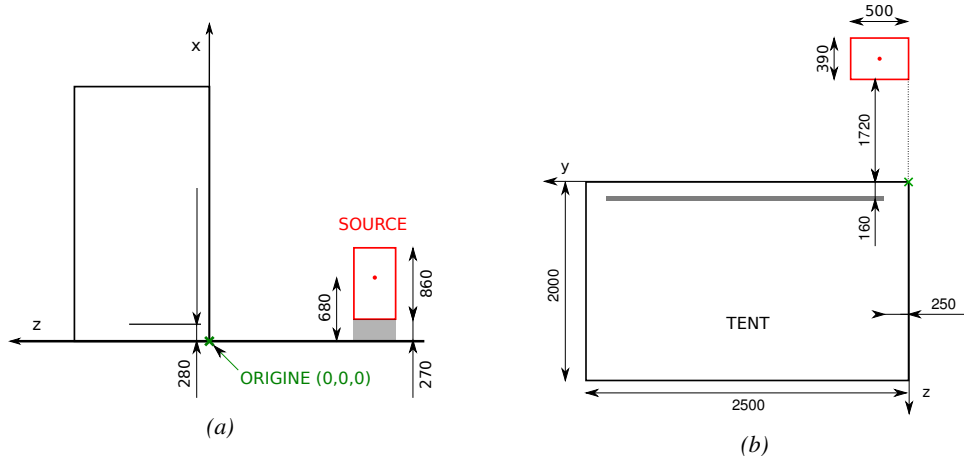
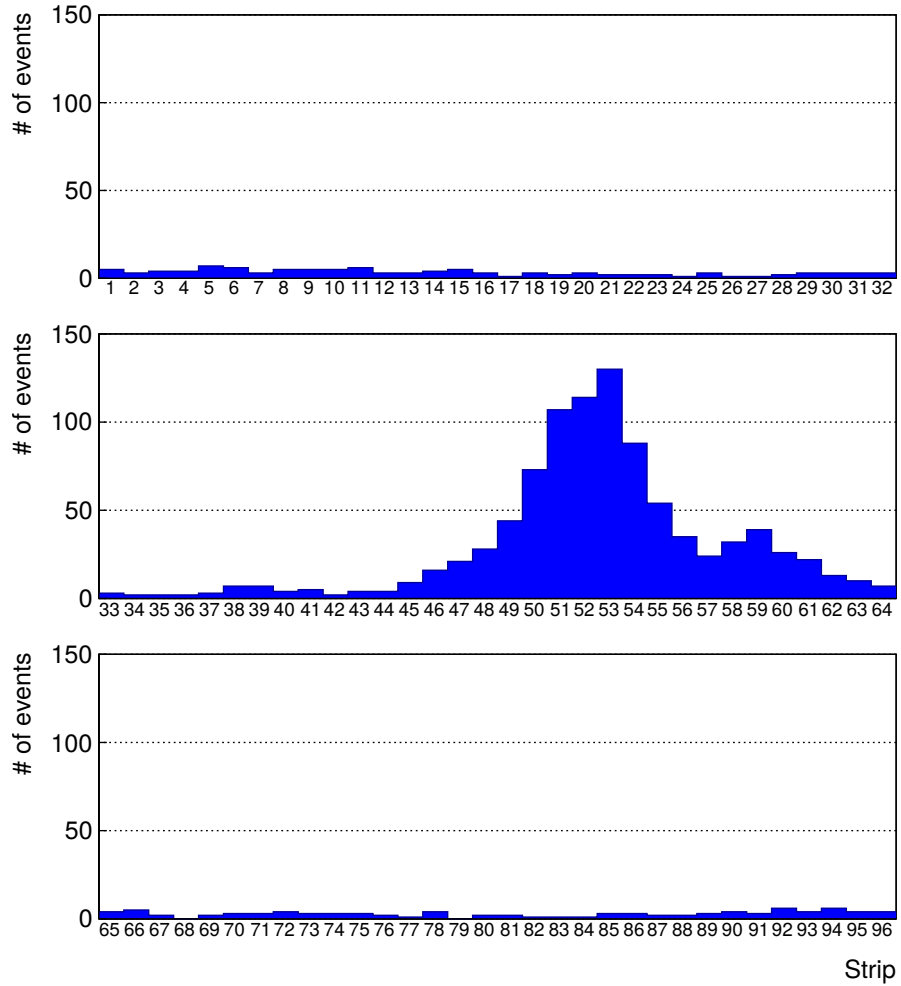


Figure 4.9: Description of the RPC setup. Dimensions are given in mm. A tent containing RPCs is placed at 1720 mm from the source container. The source is situated in the center of the container. RE-4-2-BARC-161 chamber is 160 mm inside the tent. This way, the distance between the source and the chambers plan is 2060 mm. Figure 4.9a provides a side view of the setup in the xz plane while Figure 4.9b shows a top view in the yz plane.



*Figure 4.10: RE-4-2-BARC-I61 chamber is inside the tent as described in Figure 4.9. In the top right, the two scintillators used as trigger can be seen. This trigger system has an inclination of 10° relative to horizontal and is placed above half-partition B2 of the RPCs. PMT electronics are shielded thanks to lead blocks placed in order to protect them without stopping photons from going through the scintillators and the chamber.*

1247 At the time of the tests, the beam not being operational anymore, a trigger composed of 2 plastic  
 1248 scintillators has been placed in front of the setup with an inclination of 10 deg with respect to the  
 1249 detector plane in order to look at cosmic muons. Using this particular trigger layout, shown on Fig-  
 1250 ure 4.10, leads to a cosmic muon hit distribution into the chamber similar to the one in Figure 4.11.  
 1251 Measured without gamma irradiation, two peaks can be seen on the profile of partition B, centered  
 1252 on strips 52 and 59. Section ?? will help us understand that these two peaks are due respectively to  
 1253 forward and backward coming cosmic particles where forward coming particles are first detected by  
 1254 the scintillators and then the RPC while the backward coming muons are first detected in the RPC.



*Figure 4.11: Hit distributions over all 3 partitions of RE-4-2-BARC-161 chamber is showed on these plots. Top, middle and bottom figures respectively correspond to partitions A, B, and C. These plots show that some events still occur in other half-partitions than B2, which corresponds to strips 49 to 64, in front of which the trigger is placed, contributing to the inefficiency of detection of cosmic muons. In the case of partitions A and C, the very low amount of data can be interpreted as noise. On the other hand, it is clear that a little portion of muons reach the half-partition B1, corresponding to strips 33 to 48.*

### 1255 4.3.2 Data Acquisition

### 1256 4.3.3 Geometrical acceptance of the setup layout to cosmic muons

1257 In order to profit from a constant gamma irradiation, the detectors inside of the GIF bunker need  
 1258 to be placed in a plane orthogonal to the beam line. The muon beam that used to be available was  
 1259 meant to test the performance of detectors under test. This beam not being active anymore, another  
 1260 solution to test detector performance had to be used. Thus, it has been decided to use cosmic muons  
 1261 detected through a telescope composed of two scintillators. Lead blocks were used as shielding to

protect the photomultipliers from gammas as can be seen from Figure 4.10.

An inclination has been given to the cosmic telescope to maximize the muon flux. A good compromise had to be found between good enough muon flux and narrow enough hit distribution to be sure to contain all the events into only one half partitions as required from the limited available readout hardware. Nevertheless, a consequence of the misplaced trigger, that can be seen as a loss of events in half-partition B1 in Figure 4.11, is an inefficiency. Nevertheless, the inefficiency of approximately 20 % highlighted in Figure 4.12 by comparing the performance of chamber BARC-161 in 904 and at GIF without irradiation seems too important to be explained only by the geometrical acceptance of the setup itself. Simulations have been conducted to show how the setup brings inefficiency.

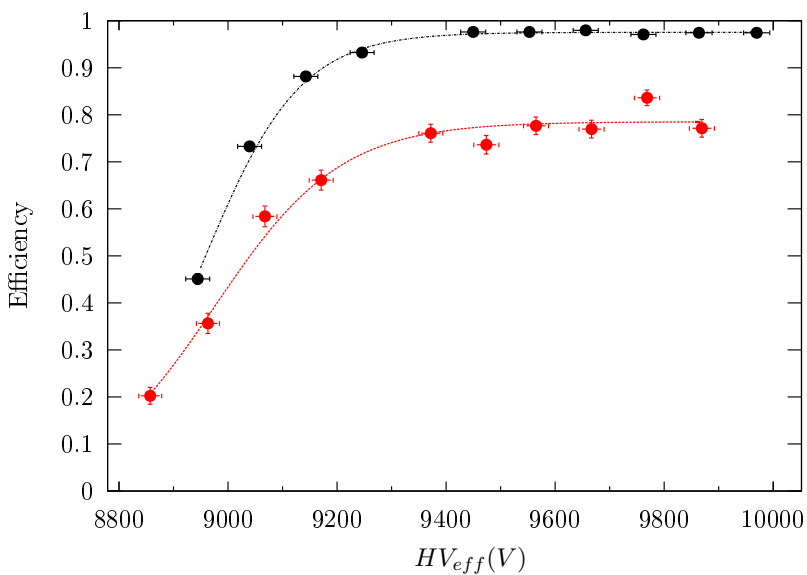
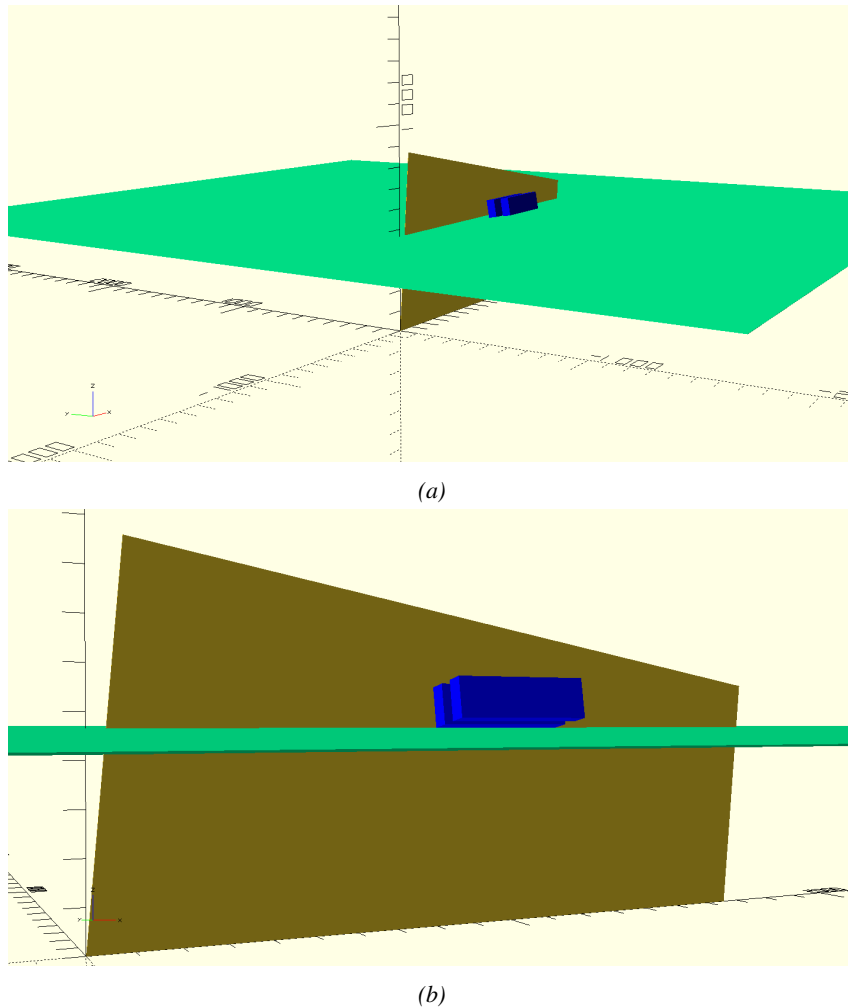


Figure 4.12: Results are derived from data taken on half-partition B2 only. On the 18<sup>th</sup> of June 2014, data has been taken on chamber RE-2-BARC-161 at building 904 (Prevessin Site) with cosmic muons providing us a reference efficiency plateau of  $(97.54 \pm 0.15)\%$  represented by a black curve. A similar measurement has been done at GIF on the 21<sup>st</sup> of July with the same chamber giving a plateau of  $(78.52 \pm 0.94)\%$  represented by a red curve.

#### 4.3.3.1 Description of the simulation layout

The layout of GIF setup has been reproduced and incorporated into a Monte Carlo (MC) simulation to study the influence of the disposition of the telescope on the final distribution measured by the RPC. A 3D view of the simulated layout is given into Figure 4.13. Muons are generated randomly in a horizontal plane located at a height corresponding to the lowest point of the PMTs. This way, the needed size of the plane in order to simulate events happening at very big azimuthal angles (i.e.  $\theta \approx \pi$ ) can be kept relatively small. The muon flux is designed to follow the usual  $\cos^2\theta$  distribution for cosmic particle. The goal of the simulation is to look at muons that pass through the muon telescope composed of the two scintillators and define their distribution onto the RPC plane. During the reconstruction, the RPC plane is then divided into its strips and each muon track is assigned to a strip.



*Figure 4.13: Representation of the layout used for the simulations of the test setup. The RPC is represented as a yellow trapezoid while the two scintillators as blue cuboids looking at the sky. A green plane corresponds to the muon generation plane within the simulation. Figure 4.9a shows a global view of the simulated setup. Figure 4.9b shows a zoomed view that allows to see the 2 scintillators as well as the full RPC plane.*

1283 In order to further refine the quality of the simulation and understand deeper the results the  
 1284 dependance of the distribution has been studied for a range of telescope inclinations. Moreover,  
 1285 the threshold applied on the PMT signals has been included into the simulation in the form of a  
 1286 cut. In the approximation of uniform scintillators, it has been considered that the threshold can be  
 1287 understood as the minimum distance particles need to travel through the scintillating material to give  
 1288 a strong enough signal. Particles that travel a distance smaller than the set "threshold" are thus not  
 1289 detected by the telescope and cannot trigger the data taking. Finally, the FEE threshold also has  
 1290 been considered in a similar way. The mean momentum of horizontal cosmic rays is higher than  
 1291 those of vertical ones but the stopping power of matter for momenta ranging from 1 GeV to 1 TeV  
 1292 stays comparable. It is then possible to assume that the mean number of primary  $e^-/ion$  pairs per  
 1293 unit length will stay similar and thus, depending on the applied discriminator threshold, muons with

1294 the shortest path through the gas volume will deposit less charge and induce a smaller signal on the  
 1295 pick-up strips that could eventually not be detected. These two thresholds also restrain the overall  
 1296 geometrical acceptance of the system.

1297 **4.3.3.2 Simulation procedure**

1298 The simulation software has been designed using C++ and the output data is saved into ROOT  
 1299 histograms. Simulations start for a threshold  $T_{scint}$  varying in a range from 0 to 45 mm in steps  
 1300 of 5 mm, where  $T_{scint} = 0$  mm corresponds to the case where there isn't any threshold apply on  
 1301 the input signal while  $T_{scint} = 45$  mm, which is the scintillator thickness, is the case where muons  
 1302 cannot arrive orthogonally onto the scintillator surface. For a given  $T_{scint}$ , a set of RPC thresholds  
 1303 are considered. The RPC threshold,  $T_{RPC}$  varies from 2 mm, the thickness of the gas volume, to  
 1304 3 mm in steps of 0.25 mm. For each  $(T_{scint}; T_{RPC})$  pair,  $N_\mu = 10^8$  muons are randomly generated  
 1305 inside the muon plane described in the previous paragraph with an azimuthal angle  $\theta$  chosen to follow  
 1306 a  $\cos^2\theta$  distribution.

1307 Planes are associated to each surface of the scintillators. Knowing muon position into the muon  
 1308 plane and its direction allows us, by assuming that muons travel in a straight line, to compute the  
 1309 intersection of the muon track with these planes. Applying conditions to the limits of the surfaces  
 1310 of the scintillator faces then gives us an answer to whether or not the muon passed through the  
 1311 scintillators. In the case the muon has indeed passed through the telescope, the path through each  
 1312 scintillator is computed and muons whose path was shorter than  $T_{scint}$  are rejected and are thus  
 1313 considered as having not interacted with the setup.

1314 On the contrary, if the muon is labeled as good, its position within the RPC plane is computed  
 1315 and the corresponding strip, determined by geometrical tests in the case the distance through the  
 1316 gas volume was enough not to be rejected because of  $T_{RPC}$ , gets a hit and several histograms  
 1317 are filled in order to keep track of the generation point on the muon plane, the intersection points  
 1318 of the reconstructed muons within the telescope, or on the RPC plane, the path traveled through  
 1319 each individual scintillator or the gas volume, as well as other histograms. Moreover, muons fill  
 1320 different histograms whether they are forward or backward coming muons. They are discriminated  
 1321 according to their direction components. When a muon is generated, an  $(x, y, z)$  position is assigned  
 1322 into the muon plane as well as a  $(\theta; \phi)$  pair that gives us the direction it's coming from. This way,  
 1323 muons satisfying the condition  $0 \leq \phi < \pi$  are designated as backward coming muons while muons  
 1324 satisfying  $\pi \leq \phi < 2\pi$  as forward coming muons.

1325 This simulation is then repeated for different telescope inclinations ranging in between 4 and  $20^\circ$   
 1326 and varying in steps of  $2^\circ$ . Due to this inclination and to the vertical position of the detector under  
 1327 test, the muon distribution reconstructed in the detector plane is asymmetrical. The choice as been  
 1328 made to chose a skew distribution formula to fit the data built as the multiplication of gaussian and  
 1329 sigmoidal curves together. A typical gaussian formula is given as 4.1 and has three free parameters  
 1330 as  $A_g$ , its amplitude,  $\bar{x}$ , its mean value and  $\sigma$ , its root mean square. Sigmoidal curves as given by  
 1331 formula 4.2 are functions converging to 0 and  $A_s$  as  $x$  diverges. The inflection point is given as  $x_i$   
 1332 and  $\lambda$  is proportional to the slope at  $x = x_i$ . In the limit where  $\lambda \rightarrow \infty$ , the sigmoid becomes a  
 1333 step function.

$$g(x) = A_g e^{-\frac{(x-\bar{x})^2}{2\sigma^2}} \quad (4.1)$$

$$s(x) = \frac{A_s}{1 + e^{-\lambda(x-x_i)}} \quad (4.2)$$

Finally, a possible representation of a skew distribution is given by formula 4.3 and is the product of 4.1 and 4.2. Naturally, here  $A_{sk} = A_g \times A_s$  and represents the theoretical maximum in the limit where the skew tends to a gaussian function.

$$sk(x) = g(x) \times s(x) = A_{sk} \frac{e^{\frac{-(x-\bar{x})^2}{2\sigma^2}}}{1 + e^{-\lambda(x-x_i)}} \quad (4.3)$$

### 4.3.3.3 Results

#### Influence of $T_{scint}$ on the muon distribution

#### Influence of $T_{RPC}$ on the muon distribution

#### Influence of the telescope inclination on the muon distribution

#### Comparison to data taken at GIF without irradiation

### 4.3.4 Photon flux at GIF

#### 4.3.4.1 Expectations from simulations

In order to understand and evaluate the  $\gamma$  flux in the GIF area, simulations had been conducted in 1999 and published by S. Agosteo et al [55]. Table 4.1 presented in this article gives us the  $\gamma$  flux for different distances  $D$  to the source. This simulation was done using GEANT and a Monte Carlo N-Particle (MCNP) transport code, and the flux  $F$  is given in number of  $\gamma$  per unit area and unit time along with the estimated error from these packages expressed in %.

Nominal ABS	Photon flux $F$ [ $s^{-1}cm^{-2}$ ]			
	at $D = 50$ cm	at $D = 155$ cm	at $D = 300$ cm	at $D = 400$ cm
1	$0.12 \cdot 10^8 \pm 0.2\%$	$0.14 \cdot 10^7 \pm 0.5\%$	$0.45 \cdot 10^6 \pm 0.5\%$	$0.28 \cdot 10^6 \pm 0.5\%$
2	$0.68 \cdot 10^7 \pm 0.3\%$	$0.80 \cdot 10^6 \pm 0.8\%$	$0.25 \cdot 10^6 \pm 0.8\%$	$0.16 \cdot 10^6 \pm 0.6\%$
5	$0.31 \cdot 10^7 \pm 0.4\%$	$0.36 \cdot 10^6 \pm 1.2\%$	$0.11 \cdot 10^6 \pm 1.2\%$	$0.70 \cdot 10^5 \pm 0.9\%$

Table 4.1: Total photon flux ( $E\gamma \leq 662$  keV) with statistical error predicted considering a  $^{137}Cs$  activity of 740 GBq at different values of the distance  $D$  to the source along the  $x$ -axis of irradiation field [55].

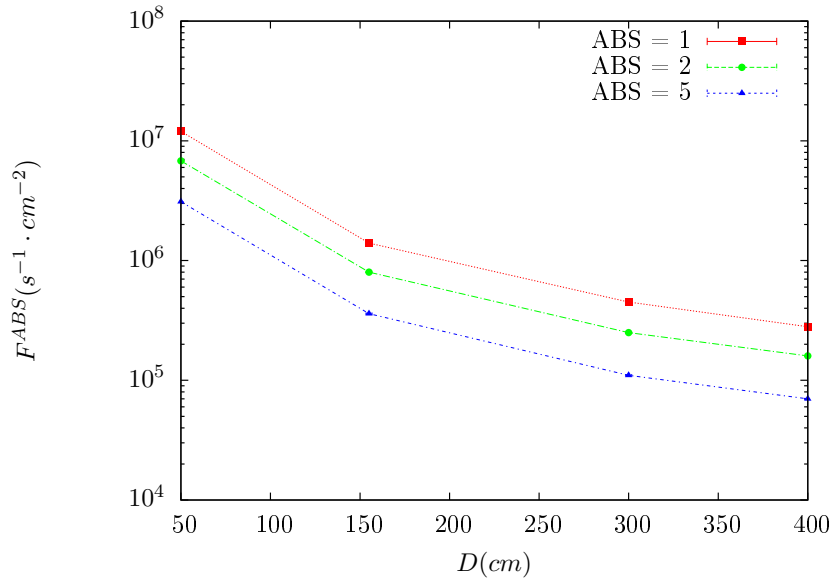


Figure 4.14:  $\gamma$  flux  $F(D)$  is plot using values from table 4.1. As expected, the plot shows similar attenuation behaviours with increasing distance for each absorption factors.

The simulation doesn't directly provides us with an estimated flux at the level of our RPC. First of all, it is needed to extract the value of the flux from the available data contained in the original paper and then to estimate the flux in 2014 at the time the experimentation took place. Figure 4.14 that contains the data from Table 4.1. In the case of a pointlike source emitting isotropic and homogeneous gamma radiations, the gamma flux  $F$  at a distance  $D$  to the source with respect to a reference point situated at  $D_0$  where a known flux  $F_0$  is measured will be expressed like in Equation 4.4, assuming that the flux decreases as  $1/D^2$ , where  $c$  is a fitting factor.

$$F^{ABS} = F_0^{ABS} \times \left( \frac{cD_0}{D} \right)^2 \quad (4.4)$$

By rewriting Equation 4.4, it comes that :

$$c = \frac{D}{D_0} \sqrt{\frac{F^{ABS}}{F_0^{ABS}}} \quad (4.5)$$

$$\Delta c = \frac{c}{2} \left( \frac{\Delta F^{ABS}}{F^{ABS}} + \frac{\Delta F_0^{ABS}}{F_0^{ABS}} \right) \quad (4.6)$$

Finally, using Equation 4.5 and the data in Table 4.1 with  $D_0 = 50$  cm as reference point, we can build Table 4.2. It is interesting to note that  $c$  for each value of  $D$  doesn't depend on the absorption factor.

Nominal ABS	Correction factor $c$		
	at $D = 155$ cm	at $D = 300$ cm	at $D = 400$ cm
1	$1.059 \pm 0.70\%$	$1.162 \pm 0.70\%$	$1.222 \pm 0.70\%$
2	$1.063 \pm 1.10\%$	$1.150 \pm 1.10\%$	$1.227 \pm 0.90\%$
5	$1.056 \pm 1.60\%$	$1.130 \pm 1.60\%$	$1.202 \pm 1.30\%$

Table 4.2: Correction factor  $c$  is computed thanks to formulae 4.5 taking as reference  $D_0 = 50$  cm and the associated flux  $F_0^{ABS}$  for each absorption factor available in table 4.1.

1360 For the range of  $D/D_0$  values available, it is possible to use a simple linear fit to get the evolution  
 1361 of  $c$ . The linear fit will then use only 2 free parameters,  $a$  and  $b$ , as written in Equation 4.7. This gives  
 1362 us the results showed in Figure 4.15. Figure 4.15b confirms that using only a linear fit to extract  $c$  is  
 1363 enough as the evolution of the rate that can be obtained superimposes well on the simulation points.

$$c \left( \frac{D}{D_0} \right) = a \frac{D}{D_0} + b \quad (4.7)$$

$$F^{ABS} = F_0^{ABS} \left( a + \frac{bD_0}{D} \right)^2 \quad (4.8)$$

$$\Delta F^{ABS} = F^{ABS} \left[ \frac{\Delta F_0^{ABS}}{F_0^{ABS}} + 2 \frac{\Delta a + \Delta b \frac{D_0}{D}}{a + \frac{bD_0}{D}} \right] \quad (4.9)$$

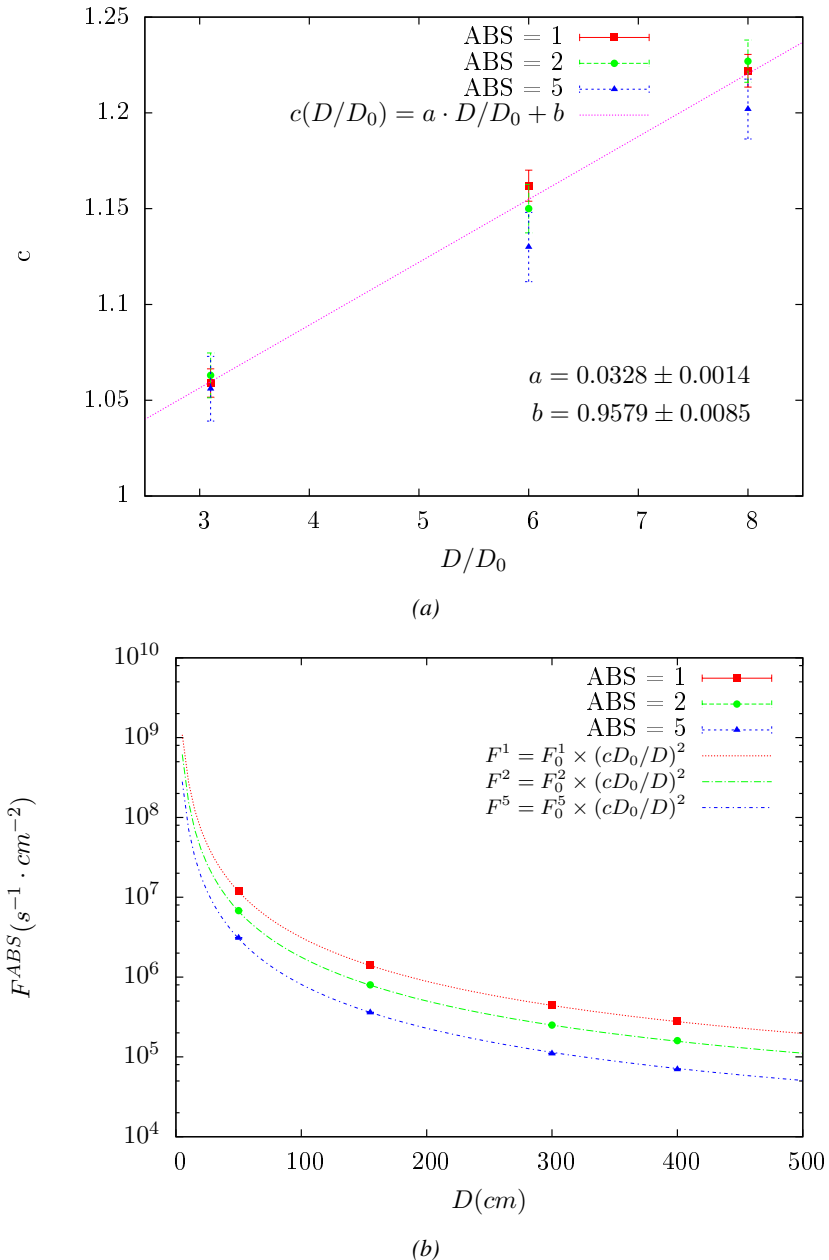


Figure 4.15: Figure 4.15a shows the linear approximation fit done via formulae 4.7 on data from table 4.2. Figure 4.15b shows a comparison of this model with the simulated flux using  $a$  and  $b$  given in figure 4.15a in formulae 4.4 and the reference value  $D_0 = 50\text{cm}$  and the associated flux for each absorption factor  $F_0^{ABS}$  from table 4.1

In the case of the 2014 GIF tests, the RPC plane is located at a distance  $D = 206\text{ cm}$  to the source. Moreover, to estimate the strength of the flux in 2014, it is necessary to consider the nuclear decay through time associated to the Cesium source whose half-life is well known ( $t_{1/2} = (30.05 \pm 0.08)\text{ y}$ ). The very first source activity measurement has been done on the 5<sup>th</sup> of March 1997 while the GIF

1368 tests where done in between the 20<sup>th</sup> and the 31<sup>st</sup> of August 2014, i.e. at a time  $t = (17.47 \pm 0.02)$  y  
 1369 resulting in an attenuation of the activity from 740 GBq in 1997 to 494 GBq in 2014. All the needed  
 1370 information to extrapolate the flux through our detector in 2014 has now been assembled, leading  
 1371 to the Table 4.3. It is interesting to note that for a common RPC sensitivity to  $\gamma$  of  $2 \cdot 10^{-3}$ , the  
 1372 order of magnitude of the estimated hit rate per unit area is of the order of the kHz for the fully  
 1373 opened source. Moreover, taking profit of the two working absorbers, it will be possible to scan  
 1374 background rates at 0 Hz,  $\sim 300$  Hz as well as  $\sim 600$  Hz. Without source, a good estimate of the  
 1375 intrinsic performance will be available. Then at 300 Hz, the goal will be to show that the detectors  
 1376 fulfill the performance certification of CMS RPCs. Then a first idea of the performance of the  
 1377 detectors at higher background will be provided with absorption factors 2 ( $\sim 600$  Hz) and 1 (no  
 1378 absorption). *[Here I will also put a reference to the plot showing the estimated background rate at  
 1379 the level of RE3/1 in the case of HL-LHC but this one being in another chapter, I will do it later.]*

Nominal ABS	Photon flux $F$ [ $s^{-1}cm^{-2}$ ]			Hit rate/unit area [ $Hz cm^{-2}$ ] at $D^{2014} = 206$ cm
	at $D_0^{1997} = 50$ cm	at $D^{1997} = 206$ cm	at $D^{2014} = 206$ cm	
1	$0.12 \cdot 10^8 \pm 0.2\%$	$0.84 \cdot 10^6 \pm 0.3\%$	$0.56 \cdot 10^6 \pm 0.3\%$	$1129 \pm 32$
2	$0.68 \cdot 10^7 \pm 0.3\%$	$0.48 \cdot 10^6 \pm 0.3\%$	$0.32 \cdot 10^6 \pm 0.3\%$	$640 \pm 19$
5	$0.31 \cdot 10^7 \pm 0.4\%$	$0.22 \cdot 10^6 \pm 0.3\%$	$0.15 \cdot 10^6 \pm 0.3\%$	$292 \pm 9$

Table 4.3: The data at  $D_0$  in 1997 is taken from [55]. In a second step, using Equations 4.8 and 4.9, the flux at  $D$  can be estimated in 1997. Then, taking into account the attenuation of the source activity, the flux at  $D$  can be estimated at the time of the tests in GIF in 2014. Finally, assuming a sensitivity of the RPC to  $\gamma$   $s = 2 \cdot 10^{-3}$ , an estimation of the hit rate per unit area is obtained.

1380 **4.3.4.2 Dose measurements**

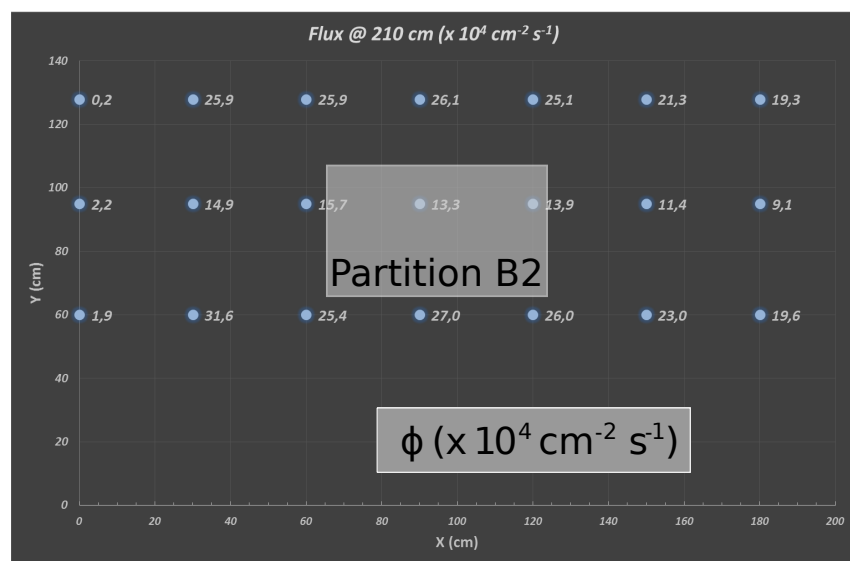


Figure 4.16: Dose measurements has been done in a plane corresponding to the tents front side. This plan is 1900 mm away from the source. As explained in the first chapter, a lens-shaped lead filter provides a uniform photon flux in the vertical plan orthogonal to the beam direction. If the second line of measured fluxes is not taken into account because of lower values due to experimental equipments in the way between the source and the tent, the uniformity of the flux is well showed by the results.

<sup>1381</sup> **4.3.5 Results and discussions**

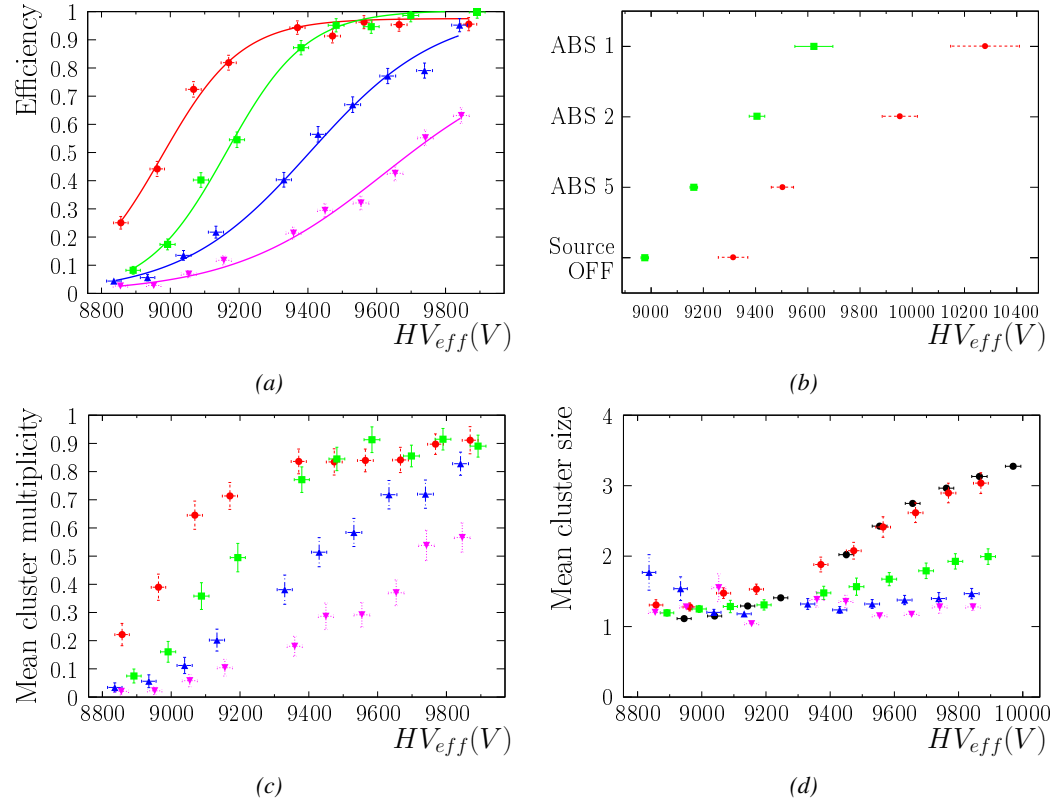


Figure 4.17

## 1382 4.4 Longevity tests at GIF++

1383 Longevity studies imply a monitoring of the performance of the detectors probed using a high inten-  
1384 sity muon beam in a irradiated environment by periodically measuring their rate capability, the dark  
1385 current running through them and the bulk resistivity of the Bakelite composing their electrodes.  
1386 GIF++, with its very intense  $^{137}\text{Cs}$  source, provides the perfect environment to perform such kind  
1387 of tests. Assuming a maximum acceleration factor of 3, it is expected to accumulate the equivalent  
1388 charge in 1.7 years.

1389 As the maximum background is found in the endcap, the choice naturally was made to focus the  
1390 GIF++ longevity studies on endcap chambers. Most of the RPC system was installed in 2007. Nev-  
1391 ertheless, the large chambers in the fourth endcap (RE4/2 and RE4/3) have been installed during  
1392 LS1 in 2014. The Bakelite of these two different productions having different properties, four spare  
1393 chambers of the present system were selected, two RE2,3/2 spares and two RE4/2 spares. Having  
1394 two chambers of each type allows to always keep one of them non irradiated as reference, the per-  
1395 formance evolution of the irradiated chamber being then compared through time to the performance  
1396 of the non irradiated one.

1397 The performance of the detectors under different level of irradiation is measured periodically dur-  
1398 ing dedicated test beam periods using the H4 muon beam. In between these test beam periods, the  
1399 two RE2,3/2 and RE4/2 chambers selected for this study are irradiated by the  $^{137}\text{Cs}$  source in order  
1400 to accumulate charge and the gamma background is monitored, as well as the currents. The two  
1401 remaining chambers are kept non-irradiated as reference detectors. Due to the limited gas flow in  
1402 GIF++, the RE4 chamber remained non-irradiated until end of November 2016 where a new mass  
1403 flow controller has been installed allowing for bigger volumes of gas to flow in the system.

1404 Figures 4.18 and 4.19 give us for different test beam periods, and thus for increasing integrated  
1405 charge through time, a comparison of the maximum efficiency, obtained using a sigmoid-like func-  
1406 tion, and of the working point of both irradiated and non irradiated chambers [**SIGMOID2005**]. No  
1407 aging is yet to see from this data, the shifts in  $\gamma$  rate per unit area in between irradiated and non  
1408 irradiated detectors and RE2 and RE4 types being easily explained by a difference of sensitivity due  
1409 to the various Bakelite resistivities of the HPL electrodes used for the electrode production.

1410 Collecting performance data at each test beam period allows us to extrapolate the maximum effi-  
1411 ciency for a background hit rate of  $300\text{ Hz}/\text{cm}^2$  corresponding to the expected HL-LHC conditions.  
1412 Aging effects could emerge from a loss of efficiency with increasing integrated charge over time,  
1413 thus Figure 4.20 helps us understand such degradation of the performance of irradiated detectors in  
1414 comparison with non irradiated ones. The final answer for an eventual loss of efficiency is given in  
1415 Figure 4.21 by comparing for both irradiated and non irradiated detectors the efficiency sigmoids  
1416 before and after the longevity study. Moreover, to complete the performance information, the Bake-  
1417 lite resistivity is regularly measured thanks to  $Ag$  scans (Figure 4.22) and the noise rate is monitored  
1418 weekly during irradiation periods (Figure 4.23). At the end of 2016, no signs of aging were observed  
1419 and further investigation is needed to get closer to the final integrated charge requirements proposed  
1420 for the longevity study of the present CMS RPC sub-system.

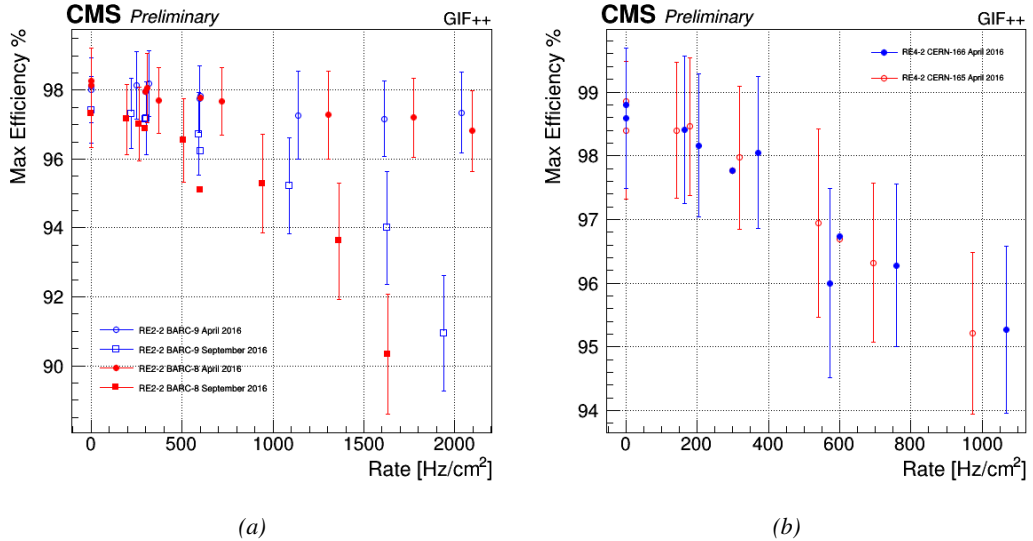


Figure 4.18: Evolution of the maximum efficiency for RE2 (4.18a) and RE4 (4.18b) chambers with increasing extrapolated  $\gamma$  rate per unit area at working point. Both irradiated (blue) and non irradiated (red) chambers are shown.

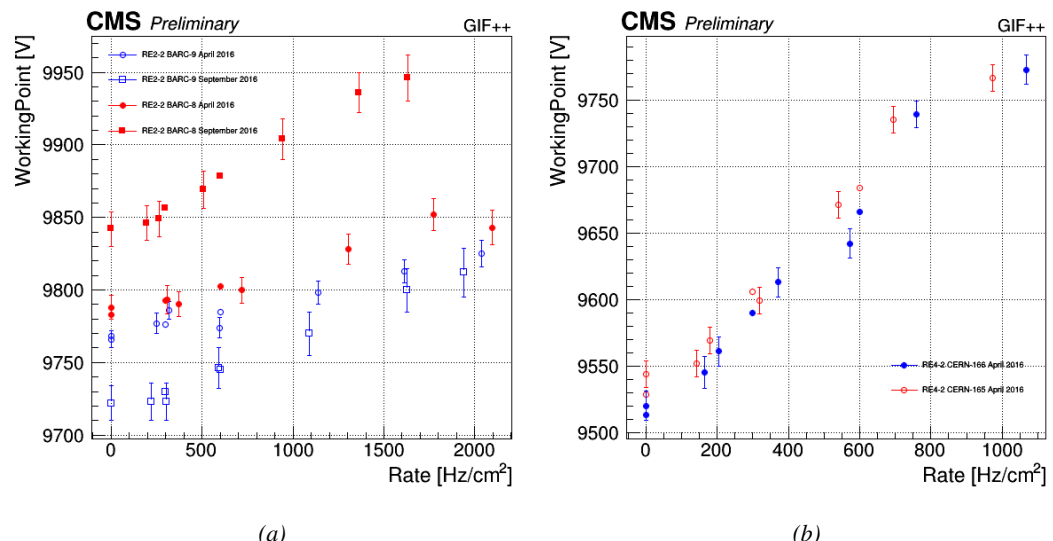
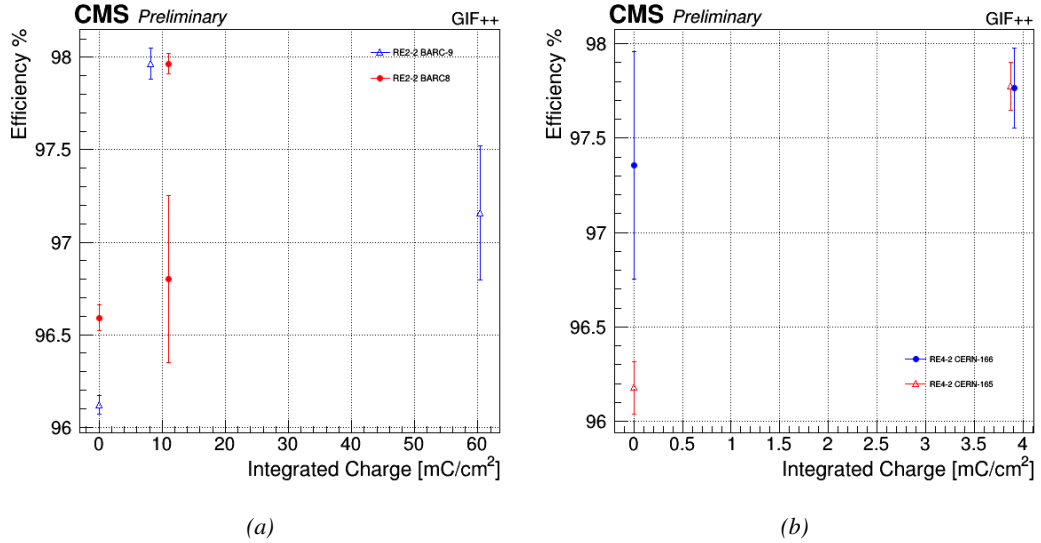
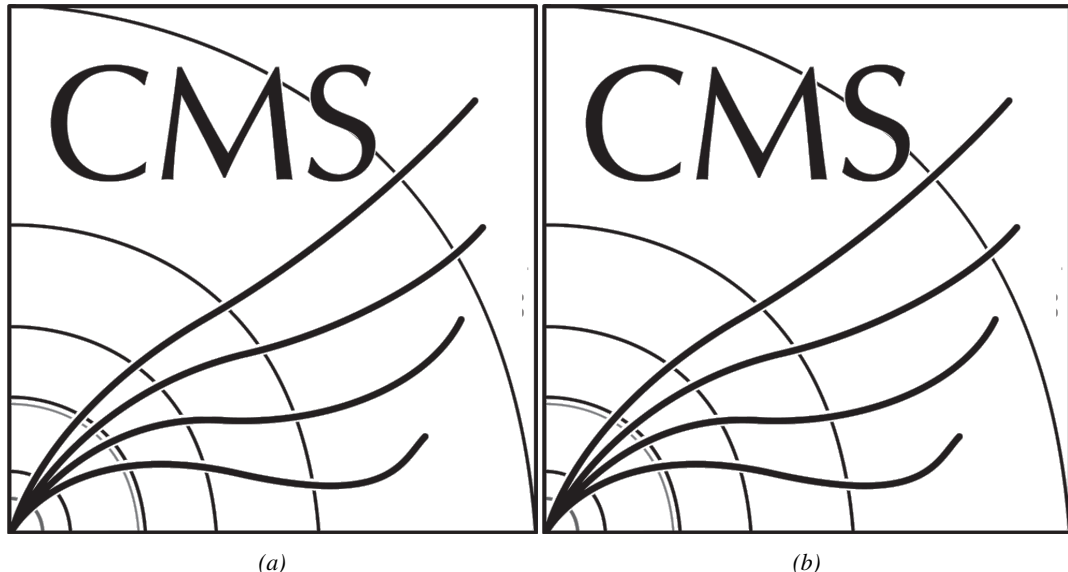


Figure 4.19: Evolution of the working point for RE2 (4.19a) and RE4 (4.19b) with increasing extrapolated  $\gamma$  rate per unit area at working point. Both irradiated (blue) and non irradiated (red) chambers are shown.



*Figure 4.20: Evolution of the maximum efficiency at HL-LHC conditions, i.e. a background hit rate per unit area of 300 Hz/cm<sup>2</sup>, with increasing integrated charge for RE2 (4.20a) and RE4 (4.20b) detectors. Both irradiated (blue) and non irradiated (red) chambers are shown. The integrated charge for non irradiated detectors is recorded during test beam periods and stays small with respect to the charge accumulated in irradiated chambers.*



*Figure 4.21: Comparison of the efficiency sigmoid before (triangles) and after (circles) irradiation for RE2 (4.21a) and RE4 (4.21b) detectors. Both irradiated (blue) and non irradiated (red) chambers are shown.*

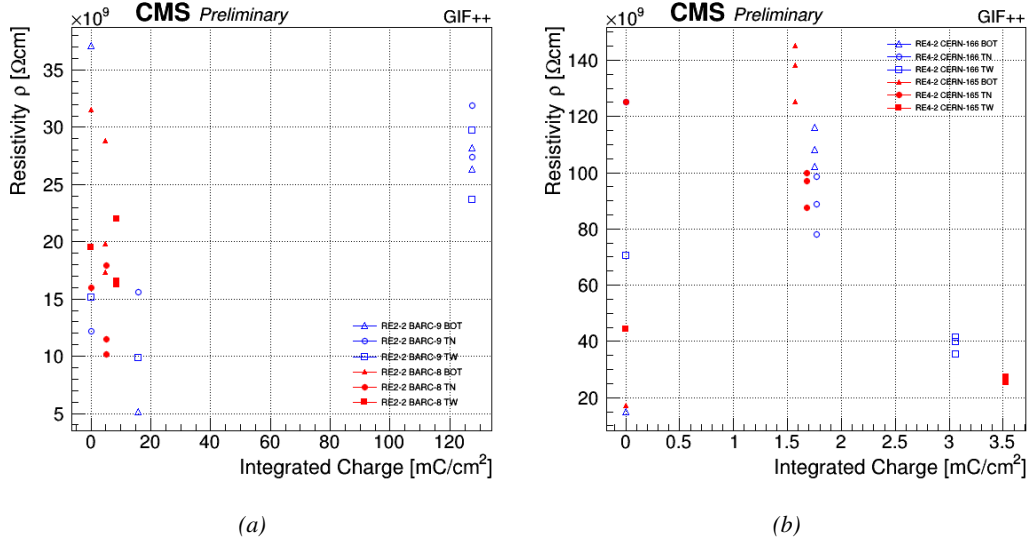


Figure 4.22: Evolution of the Bakelite resistivity for RE2 (4.22a) and RE4 (4.22b) detectors. Both irradiated (blue) and non-irradiated (red) chambers are shown.

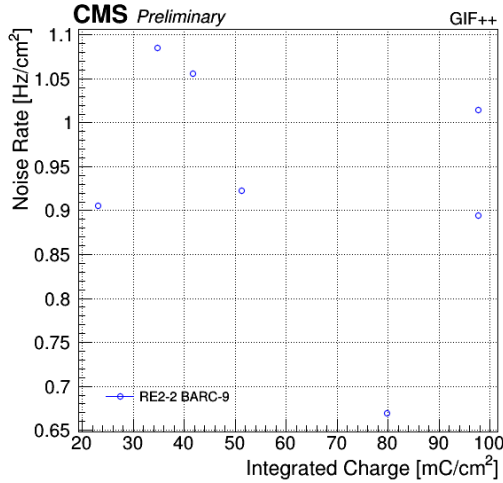


Figure 4.23: Evolution of the noise rate per unit area for the irradiated chamber RE2-2-BARC-9 only.

#### 4.4.1 Description of the Data Acquisition

For the longevity studies, four spare chambers of the present system are used. Two spare RPCs of the RE2,3 stations as well as two spare RPCs from the new RE4 stations have been mounted in a Trolley. Six RE4 gaps are also placed in the trolley. The trolley is placed inside the GIFT++ in the upstream region of the bunker, taking the cesium source as a reference. The trolley is oriented for the detection surface of the chambers to be orthogonal to the beam line. The system can be moved along the orthogonal plane in order to have the beam in all  $\eta$ -partitions. For the aging the trolley is

1429 moved outside the beam line and is placed in a distance of 5.2 m to the source, which irradiates the  
 1430 bunker using an attenuation filter of 2.2 which corresponds to a fluence of  $10^7 \text{ gamma/cm}^2$ .

1431 During GIF++ operation, the data collected can be divided into different categories as several  
 1432 parameters are monitored in addition to the usual RPC performance data. On one hand, to know  
 1433 the performance of a chamber, it is need to measure its efficiency and to know the background  
 1434 conditions in which it is operated. To do this, the hit signals from the chamber are recorded and  
 1435 stored in a ROOT file via a Data Acquisition (DAQ) software. On the other hand, it is also very  
 1436 important to monitor parameters such as environmental pressure and temperature, gas temperature  
 1437 and humidity, RPC HV, LV, and currents, or even source and beam status. This is done through the  
 1438 GIF++ web Detector Control Software (DCS) that stores this information in a database.

1439 Two different types of tests are conducted on RPCs via the DAQ. Indeed, the performance of the  
 1440 detectors is measured periodically during dedicated test beam periods using the H4 muon beam. In  
 1441 between these test beam periods, when the beam is not available, the chambers are irradiated by the  
 1442  $^{137}\text{Cs}$  in order to accumulate deposited charge and the gamma background is measured.

1443 RPCs under test are connected through LVDS cables to V1190A Time-to-Digital Converter  
 1444 (TDC) modules manufactured by CAEN. These modules, located in the rack area outside of the  
 1445 bunker, get the logic signals sent by the chambers and save them into their buffers. Due to the  
 1446 limited size of the buffers, the collected data is regularly erased and replaced. A trigger signal is  
 1447 needed for the TDC modules to send the useful data to the DAQ computer via a V1718 CAEN USB  
 1448 communication module.

1449 In the case of performance test, the trigger signal used for data acquisition is generated by the  
 1450 coincidence of three scintillators. A first one is placed upstream outside of the bunker, a second one  
 1451 is placed downstream outside of the bunker, while a third one is placed in front of the trolley, close by  
 1452 the chambers. Every time a trigger is sent to the TDCs, i.e. every time a muon is detected, knowing  
 1453 the time delay in between the trigger and the RPC signals, signals located in the right time window  
 1454 are extracted from the buffers and saved for later analysis. Signals are taken in a time window of  
 1455 400 ns centered on the muon peak (here we could show a time spectrum). On the other hand, in the  
 1456 case of background rate measurement, the trigger signal needs to be "random" not to measure muons  
 1457 but to look at gamma background. A trigger pulse is continuously generated at a rate of 300 Hz using  
 1458 a dual timer. To integrate an as great as possible time, all signals contained within a time window of  
 1459 10us prior to the random trigger signal are extracted form the buffers and saved for further analysis  
 1460 (here another time spectrum to illustrate could be useful, maybe even place both spectrum together  
 1461 as a single Figure).

1462 The signals sent to the TDCs correspond to hit collections in the RPCs. When a particle hits  
 1463 a RPC, it induce a signal in the pickup strips of the RPC readout. If this signal is higher than the  
 1464 detection threshold, a LVDS signal is sent to the TDCs. The data is then organised into 4 branches  
 1465 keeping track of the event number, the hit multiplicity for the whole setup, and the time and channel  
 1466 profile of the hits in the TDCs.

#### 1467 4.4.2 RPC current, environmental and operation parameter monitoring

1468 In order to take into account the variation of pressure and temperature between different data taking  
 1469 periods the applied voltage is corrected following the relationship :

$$1467 \quad HV_{eff} = HV_{app} \times \left( 0.2 + 0.8 \cdot \frac{P_0}{P} \times \frac{T}{T_0} \right) \quad (4.10)$$

<sup>1470</sup> where  $T_0$  (=293 K) and  $P_0$  (=990 mbar) are the reference values.

#### <sup>1471</sup> **4.4.3 Measurement procedure**

<sup>1472</sup> Insert a short description of the online tools (DAQ, DCS, DQM).

<sup>1473</sup> Insert a short description of the offline tools : tracking and efficiency algorithm.

<sup>1474</sup> Identify long term aging effects we are monitoring the rates per strip.

#### <sup>1475</sup> **4.4.4 Longevity studies results**



# 5

1476

1477

## Investigation on high rate RPCs

1478 **5.1 Rate limitations and ageing of RPCs**

1479 **5.1.1 Low resistivity electrodes**

1480 **5.1.2 Low noise front-end electronics**

1481 **5.2 Construction of prototypes**

1482 **5.3 Results and discussions**



# 6

## Conclusions and outlooks

1483

1484

1485 **6.1 Conclusions**

1486 **6.2 Outlooks**



# A

1487

1488

## A data acquisition software for CAEN VME TDCs

1489

1490 Certifying detectors in the perspective of HL-LHC required to develop tools for the GIF++ expe-  
1491 riment. Among them was the C++ Data Acquisition (DAQ) software that allows to make the com-  
1492 munications in between a computer and TDC modules in order to retrieve the RPC data [57]. In this  
1493 appendix, details about this software, as of how the software was written, how it functions and how  
1494 it can be exported to another similar setup, will be given.

### 1495 A.1 GIF++ DAQ file tree

1496 GIF++ DAQ source code is fully available on github at [https://github.com/afagot/GIF\\_](https://github.com/afagot/GIF_DAQ)  
1497 DAQ. The software requires 3 non-optional dependencies:

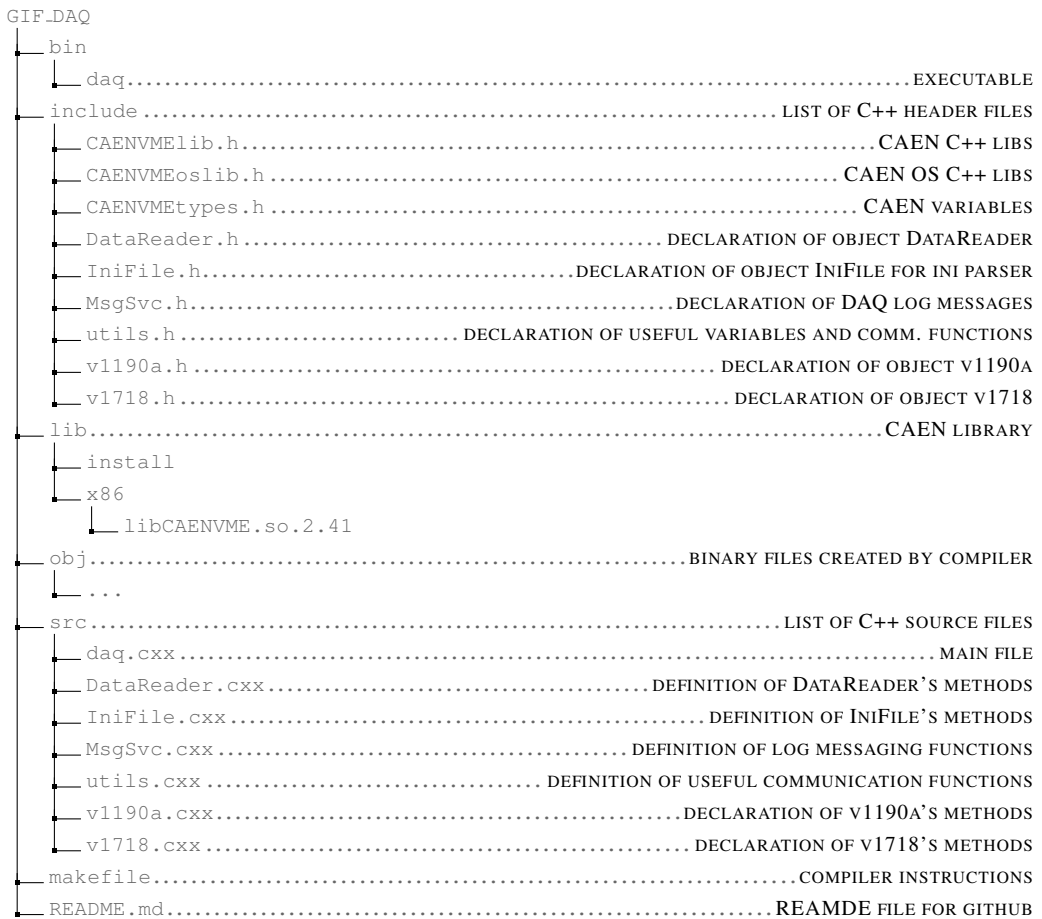
- 1498 • CAEN USB Driver, to mount the VME hardware,  
1499 • CAEN VME Library, to communicate with the VME hardware, and  
1500 • ROOT, to organize the collected data into a TTree.

1501 The CAEN VME library will not be packaged by distributions and will need to be installed man-  
1502 ually. To compile the GIF++ DAQ project via a terminal, from the DAQ folder use the command:

1503  
1504 make

1505 The source code tree is provided below along with comments to give an overview of the files' con-  
1506 tent. The different objects created for this project (`v1718`, `v1190a`, `IniFile` & `DataReader`) will be  
1507 described in details in the following sections.

1508



## 1509 A.2 Usage of the DAQ

1510 GIF++ DAQ, as used in GIF++, is not a standalone software. Indeed, the system being more complexe,  
 1511 the DAQ only is a sub-layer of the software architecture developped to control and monitor  
 1512 the RPCs that are placed into the bunker for performance study in an irradiated environment. The top  
 1513 layer of GIF++ is a Web Detector Control System (webDCS) application. The DAQ is only called  
 1514 by the webDCS when data needs to be acquired. The webDCS operates the DAQ through command  
 1515 line. To start the DAQ, the webDCS calls:

1516  
 1517   bin/daq /path/to/the/log/file/in/the/output/data/folder

1518 where /path/to/the/log/file/in/the/output/data/folder is the only argument required. This  
 1519 log file is important for the webDCS as this file contains all the content of the communication of the  
 1520 webDCS and the different systems monitored by the webDCS. Its content is constantly displayed  
 1521 during data taking for the users to be able to follow the operations. The communication messages  
 1522 are normally sent to the webDCS log file via the functions declared in file MsgSvc.h, typically  
 1523 MSG\_INFO(string message).

1524

### A.3 Description of the readout setup

1526 The CMS RPC setup at GIF++ counts 5 V1190A Time-to-Digital Converter (TDC) manufactured  
 1527 by CAEN [58]. V1190A are VME units accepting 128 independent Multi-Hit/Multi-Event TDC  
 1528 channels whose signals are treated by 4 100 ps high performance TDC chips developed by CERN  
 1529 / ECP-MIC Division. The communication between the computer and the TDCs to transfer data is  
 1530 done via a V1718 VME master module also manufactured by CAEN and operated from a USB  
 1531 port [59]. These VME modules are all hosted into a 6U VME 6021 powered crate manufactured by  
 1532 W-Ie-Ne-R than can accommodate up to 21 VME bus cards [60]. These 3 components of the DAQ  
 1533 setup are shown in Figure A.1.

1534

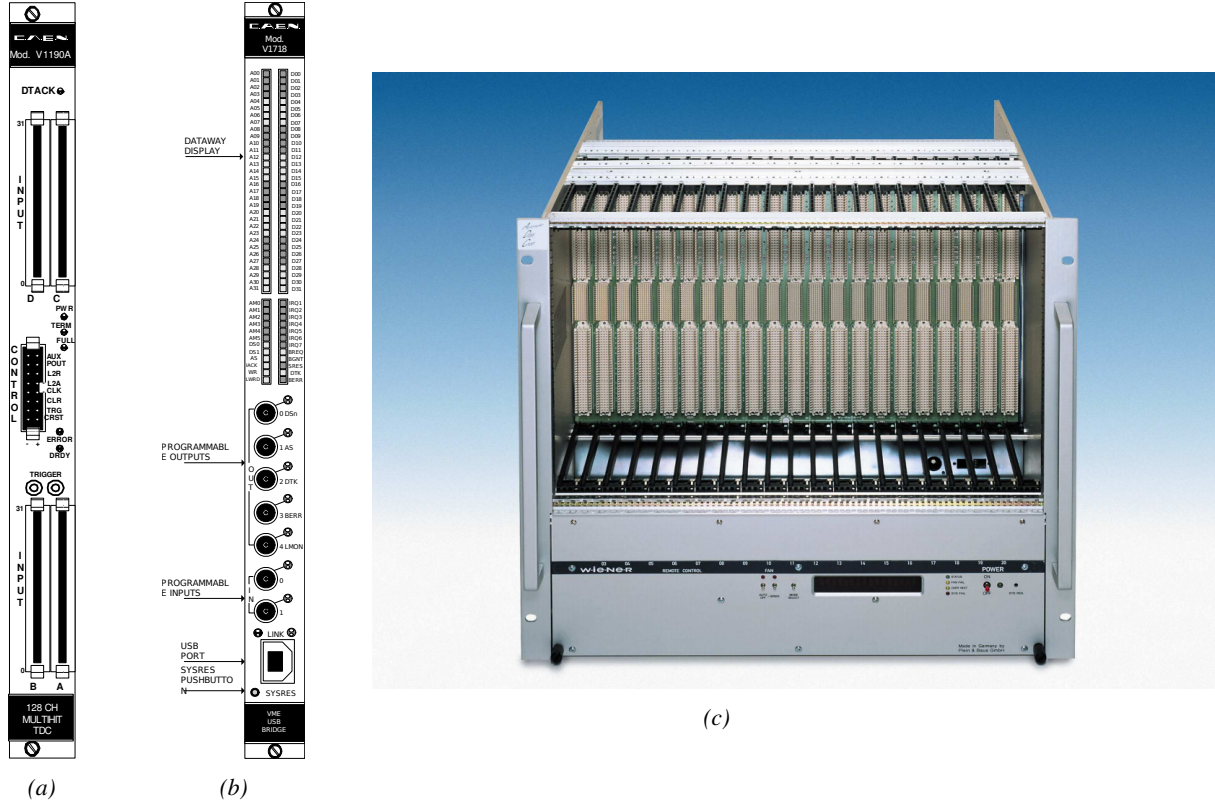


Figure A.1: (A.1a) View of the front panel of a V1190A TDC module [58]. (A.1b) View of the front panel of a V1718 Bridge module [59]. (A.1c) View of the front panel of a 6U 6021 VME crate [60].

1535

### A.4 Data read-out

1536 To efficiently perform a data readout algorithm, C++ objects to handle the VME modules (TDCs  
 1537 and VME bridge) have been created along with objects to store data and read the configuration file

1538 that comes as an input of the DAQ software.

1539

#### 1540 A.4.1 V1190A TDCs

1541 The DAQ used at GIF takes profit of the *Trigger Matching Mode* offered by V1190A modules.  
 1542 This setting is enabled through the method `v1190a::SetTrigMatching (int ntdcs)` where `ntdcs`  
 1543 is the total number of TDCs in the setup this setting needs to be enabled for (Source Code A.1). A  
 1544 trigger matching is performed in between a trigger time tag, a trigger signal sent into the TRIGGER  
 1545 input of the TDC visible on Figure A.1a, and the channel time measurements, signals recorded from  
 1546 the detectors under test in our case. Control over this data acquisition mode, explained through  
 1547 Figure A.2, is offered via 4 programmable parameters:

- 1548 • **match window:** the matching between a trigger and a hit is done within a programmable time  
 1549 window. This is set via the method

1550   **void** v1190a::SetTrigWindowWidth(Uint windowWidth, **int** ntdcs)

- 1551 • **window offset:** temporal distance between the trigger tag and the start of the trigger matching  
 1552   window. This is set via the method

1553   **void** v1190a::SetTrigWindowWidth(Uint windowWidth, **int** ntdcs)

- 1554 • **extra search margin:** an extended time window is used to ensure that all matching hits are  
 1555   found. This is set via the method

1556   **void** v1190a::SetTrigSearchMargin(Uint searchMargin, **int** ntdcs)

- 1557 • **reject margin:** older hits are automatically rejected to prevent buffer overflows and to speed  
 1558   up the search time. This is set via the method

1559   **void** v1190a::SetTrigRejectionMargin(Uint rejectMargin, **int** ntdcs)

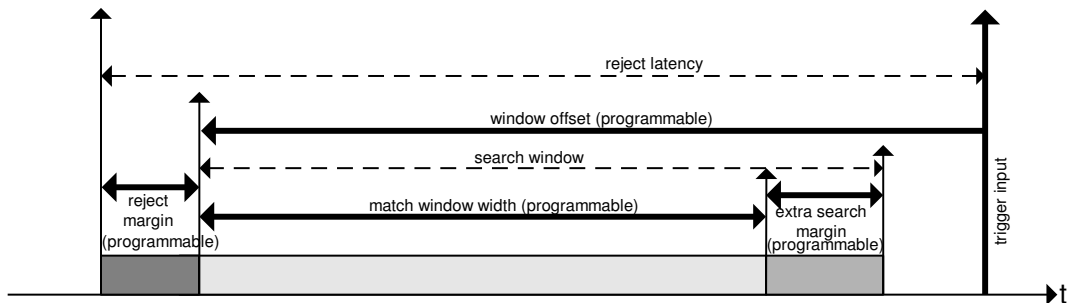


Figure A.2: Module V1190A Trigger Matching Mode timing diagram [58].

1560   Each of these 4 parameters are given in number of clocks, 1 clock being 25 ns long. It is easy to  
 1561 understand at this level that there are 3 possible functioning settings:

- 1562   • **1:** the match window is entirely contained after the trigger signal,

- 1563   • **2:** the match window overlaps the trigger signal, or

- 1564   • **3:** the match window is entirely contained before the trigger signal as displayed on Figure A.2.

1565 In both the first and second cases, the sum of the window width and of the offset can be set to  
1566 a maximum of 40 clocks, which corresponds to 1  $\mu$ s. Evidently, the offset can be negative, allowing  
1567 for a longer match window, with the constraint of having the window ending at most 1  $\mu$ s after the  
1568 trigger signal. In the third case, the maximum negative offset allowed is of 2048 clocks (12 bit) cor-  
1569 responding to 51.2  $\mu$ s, the match window being strictly smaller than the offset. In the case of GIF++,  
1570 the choice has been made to use this last setting by delaying the trigger signal. During the studies  
1571 performed in GIF++, both the efficiency of the RPCs, probed using a muon beam, and the noise or  
1572 gamma background rate are monitored. The extra search and reject margins are left unused.  
1573 To probe the efficiency of RPC detectors, the trigger time tag is provided by the coïncidence of  
1574 scintillators when a bunch of muons passes through GIF++ area is used to trigger the data acquisi-  
1575 tion. For this measurement, it is useful to reduce the match window width only to contain the muon  
1576 information. Indeed, the delay in between a trigger signal and the detection of the corresponding  
1577 muon in the RPC being very contant (typically a few tens of ns due to jitter and cable length), the  
1578 muon signals are very localised in time. Thus, due to a delay of approximalety 325 ns in between  
1579 the muons and the trigger, the settings where chosen to have a window width of 24 clocks (600 ns)  
1580 centered on the muon peak thanks to a negative offset of 29 clocks (725 ns).  
1581 On the otherhand, monitoring the rates don't require for the DAQ to look at a specific time window.  
1582 It is important to integrate enough time to have a robust measurement of the rate as the number of  
1583 hits per time unit. The triggerring signal is provided by a pulse generator at a frequency of 300 Hz  
1584 to ensure that the data taking occurs in a random way, with respect to beam physics, to probe only  
1585 the irradiation spectrum on the detectors. The match window is set to 400 clocks (10  $\mu$ s) and the  
1586 negative offset to 401 clocks as it needs to exceed the value of the match window.

```

1587
1588 class v1190a
{
    private :
        long             Handle;
        vector<Data32>   Address;
        CVDataWidth      DataWidth;
        CVAddressModifier AddressModifier;

    public:

        v1190a(long handle, IniFile *inifile, int ntdcs);
        ~v1190a();
        Data16 write_op_reg(Data32 address, int code, string error);
        Data16 read_op_reg(Data32 address, string error);
        void Reset(int ntdcs);
        void Clear(int ntdcs);
        void TestWR(Data16 value,int ntdcs);
        void CheckTDCStatus(int ntdcs);
        void CheckCommunication(int ntdcs);
        void SetTDCTestMode(Data16 mode,int ntdcs);
        void SetTrigMatching(int ntdcs);
        void SetTrigTimeSubtraction(Data16 mode,int ntdcs);
        void SetTrigWindowWidth(Uint windowHeight,int ntdcs);
        void SetTrigWindowOffset(Uint windowOffset,int ntdcs);
        void SetTrigSearchMargin(Uint searchMargin,int ntdcs);
        void SetTrigRejectionMargin(Uint rejectMargin,int ntdcs);
        void GetTrigConfiguration(int ntdcs);
        void SetTrigConfiguration(IniFile *inifile,int ntdcs);
        void SetTDCDetectionMode(Data16 mode,int ntdcs);
        void SetTDCResolution(Data16 lsb,int ntdcs);
        void SetTDCDeadTime(Data16 time,int ntdcs);
        void SetTDCHeadTrailer(Data16 mode,int ntdcs);
        void SetTDCEventSize(Data16 size,int ntdcs);
        void SwitchChannels(IniFile *inifile,int ntdcs);
        void SetIRQ(Data32 level, Data32 count,int ntdcs);
        void SetBlockTransferMode(Data16 mode,int ntdcs);
        void Set(IniFile *inifile,int ntdcs);
        void CheckStatus(CVErrorCodes status) const;
        int ReadBlockD32(Uint tdc, const Data16 address,
                         Data32 *data, const Uint words, bool ignore_berr);
        Uint Read(RAWData *DataList,int ntdcs);
};

1589
```

*Source Code A.1: Description of C++ object v1190a.*

1590     The v1190a object, defined in the DAQ software as in Source Code A.1, offers the possibility to  
1591     concatenate all TDCs in the readout setup into a single object containing a list of hardware addresses  
1592     (addresses to access the TDCs' buffer through the VME crate) and each constructor and method acts  
1593     on the list of TDCs.

1594

#### 1595     A.4.2 DataReader

1596     Enabled thanks to v1190a::SetBlockTransferMode(Data16 mode, int ntdcs), the data transfer  
1597     is done via Block Transfer (BLT). Using BLT allows to tranfer a fixed number of events called a  
1598     *block*. This is used together with an Almost Full Level (AFL) of the TDCs' output buffers, defined

1599 through `v1190a::SetIRQ(Data32 level, Data32 count, int ntdcs)`. This AFL gives the maxi-  
 1600 mum amount of 32735 words (16 bits, corresponding to the depth of a TDC output buffer) that can  
 1601 written in a buffer before an Interrupt Request (IRQ) is generated and seen by the VME Bridge,  
 1602 stopping the data acquisition to transfer the content of each TDC buffers before resuming. For each  
 1603 trigger, 6 words or more are written into the TDC buffer:

- 1604     • a **global header** providing information of the event number since the beginning of the data  
       acquisition,
- 1606     • a **TDC header**,
- 1607     • the **TDC data** (*if any*), 1 for each hit recorded during the event, providing the channel and the  
       time stamp associated to the hit,
- 1609     • a **TDC error** providing error flags,
- 1610     • a **TDC trailer**,
- 1611     • a **global trigger time tag** that provides the absolute trigger time relatively to the last reset,  
       and
- 1613     • a **global trailer** providing the total word count in the event.

1614     As previously described in Section ??, CMS RPC FEEs provide us with 100 ns long LVDS out-  
 1615 put signals that are injected into the TDCs' input. Any avalanche signal that gives a signal above the  
 1616 FEEs threshold is thus recorded by the TDCs as a hit within the match window. Each hit is assigned  
 1617 to a specific TDC channel with a time stamp, with a precision of 100 ps. The reference time,  $t_0 = 0$ ,  
 1618 is provided by the beginning of the match window. Thus for each trigger, coming from a scintillator  
 1619 coïncidence or the pulse generator, a list of hits is stored into the TDCs' buffers and will then be  
 1620 transferred into a ROOT Tree.

1621     When the BLT is used, it is easy to understand that the maximum number of words that have  
 1622 been set as ALF will not be a finite number of events or, at least, the number of events that would  
 1623 be recorded into the TDC buffers will not be a multiple of the block size. In the last BLT cycle to  
 1624 tranfer data, the number of events to transfer will most probably be lower than the block size. In that  
 1625 case, the TDC can add fillers at the end of the block but this option requires to send more data to the  
 1626 computer and is thus a little slower. Another solution is to finish the transfer after the last event by  
 1627 sending a bus error that states that the BLT reached the last event in the pile. This method has been  
 1628 chosen in GIF++.

1630     Due to irradiation, an event in GIF++ can count up to 300 words per TDC. A limit of 4096 words  
 1631 (12 bits) has been set to generate IRQ which represent from 14 to almost 700 events depending on  
 1632 the average of hits collected per event. Then the block size has been set to 100 events with enabled  
 1633 bus errors. When an AFL is reached for one of the TDCs, the VME bridge stops the acquisition by  
 1634 sending a BUSY signal.

1636

1637     The data is then transferred one TDC at a time into a structure called `RAWData` (Source Code A.2).

```
1638
1639 struct RAWData{
1640     vector<int>           *EventList;
1641     vector<int>           *NHitsList;
1642     vector<int>           *QFlagList;
1643     vector<vector<int>>   *Channellist;
1644     vector<vector<float>>  *TimeStampList;
1645 };
1646
```

1640                 *Source Code A.2: Description of data holding C++ structure `RAWData`.*

1641     In order to organize the data transfer and the data storage, an object called `DataReader` was
1642     created (Source Code A.3). On one hand, it has `v1718` and `v1190a` objects as private members for
1643     communication purposes, such as VME modules settings via the configuration file `*iniFile` or data
1644     read-out through `v1190a::Read()` and on the other hand, it contains the structure `RAWData` that allows
1645     to organise the data in vectors reproducing the tree structure of a ROOT file.

```
1646
1647 class DataReader
1648 {
1649     private:
1650     bool      StopFlag;
1651     IniFile  *iniFile;
1652     Data32    MaxTriggers;
1653     v1718    *VME;
1654     int       nTDCs;
1655     v1190a   *TDCs;
1656     RAWData  TDCData;
1657
1658     public:
1659     DataReader();
1660     virtual ~DataReader();
1661     void      SetIniFile(string inifilename);
1662     void      SetMaxTriggers();
1663     Data32    GetMaxTriggers();
1664     void      SetVME();
1665     void      SetTDC();
1666     int       GetQFlag(Uint it);
1667     void      Init(string inifilename);
1668     void      FlushBuffer();
1669     void      Update();
1670     string   GetFileName();
1671     void      WriteRunRegistry(string filename);
1672     void      Run();
1673 };
1674
```

1648                 *Source Code A.3: Description of C++ object `DataReader`.*

1649     Each event is transferred from `TDCData` and saved into branches of a ROOT `TTree` as 3 integers
1650     that represent the event ID (`EventCount`), the number of hits read from the TDCs (`nHits`), and the
1651     quality flag that provides information for any problem in the data transfer (`qflag`), and 2 lists of
1652     `nHits` elements containing the fired TDC channels (`TDCCh`) and their respective time stamps (`TDCTS`),
1653     as presented in Source Code A.4. The ROOT file file is named using information contained into
1654     the configuration file, presented in section A.5.2. The needed information is extracted using method
1655     `DataReader::GetFileName()` and allow to build the output filename format `ScanXXXXXX_HVX_DAQ.root`

1656 where ScanXXXXXX is a 6 digit number representing the scan number into GIFT++ database and HVX  
 1657 the HV step within the scan that can be more than a single digit. An example of ROOT data file is  
 1658 provided with Figure A.3.

```
1659
1660 RAWData TDCData;
TFile *outputFile = new TFile(outputFileName.c_str(),"recreate");
TTree *RAWDataTree = new TTree("RAWData","RAWData");

int EventCount = -9;
int nHits = -8;
int qflag = -7;
vector<int> TDCCh;
vector<float> TDCTS;

RAWDataTree->Branch("EventNumber",&EventCount, "EventNumber/I");
RAWDataTree->Branch("number_of_hits",&nHits,"number_of_hits/I");
RAWDataTree->Branch("Quality_flag",&qflag,"Quality_flag/I");
RAWDataTree->Branch("TDC_channel",&TDCCh);
RAWDataTree->Branch("TDC_TimeStamp",&TDCTS);

1661 //...
//Here read the TDC data using v1190a::Read() and place it into
//TDCData for as long as you didn't collect the requested amount
//of data.
//...

for(Uint i=0; i<TDCData.EventList->size(); i++){
    EventCount = TDCData.EventList->at(i);
    nHits = TDCData.NHitsList->at(i);
    qflag = TDCData.QFlagList->at(i);
    TDCCh = TDCData.ChannelList->at(i);
    TDCTS = TDCData.TimeStampList->at(i);
    RAWDataTree->Fill();
}
```

1661 *Source Code A.4: Highlight of the data transfer and organisation within DataReader::Run() after the data has been collected into TDCData.*

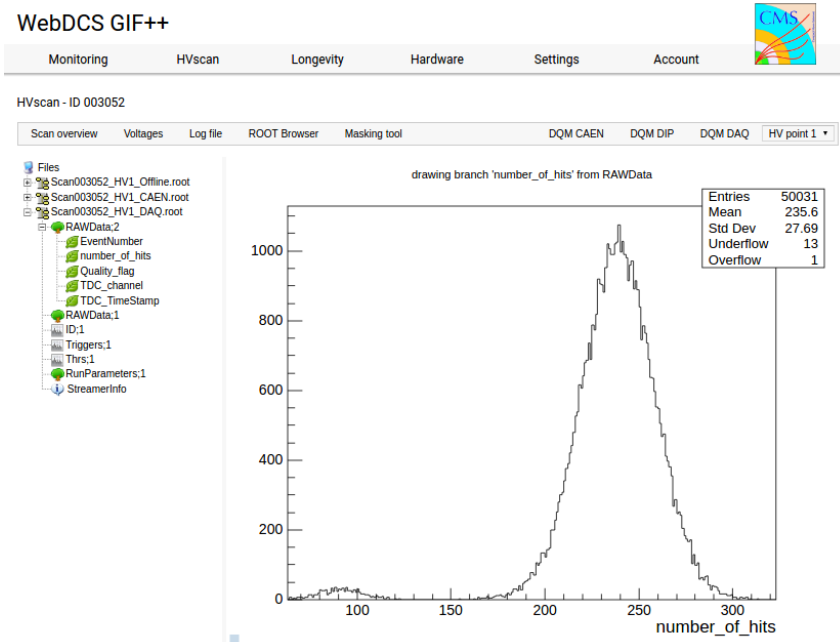


*Figure A.3: Structure of the ROOT output file generated by the DAQ. The 5 branches (EventNumber, number\_of\_hits, Quality\_flag, TDC\_channel and TDC\_TimeStamp) are visible on the left panel of the ROOT browser. On the right panel is visible the histogram corresponding to the variable nHits. In this specific example, there were approximately 50k events recorded to measure the gamma irradiation rate on the detectors. Each event is stored as a single entry in the TTree.*

#### 1662    A.4.3 Data quality flag

1663    Among the parameters that are recorded for each event, the quality flag, defined in Source Code A.5,  
 1664    is determined on the fly by checking the data recorded by every single TDC. From method `v1190a::Read()`,  
 1665    it can be understood that the content of each TDC buffer is readout one TDC at a time. Entries are  
 1666    created in the data list for the first TDC and then, when the second buffer is readout, events corre-  
 1667    sponding to entries that have already been created to store data for the previous TDC are added to  
 1668    the existing list element. On the contrary, when an event entry has not been yet created in the data  
 1669    list, a new entry is created.

```
1670
 1671 typedef enum _QualityFlag {
 1672     GOOD      = 1,
 1673     CORRUPTED = 0
 1674 } QualityFlag;
```

1672    *Source Code A.5: Definition of the quality flag `enum`.*

1673    It is possible that each TDC buffer contains a different number of events. In cases where the first  
 1674    element in the buffer list is an event for corresponds to a new entry, the difference in between the  
 1675    entry from the buffer and the last entry in the data list is recorded and checked. If it is greater than 1,  
 1676    what should never be the case, the quality flag is set to CORRUPTED for this TDC and an empty entry  
 1677    is created in the place of the missing ones. Missing entries are believe to be the result of a bad hold

1678 on the TDC buffers at the moment of the readout. Indeed, the software hold is effective only on 1  
 1679 TDC at a time and no solution as been found yet to completely block the writting in the buffers when  
 1680 an IRQ is received.

1681 At the end of each BLT cycle, the ID of the last entry stored for each TDC buffer is not recorded.  
 1682 When starting the next cycle, if the first entry in the pile corresponds to an event already existing  
 1683 in the list, the readout will start from this list element and will not be able to check the difference  
 1684 in between this entry's ID and the one of the last entry that was recorded for this TDC buffer in  
 1685 the previous cycle. In the case events were missing, the flag stays at its initial value of 0, which is  
 1686 similar to CORRUPTED and it is assumed that then this TDC will not contribute to `number_of_hits`,  
 1687 `TDC_channel` or `TDC_TimeStamp`.

1688 Finally, since there will be 1 `RAWData` entry per TDC for each event (meaning `nTDCs` entries,  
 1689 referring to `DataReader` private attribute), the individual flags of each TDC will be added together.  
 1690 The final format is an integer composed `nTDCs` digits where each digit is the flag of a specific TDC.  
 1691 This is constructed using powers of 10 like follows:

```
1692     TDC 0: QFlag = 100 × _QualityFlag
1693     TDC 1: QFlag = 101 × _QualityFlag
1694     ...
1695     TDC N: QFlag = 10N × _QualityFlag
```

1696 and the final flag to be with N digits:

```
1697     QFlag = n....3210
```

1698 each digit being 1 or 0. Below is given an example with a 4 TDCs setup.

```
1699     If all TDCs were good : QFlag = 1111,
```

```
1700     but if TDC 2 was corrupted : QFlag = 1011.
```

1701 When data taking is over and the data contained in the dynamical `RAWData` structure is transferred  
 1702 to the ROOT file, all the 0s are changed into 2s by calling the method `DataReader::GetQFlag()`.  
 1703 This will help translating the flag without knowing the number of TDCs beforehand. Indeed, a flag  
 1704 111 could be due to a 3 TDC setup with 3 good individual TDC flags or to a more than 3 TDC setup  
 1705 with TDCs those ID is greater than 2 being CORRUPTED, thus giving a 0.

1706 The quality flag has been introduced quite late, in October 2017 only, to the list of GIFT++ DAQ  
 1707 parameters to be recorded into the output ROOT file. Before this addition, the missing data, corrupting  
 1708 the quality for the offline analysis, was contributing to artificially fill data with lower multiplicity.  
 1709 Looking at `TBranch number_of_hits` provides an information about the data of the full GIFT++  
 1710 setup. When a TDC is not able to transfer data for a specific event, the effect is a reduction of the  
 1711 total number of hits recorded in the full setup, this is what can be seen from Figure A.4. After offline  
 1712 reconstruction detector by detector, the effect of missing events can be seen in the artificially filled  
 1713 bin at multiplicity 0 shown in Figure A.5. Nonetheless, for data with high irradiation levels, as it is  
 1714 the case for Figure A.5a, discarding the fake multiplicity 0 data can be done easily during the offline  
 1715 analysis. At lower radiation, the missing events contribution becomes more problematic as the multi-  
 1716 tiplicity distribution overlaps the multiplicity 0 and that in the same time the proportion of missing

1717 events decreases. Attempts to fit the distribution with a Poisson or skew distribution function were  
 1718 not conclusive and this very problem has been at the origin of the quality flag that allows to give a  
 1719 non ambiguous information about each event quality.

1720

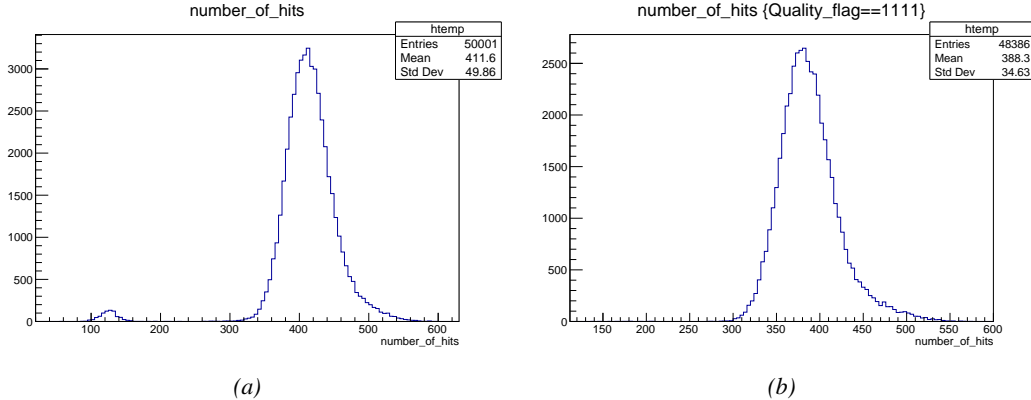


*Figure A.4: The effect of the quality flag is explained by presenting the content of TBranch `number_of_hits` of a data file without `Quality_flag` in Figure A.4a and the content of the same TBranch for data corresponding to a `Quality_flag` where all TDCs were labelled as `GOOD` in Figure A.4b taken with similar conditions. It can be noted that the number of entries in Figure A.4b is slightly lower than in Figure A.4a due to the excluded events.*

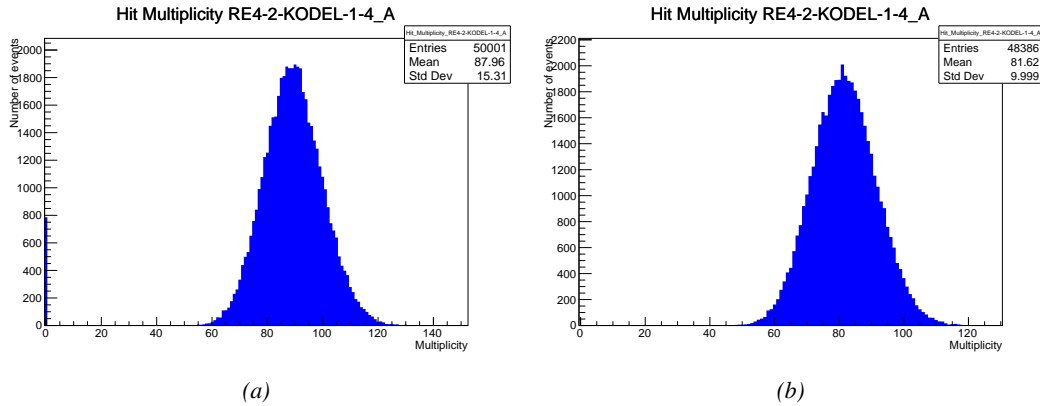


*Figure A.5: Using the same data as previously showed in Figure A.4, the effect of the quality flag is explained by presenting the reconstructed hit multiplicity of a data file without `Quality_flag` in Figure A.5a and the reconstructed content of the same RPC partition for data corresponding to a `Quality_flag` where all TDCs were labelled as `GOOD` in Figure A.5b taken with similar conditions. The artificial high content of bin 0 is completely suppressed.*

1721

## A.5 Communications

1722 To ensure data readout and dialog in between the machine and the TDCs or in between the webDCS  
 1723 and the DAQ, different communication solutions were used. First of all, it is important to have a

1724 module to allow the communication in between the TDCs and the computer from which the DAQ  
 1725 operates. When this communication is effective, shifters using the webDCS to control data taking  
 1726 can thus send instructions to the DAQ.

1727

### 1728 A.5.1 V1718 USB Bridge

1729 In the previous section, the data transfer has been discussed. The importance of the `v1718` object  
 1730 (Source Code A.6), used as private member of `DataReader`, was not explicated. VME master  
 1731 modules are used for communication purposes as they host the USB port that connects the pow-  
 1732 ered crate buffer to the computer where the DAQ is installed. From the source code point of view,  
 1733 this object is used to control the communication status, by reading the returned error codes with  
 1734 `v1718::CheckStatus()`, or to check for IRQs coming from the TDCs through `v1718::CheckIRQ()`.  
 1735 Finally, to ensure that triggers are blocked at the hardware level, a NIM pulse is sent out of one of the  
 1736 5 programmable outputs (`v1718::SendBUSY()`) to the VETO of the coincidence module where the  
 1737 trigger signals originate from. As long as this signal is ON, no trigger can reach the TDCs anymore.  
 1738

```
1739
  class v1718{
    private:
      int Handle;
      Data32 Data;           // Data
      CVIRQLevels Level;    // Interrupt level
      CVAddressModifier AM;  // Addressing Mode
      CVDataWidth dataSize; // Data Format
      Data32 BaseAddress;   // Base Address

    public:
      v1718(IniFile *inifile);
      ~v1718();
      long GetHandle(void) const;
      int GetData(Data16 data);
      Data16 GetData(void);
      int SetLevel(CVIRQLevels level);
      CVIRQLevels GetLevel(void);
      int SetAM(CVAddressModifier am);
      CVAddressModifier GetAM(void);
      int SetDataSize(CVDataWidth datasize);
      CVDataWidth GetDataSize(void);
      int SetBaseAddress(Data16 baseaddress);
      Data16 GetBaseAddress(void);
      void CheckStatus(CVErrorCodes status) const;
      void CheckIRQ();
      void SetPulsers();
      void SendBUSY(BusyLevel level);
  };

```

1740 *Source Code A.6: Description of C++ object v1718.*

### 1741 A.5.2 Configuration file

1742 The DAQ software takes as input a configuration file written using INI standard [61]. This file is  
 1743 partly filled with the information provided by the shifters when starting data acquisition using the  
 1744 webDCS, as shown by Figure A.6. This information is written in section [`General`] and will later

1745 be stored in the ROOT file that contains the DAQ data as can be seen from Figure A.3. Indeed,  
 1746 another `TTree` called `RunParameters` as well as the 2 histograms `ID`, containing the scan number,  
 1747 start and stop time stamps, and `Triggers`, containing the number of triggers requested by the shifter,  
 1748 are available in the data files. Moreover, `ScanID` and `HV` are then used to construct the file name  
 1749 thanks to the method `DataReader::GetFileName()`.

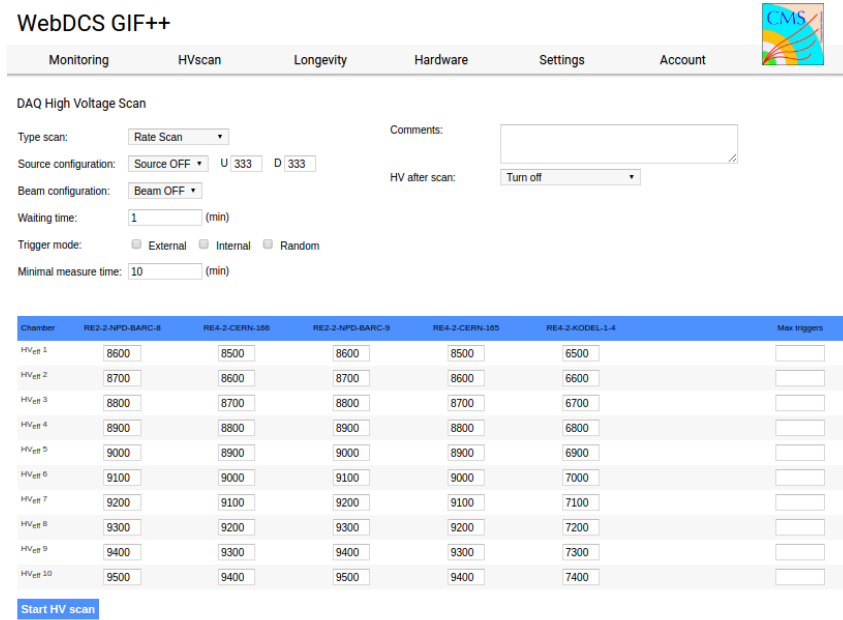


Figure A.6: WebDCS DAQ scan page. On this page, shifters need to choose the type of scan (Rate, Efficiency or Noise Reference scan), the gamma source configuration at the moment of data taking, the beam configuration, and the trigger mode. These information will be stored in the DAQ ROOT output. Are also given the minimal measurement time and waiting time after ramping up of the detectors is over before starting the data acquisition. Then, the list of HV points to scan and the number of triggers for each run of the scan are given in the table underneath.

1750 The rest of the information is written beforehand in the configuration file template, as explicated  
 1751 in Source Code A.7, and contains the hardware addresses to the different VME modules in the  
 1752 setup as well as settings for the TDCs. As the TDC settings available in the configuration file are not  
 1753 supposed to be modified, an improvement would be to remove them from the configuration file and  
 1754 to hardcode them inside of the DAQ code itself or to place them into a different INI file that would  
 1755 host only the TDC settings to lower the probability for a bad manipulation of the configuration file  
 1756 that can be modified from one of webDCS' menus.

1757

```
[General]
TdcS=4
ScanID=$scanid
HV=$HV
RunType=$runtype
MaxTriggers=$maxtriggers
Beam=$beam
[VMEInterface]
Type=V1718
BaseAddress=0xFF0000
Name=VmeInterface
[TDC0]
Type=V1190A
BaseAddress=0x00000000
Name=Tdc0
StatusA00-15=1
StatusA16-31=1
StatusB00-15=1
StatusB16-31=1
StatusC00-15=1
StatusC16-31=1
StatusD00-15=1
StatusD16-31=1
[TDC1]
Type=V1190A
BaseAddress=0x11110000
Name=Tdc1
StatusA00-15=1
StatusA16-31=1
StatusB00-15=1
StatusB16-31=1
StatusC00-15=1
StatusC16-31=1
StatusD00-15=1
StatusD16-31=1
[TDC2]
Type=V1190A
BaseAddress=0x22220000
Name=Tdc2
StatusA00-15=1
StatusA16-31=1
StatusB00-15=1
StatusB16-31=1
StatusC00-15=1
StatusC16-31=1
StatusD00-15=1
StatusD16-31=1
[TDC3]
Type=V1190A
BaseAddress=0x44440000
Name=Tdc3
StatusA00-15=1
StatusA16-31=1
StatusB00-15=1
StatusB16-31=1
StatusC00-15=1
StatusC16-31=1
StatusD00-15=1
StatusD16-31=1
[TDCSettings]
TriggerExtraSearchMargin=0
TriggerRejectMargin=0
TriggerTimeSubtraction=0b1
TdcDetectionMode=0b01
TdcResolution=0b10
TdcDeadTime=0b00
TdcHeadTrailer=0b1
TdcEventSize=0b1001
TdcTestMode=0b0
BLTMode=1
```

1758

*Source Code A.7: INI configuration file template for 4 TDCs. In section [General], the number of TDCs is explicitated and information about the ongoing run is given. Then, there are sections for each and every VME modules. There buffer addresses are given and for the TDCs, the list of channels to enable is given. Finally, in section [TDCSettings], a part of the TDC settings are given.*

1760     In order to retrieve the information of the configuration file, the object `IniFile` has been developed  
 1761     to provide an INI parser, presented in Source Code A.8. It contains private methods returning a  
 1762     boolean to check the type of line written in the file, whether a comment, a group header or a key line  
 1763     (`IniFile::CheckIfComment()`, `IniFile::CheckIfGroup()` and `IniFile::CheckIfToken()`). The  
 1764     key may sometimes be referred to as *token* in the source code. Moreover, the private element  
 1765     `FileData` is a map of `const string` to `string` that allows to store the data contained inside the  
 1766     configuration file via the public method `IniFile::GetFileData()` following the formatting (see  
 1767     method `IniFile::Read()`):

```
1768
  1769     string group, token, value;
  // Get the field values for the 3 strings.
  // Then concatenate group and token together as a single string
  // with a dot separation.
  token = group + "." + token;
  FileData[token] = value;
```

1770     More methods have been written to translate the different keys into the right variable format  
 1771     when used by the DAQ. For example, to get a `float` value out of the configuration file data, knowing  
 1772     the group and the key needed, the method `IniFile::floatType()` can be used. It takes 3 arguments  
 1773     being the group name and key name (both `string`), and a default `float` value used as exception in  
 1774     the case the expected combination of group and key cannot be found in the configuration file. This  
 1775     default value is then used and the DAQ continues on working after sending an alert in the log file for  
 1776     further debugging.

```

1777
typedef map< const string, string > IniFileData;

class IniFile{
    private:
        bool      CheckIfComment (string line);
        bool      CheckIfGroup (string line, string& group);
        bool      CheckIfToken (string line, string& key, string& value);
        string    FileName;
        IniFileData FileData;
        int       Error;

    public:
        IniFile();
        IniFile(string filename);
        virtual ~IniFile();

        // Basic file operations
        void      SetFileName(string filename);
        int       Read();
        int       Write();
        IniFileData GetFileData();

        // Data readout methods
        Data32    addressType (string groupname, string keyname, Data32
→      defaultvalue);
        long      intType     (string groupname, string keyname, long
→      defaultvalue);
        long long  longType   (string groupname, string keyname, long long
→      defaultvalue );
        string    stringType  (string groupname, string keyname, string
→      defaultvalue );
        float     floatType   (string groupname, string keyname, float
→      defaultvalue );

        // Error methods
        string    GetErrorMsg();
};

1778

```

1779       *Source Code A.8: Description of C++ object `IniFile` used as a parser for INI file format.*

### 1780     A.5.3 WebDCS/DAQ intercommunication

1781 When shifters send instructions to the DAQ via the configuration file, it is the webDCS itself that  
 1782 gives the start command to the DAQ and then the 2 softwares use inter-process communication  
 1783 through file to synchronise themselves. This communication file is represented by the variable `const`  
 1784 `string __runstatuspath`.

1785 On one side, the webDCS sends commands or status that are readout by the DAQ:

- 1786     ● INIT, status sent when launching a scan and read via function `CtrlRunStatus(...)`,
- 1787     ● START, command to start data taking and read via function `CheckSTART()`,
- 1788     ● STOP, command to stop data taking at the end of the scan and read via function `CheckSTOP()`,  
 1789       and
- 1790     ● KILL, command to kill data taking sent by user and read via function `CheckKILL()`

1791 and on the other, the DAQ sends status that are controled by the webDCS:

- 1792     ● `DAQ_RDY`, sent with `SendDAQReady()` to signify that the DAQ is ready to receive commands  
1793       from the webDCS,
- 1794     ● `RUNNING`, sent with `SendDAQRunning()` to signify that the DAQ is taking data,
- 1795     ● `DAQ_ERR`, sent with `SendDAQError()` to signify that the DAQ didn't receive the expected com-  
1796       mand from the webDCS or that the launch command didn't have the right number of argu-  
1797       ments,
- 1798     ● `RD_ERR`, sent when the DAQ wasn't able to read the communication file, and
- 1799     ● `WR_ERR`, sent when the DAQ wasn't able to write into the communication file.

#### 1800 **A.5.4 Example of inter-process communication cycle**

1801 Under normal conditions, the webDCS and the DAQ processes exchange commands and status via  
1802 the file hosted at the address `__runstatuspath`, as explained in subsection A.5.3. An example of  
1803 cycle is given in Table A.1. In this example, the steps 3 to 5 are repeated as long as the webDCS tells  
1804 the DAQ to take data. A data taking cycle is the equivalent as what is called a *Scan* in GIFT++ jargon,  
1805 referring to a set a runs with several HV steps. Each repetition of steps 3 to 5 is then equivalent to a  
1806 single *Run*.

1807  
1808 At any moment during the data taking, for any reason, the shifter can decide that the data taking  
1809 needs to be stopped before it reached the end of the scheduled cycle. Thus at any moment on the  
1810 cycle, the content of the inter-process communication file will be changed to `KILL` and the DAQ will  
1811 shut down right away. The DAQ checks for `KILL` signals every 5s after the TDCs configuration is  
1812 over. So far, the function `CheckKILL()` has been used only inside of the data taking loop of method  
1813 `DataReader::Run()` and thus, if the shifter decides to KILL the data taking during the TDC con-  
1814 figuration phase or the HV ramping in between 2 HV steps, the DAQ will not be stopped smoothly  
1815 and a *force kill* command will be sent to stop the DAQ process that is still awake on the computer.  
1816 Improvements can be brought on this part of the software to make sure that the DAQ can safely  
1817 shutdown at any moment.

#### 1819 **A.6 Software export**

1820 In section A.2 was discussed the fact that the DAQ as written in its last version is not a standalone  
1821 software. It is possible to make it a standalone program that could be adapted to any VME setup  
1822 using V1190A and V1718 modules by creating a GUI for the software or by printing the log mes-  
1823 sages that are normally printed in the webDCS through the log file, directly into the terminal. This  
1824 method was used by the DAQ up to version 3.0 moment where the webDCS was completed. Also, it  
1825 is possible to check branches of DAQ v2.X to have example of communication through a terminal.

1826  
1827 DAQ v2.X is nonetheless limited in it's possibilities and requires a lot of offline manual interven-  
1828 tions from the users. Indeed, there is no communication of the software with the detectors' power  
1829 supply system that would allow for a user a predefine a list of voltages to operate the detectors at

step	actions of webDCS	status of DAQ	__runstatuspath
1	launch DAQ ramp voltages ramping over wait for currents stabilization	readout of IniFile configuration of TDCs	INIT
2		configuration done send DAQ ready wait for START signal	DAQ_RDY
3	waiting time over send START		START
4	wait for run to end monitor DAQ run status	data taking ongoing check for KILL signal	RUNNING
5		run over send DAQ_RDY wait for next DCS signal	DAQ_RDY
6	ramp voltages ramping over wait for currents stabilization		DAQ_RDY
3	waiting time over send START		START
4	wait for run to end monitor DAQ run status	update IniFile information data taking ongoing check for KILL signal	RUNNING
5		run over send DAQ_RDY wait for next DCS signal	DAQ_RDY
7	send command STOP	DAQ shuts down	STOP

Table A.1: Inter-process communication cycles in between the webDCS and the DAQ through file string signals.

1830 and loop over to take data without any further manual intervention. In v2.X, the data is taken for a  
1831 single detector setting and at the end of each run, the softwares asks the user if he intends on taking  
1832 more runs. If so, the software invites the user to set the operating voltages accordingly to what is  
1833 necessary and to manual update the configuration file in consequence. This working mode can be a  
1834 very first approach before an evolution and has been successfully used by colleagues from different  
1835 collaborations.

1836

1837 For a more robust operation, it is recommended to develop a GUI or a web application to inter-  
1838 face the DAQ. Moreover, to limit the amount of manual interventions, and thus the probability to  
1839 make mistakes, it is also recommended to add an extra feature into the DAQ by installing the HV  
1840 Wrapper library provided by CAEN of which an example of use in a similar DAQ software devel-  
1841 opped by a master student of UGent, and called TinyDAQ, is provided on UGent's github. Then, this  
1842 HV Wrapper will help you communicating with and give instructions to a CAEN HV powered crate  
1843 and can be added into the DAQ at the same level where the communication with the user was made  
1844 in DAQ v2.X. In case you are using another kind of power system for your detectors, it is stringly  
1845 adviced to use HV modules or crates that can be remotely controled via a using C++ libraries.

1846

# B

1847

1848

## Details on the offline analysis package

1849 The data collected in GIF++ thanks to the DAQ described in Appendix A is difficult to interpret by  
1850 a human user that doesn't have a clear idea of the raw data architecture of the ROOT data files. In  
1851 order to render the data human readable, a C++ offline analysis tool was designed to provide users  
1852 with detector by detector histograms that give a clear overview of the parameters monitored during  
1853 the data acquisition [62]. In this appendix, details about this software in the context of GIF++, as of  
1854 how the software was written and how it functions will be given.

### 1855 B.1 GIF++ Offline Analysis file tree

1856 GIF++ Offline Analysis source code is fully available on github at [https://github.com/aafagot/GIF\\_OfflineAnalysis](https://github.com/aafagot/GIF_OfflineAnalysis). The software requires ROOT as non-optionnal dependency  
1857 as it takes ROOT files in input and write an output ROOT file containing histograms. To compile the  
1858 GIF++ Offline Analysis project is compiled with cmake. To compile, first a build/ directory must  
1859 be created to compile from there:

```
1861 mkdir build
1862 cd build
1863 cmake ..
1864 make
1865 make install
```

1863 To clean the directory and create a new build directory, the bash script cleandir.sh can be used:

```
1864
1865 ./cleandir.sh
```

1866 The source code tree is provided below along with comments to give an overview of the files' con-  
1867 tent. The different objects created for this project (`Infrastructure`, `Trolley`, `RPC`, `Mapping`, `RPCHit`,  
1868 `RPCCluster` and `Inifile`) will be described in details in the following sections.

1869

```

GIF_OfflineAnalysis
├── bin
│   └── offlineanalysis ..... EXECUTABLE
├── build..... CMAKE COMPILATION DIRECTORY
└── ...
    ├── include..... LIST OF C++ HEADER FILES
    │   ├── Cluster.h..... DECLARATION OF OBJECT RPCCLUSTER
    │   ├── Current.h..... DECLARATION OF GETCURRENT ANALYSIS MACRO
    │   ├── GIFTrolley.h..... DECLARATION OF OBJECT TROLLEY
    │   ├── Infrastructure.h..... DECLARATION OF OBJECT INFRASTRUCTURE
    │   ├── IniFile.h..... DECLARATION OF OBJECT INI FILE FORINI PARSER
    │   ├── Mapping.h..... DECLARATION OF OBJECT MAPPING
    │   ├── MsgSvc.h..... DECLARATION OF OFFLINE LOG MESSAGES
    │   ├── OfflineAnalysis.h..... DECLARATION OF DATA ANALYSIS MACRO
    │   ├── RPCTracker.h..... DECLARATION OF OBJECT RPC
    │   ├── RPCHit.h..... DECLARATION OF OBJECT RPCHIT
    │   ├── types.h..... DEFINITION OF USEFUL VARIABLE TYPES
    │   └── utils.h..... DECLARATION OF USEFUL FUNCTIONS
    ├── obj..... BINARY FILES CREATED BY COMPILER
    └── ...
        ├── src..... LIST OF C++ SOURCE FILES
        │   ├── Cluster.cc..... DEFINITION OF OBJECT RPCCLUSTER
        │   ├── Current.cc..... DEFINITION OF GETCURRENT ANALYSIS MACRO
        │   ├── GIFTrolley.cc..... DEFINITION OF OBJECT TROLLEY
        │   ├── Infrastructure.cc..... DEFINITION OF OBJECT INFRASTRUCTURE
        │   ├── IniFile.cc..... DEFINITION OF OBJECT INI FILE FORINI PARSER
        │   ├── main.cc..... MAIN FILE
        │   ├── Mapping.cc..... DEFINITION OF OBJECT MAPPING
        │   ├── MsgSvc.cc..... DECLARATION OF OFFLINE LOG MESSAGES
        │   ├── OfflineAnalysis.cc..... DECLARATION OF DATA ANALYSIS MACRO
        │   ├── RPCTracker.cc..... DECLARATION OF OBJECT RPC
        │   ├── RPCHit.cc..... DECLARATION OF OBJECT RPCHIT
        │   └── utils.cc..... DEFINITION OF USEFUL FUNCTIONS
        ├── cleandir.sh..... BASH SCRIPT TO CLEAN BUILD DIRECTORY
        ├── CMakeLists.txt..... SET OF INSTRUCTIONS FOR CMAKE
        ├── config.h.in..... DEFINITION OF VERSION NUMBER
        └── README.md..... README FILE FOR GITHUB

```

1870

## B.2 Usage of the Offline Analysis

1871

In order to use the Offline Analysis tool, it is necessary to know the Scan number and the HV Step of the run that needs to be analysed. This information needs to be written in the following format:

1873

1874

```
Scan00XXXX_HVY
```

1875

where XXXX is the scan ID and Y is the high voltage step (in case of a high voltage scan, data will be taken for several HV steps). This format corresponds to the base name of data files in the database

1876

1877 of the Gif++ webDCS. Usually, the offline analysis tool is automatically called by the webDCS at  
 1878 the end of data taking or by a user from the webDCS panel if an update of the tool was brought.  
 1879 Nonetheless, an expert can locally launch the analysis for tests on the Gif++ computer, or a user can  
 1880 get the code on its local machine from github and download data from the webDCS for its own anal-  
 1881 ysis. To launch the code, the following command can be used from the `GIF_OfflineAnalysis` folder:

1882  
 1883     `bin/offlineanalysis /path/to/Scan00XXXX_HVY`

1884 where, `/path/to/Scan00XXXX_HVY` refers to the local data files. Then, the offline tool will by itself  
 1885 take care of finding all available ROOT data files present in the folder, as listed below:

- 1886
  - 1887         ● `Scan00XXXX_HVY_DAQ.root` containing the TDC data as described in Appendix ?? (events, hit  
     and timestamp lists), and
  - 1888         ● `Scan00XXXX_HVY_CAEN.root` containing the CAEN mainframe data recorded by the monitor-  
     ing tool webDCS during data taking (HVs and currents of every HV channels). This file is  
     created independently of the DAQ.

## 1891 **B.2.1 Output of the offline tool**

### 1892 **B.2.1.1 ROOT file**

1893 The analysis gives in output ROOT datafiles that are saved into the data folder and called using the  
 1894 naming convention `Scan00XXXX_HVY_Offline.root`. Inside those, a list of `TH1` histograms can be  
 1895 found. Its size will vary as a function of the number of detectors in the setup as each set of histograms  
 1896 is produced detector by detector. For each partition of each chamber, can be found:

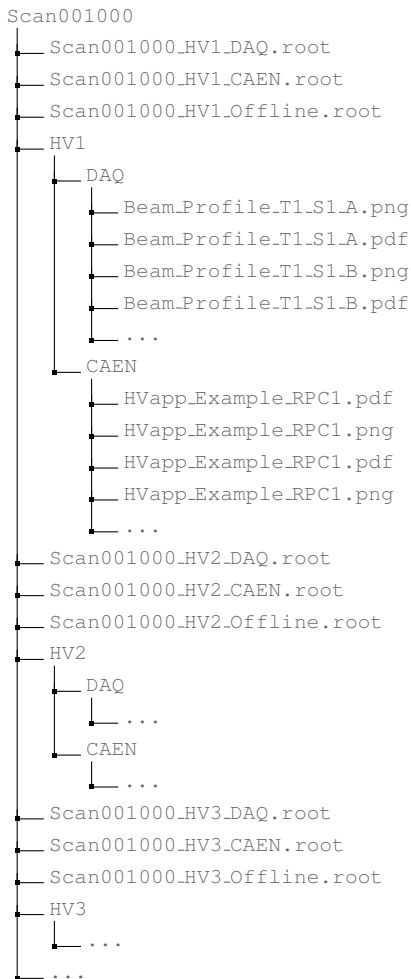
- 1897
  - 1898         ● `Time_Profile_Tt_Sc_p` shows the time profile of all recorded events (number of events per  
     time bin),
  - 1899         ● `Hit_Profile_Tt_Sc_p` shows the hit profile of all recorded events (number of events per chan-  
     nel),
  - 1900         ● `Hit_Multiplicity_Tt_Sc_p` shows the hit multiplicity (number of hits per event) of all recorded  
     events (number of occurrences per multiplicity bin),
  - 1901         ● `Strip_Mean_Noise_Tt_Sc_p` shows noise/gamma rate per unit area for each strip in a se-  
     lected time range. After filters are applied on `Time_Profile_Tt_Sc_p`, the filtered version  
     of `Hit_Profile_Tt_Sc_p` is normalised to the total integrated time and active detection area  
     of a single channel,
  - 1902         ● `Strip_Activity_Tt_Sc_p` shows noise/gamma activity for each strip (normalised version of  
     previous histogram - strip activity = strip rate / average partition rate),
  - 1903         ● `Strip_Homogeneity_Tt_Sc_p` shows the *homogeneity* of a given partition ( $\text{homogeneity} = \exp(-\text{strip rates standard deviation}(\text{strip rates in partition}/\text{average partition rate}))$ ),
  - 1904         ● `mask_Strip_Mean_Noise_Tt_Sc_p` shows noise/gamma rate per unit area for each masked  
     strip in a selected time range. Offline, the user can control the noise/gamma rate and decide to  
     mask the strips that are judged to be noisy or dead. This is done via the *Masking Tool* provided  
     by the webDCS,

- 1915     ● `mask_Strip_Activity_Tt_Sc_p` shows noise/gamma activity per unit area for each masked  
1916     strip with respect to the average rate of active strips,
- 1917     ● `NoiseCSize_H_Tt_Sc_p` shows noise/gamma cluster size, a cluster being constructed out of  
1918     adjacent strips giving a signal at the *same time* (hits within a time window of 25 ns),
- 1919     ● `NoiseCMult_H_Tt_Sc_p` shows noise/gamma cluster multiplicity (number of reconstructed  
1920     clusters per event),
- 1921     ● `Chip_Mean_Noise_Tt_Sc_p` shows the same information than `Strip_Mean_Noise_Tt_Scp` us-  
1922     ing a different binning (1 chip corresponds to 8 strips),
- 1923     ● `Chip_Activity_Tt_Sc_p` shows the same information than `Strip_Activity_Tt_Scp` using  
1924     chip binning,
- 1925     ● `Chip_Homogeneity_Tt_Sc_p` shows the homogeneity of a given partition using chip binning,
- 1926     ● `Beam_Profile_Tt_Sc_p` shows the estimated beam profile when taking efficiency scan. This  
1927     is obtained by filtering `Time_Profile_Tt_Sc_p` to only consider the muon peak where the  
1928     noise/gamma background has been subtracted. The resulting hit profile corresponds to the  
1929     beam profile on the detector channels,
- 1930     ● `L0_Efficiency_Tt_Sc_p` shows the level 0 efficiency that was estimated **without** muon track-  
1931     ing,
- 1932     ● `MuonCSize_H_Tt_Sc_p` shows the level 0 muon cluster size that was estimated **without** muon  
1933     tracking, and
- 1934     ● `MuonCMult_H_Tt_Sc_p` shows the level 0 muon cluster multiplicity that was estimated **without**  
1935     muon tracking.

1936     In the histogram labels, *t* stands for the trolley number (1 or 3), *c* for the chamber slot label in  
1937     trolley *t* and *p* for the partition label (A, B, C or D depending on the chamber layout) as explained  
1938     in Chapter ??.

1939     In the context of GIF++, an extra script called by the webDCS is called to extract the histograms  
1940     from the ROOT files. The histograms are then stored in PNG and PDF formats into the correspond-  
1941     ing folder (a single folder per HV step, so per ROOT file). the goal is to then display the histograms  
1942     on the Data Quality Monitoring (DQM) page of the webDCS in order for the users to control the  
1943     quality of the data taking at the end of data taking. An example of histogram organisation is given  
1944     below:

1945  
1946



**1947      Here can put some screens from the webDCS to show the DQM and the plots available to users.**

**1948**

### **1949      B.2.1.2 CSV files**

**1950      Moreover, up to 3 CSV files can be created depending on which ones of the 3 input files were in the  
1951      data folder:**

- 1952      • Offline-Corrupted.csv , is used to keep track of the amount of data that was corrupted and  
1953      removed from old data format files that don't contain any data quality flag.**
- 1954      • Offline-Current.csv , contains the summary of the currents and voltages applied on each  
1955      RPC HV channel.**
- 1956      • Offline-L0-EffC1.csv , is used to write the efficiencies, cluster size and cluster multiplicity  
1957      of efficiency runs. Note that L0 refers here to *Level 0* and means that the results of efficiency and  
1958      clusterization are a first approximation calculated without performing any muon tracking in**

1959 between the different detectors. This offline tool provides the user with a preliminar calculation  
 1960 of the efficiency and of the muon event parameters. Another analysis software especially  
 1961 dedicated to muon tracking is called on selected data to retrieve the results of efficiency and  
 1962 muon clusterization using a tracking algorithm to discriminate noise or gamma from muons  
 1963 as muons are the only particles that pass through the full setup, leaving hits than can be used  
 1964 to reconstruct their tracks.

- 1965     ● `Offline-Rate.csv`, is used to write the noise or gamma rates measured in the detector readout  
 1966 partitions.

1967     Note that these 4 CSV files are created along with their *headers* (`Offline-[...]-Header.csv`  
 1968 containing the names of each data columns) and are automatically merged together when the offline  
 1969 analysis tool is called from the webDCS, contrary to the case where the tool is runned locally from  
 1970 the terminal as the merging bash script is then not called. Thus, the resulting files, used to make  
 1971 official plots, are:

- 1972     ● `Corrupted.csv`,  
 1973     ● `Current.csv`,  
 1974     ● `L0-EffCl.csv`.  
 1975     ● `Rate.csv`.

### 1976     **B.3 Analysis inputs and information handling**

1977     The usage of the Offline Analysis tool as well as its output have been presented in the previous section.  
 1978     It is now important to dig further and start looking at the source code and the inputs necessary  
 1979 for the tool to work. Indeed, other than the raw ROOT data files that are analysed, more information  
 1980 needs to be imported inside of the program to perform the analysis such as the description of the  
 1981 setup inside of GIFT++ at the time of data taking (number of trolleys, of RPCs, dimensions of the  
 1982 detectors, etc...) or the mapping that links the TDC channels to the coresponding RPC channels in  
 1983 order to translate the TDC information into human readable data. 2 files are used to transmit all this  
 1984 information:  
 1985

- 1986     ● `Dimensions.ini`, that provides the necessary setup and RPC information, and  
 1987     ● `ChannelsMapping.csv`, that gives the link between the TDC and RPC channels as well as the  
 1988 *mask* for each channel (masked or not?).

#### 1989     **B.3.1 Dimensions file and InFile parser**

1990     This input file, present in every data folder, allows the analysis tool to know of the number of active  
 1991 trolleys, the number of active RPCs in those trolleys, and the details about each RPCs such as  
 1992 the number of RPC gaps, the number of pseudo-rapidity partitions (for CMS-like prototypes), the  
 1993 number of strips per partion or the dimensions. To do so, there are 3 types of groups in the INI file  
 1994 architecture. A first general group, appearing only once at the head of the document, gives information  
 1995 about the number of active trolleys as well as their IDs, as presented in Source Code B.1. For

1996 each active trolley, a group similar to Source Code B.2 can be found containing information about  
 1997 the number of active detectors in the trolley and their IDs. Each trolley group as a `Tt` name format,  
 1998 where `t` is the trolley ID. Finally, for each detector stored in slots of an active trolley, there is a group  
 1999 providing information about their names and dimensions, as shown in Source Code B.3. Each slot  
 2000 group as a `TtSs` name format, where `s` is the slot ID of trolley `t` where the active RPC is hosted.

```
2001 [General]
2002 nTrolleys=2
  TrolleysID=13
```

2003 *Source Code B.1: Example of `[General]` group as might be found in `Dimensions.ini`. In Gif++, only 2 trolleys are available to hold RPCs and place them inside of the bunker for irradiation. The IDs of the trolleys are written in a single string as "13" and then read character by character by the program.*

```
2004 [T1]
  nSlots=4
  SlotsID=1234
```

2005 *Source Code B.2: Example of trolley group as might be found in `Dimensions.ini`. In this example, the file tells that there are 4 detectors placed in the holding slots of the trolley `T1` and that their IDs, written as a single string variable, are 1, 2, 3 and 4.*

```
2006 [T1S1]
  Name=RE2-2-NPD-BARC-8
  Partitions=3
  Gaps=3
  Gap1=BOT
  Gap2=TN
  Gap3=TW
  AreaGap1=11694.25
  AreaGap2=6432
  AreaGap3=4582.82
  Strips=32
  ActiveArea-A=157.8
  ActiveArea-B=121.69
  ActiveArea-C=93.03
```

2007 *Source Code B.3: Example of slot group as might be found in `Dimensions.ini`. In this example, the file provides information about a detector named `RE2-2-NPD-BARC-8`, having 3 pseudo-rapidity readout partitions and stored in slot `S1` of trolley `T1`. This is a CMS RE2-2 type of detector. This information will then be used for example to compute the rate per unit area calculation.*

2008 This information is readout and stored in a C++ object called `IniFile`, that parses the information  
 2009 in the INI input file and stores it into a local buffer for later use. This INI parser is the exact same  
 2010 one that was previously developed for the Gif++ DAQ and described in Appendix A.5.2.

### 2011 **B.3.2 TDC to RPC link file and Mapping**

2012 The same way the INI dimension file information is stored using `map`, the channel mapping and mask  
 2013 information is stored and accessed through `map`. First of all, the mapping CSV file is organised into  
 2014 3 columns separated by tabulations (and not by commas, as expected for CSV files as it is easier using  
 2015 streams to read tab or space separated data using C++):  
 2016

2017      `RPC_channel`      `TDC_channel`      `mask`

2018      using as formatting for each field:

2019

2020      `TSCCC`      `TCCC`      `M`

2021 `TSCCC` is a 5-digit integer where `T` is the trolley ID, `s` the slot ID in which the RPC is held insite  
 2022 the trolley `T` and `ccc` is the RPC channel number, or *strip* number, that can take values up to  
 2023 3-digits depending on the detector,

2024 `TCCC` is a 4 digit integer where `T` is the TDC ID, `ccc` is the TDC channel number that can take values  
 2025 in between 0 and 127, and

2026 `M` is a 1-digit integer indicating if the channel should be considered (`M = 1`) or discarded (`M = 0`)  
 2027 during analysis.

2028      This mapping and masking information is readout and stored thanks to the object `Mapping`, pre-  
 2029      sented in Source Code B.4. Similarly to `IniFile` objects, this class has private methods. The first  
 2030      one, `Mapping::CheckIfNewLine()` is used to find the newline character '`\n`' or return character  
 2031      '`\r`' (depending on which kind of operating system interacted with the file). This is used for the  
 2032      simple reason that the masking information has been introduced only during the year 2017 but the  
 2033      channel mapping files exist since 2015 and the very beginning of data taking at GIF++. This means  
 2034      that in the older data folders, before the upgrade, the channel mapping file only had 2 columns, the  
 2035      RPC channel and the TDC channel. For compatibility reasons, this method helps controling the  
 2036      character following the readout of the 2 first fields of a line. In case any end of line character is  
 2037      found, no mask information is present in the file and the default `M = 1` is used. On the contrary, if  
 2038      the next character was a tabulation or a space, the mask information is present.

2039      Once the 3 fields have been readout, the second private method `Mapping::CheckIfTDCCh()` is  
 2040      used to control that the TDC channel is an existing TDC channel. Finally, the information is stored  
 2041      into 3 different maps (`Link`, `ReverseLink` and `Mask`) thanks to the public method `Mapping::Read()`.  
 2042      `Link` allows to get the RPC channel by knowing the TDC channel while `ReverseLink` does the op-  
 2043      posite by returning the TDC channel by knowing the RPC channel. Finally, `Mask` returns the mask  
 2044      associated to a given RPC channel.

```

2045 typedef map<Uint,Uint> MappingData;

2046 class Mapping {
2047     private:
2048         bool          CheckIfNewLine(char next);
2049         bool          CheckIfTDCCh(Uint channel);
2050         string        FileName;
2051         MappingData  Link;
2052         MappingData  ReverseLink;
2053         MappingData  Mask;
2054         int           Error;
2055
2056     public:
2057         Mapping();
2058         Mapping(string baseName);
2059         ~Mapping();
2060
2061         void SetFileName(const string filename);
2062         int  Read();
2063         Uint GetLink(Uint tdcchannel);
2064         Uint GetReverse(Uint rpcchannel);
2065         Uint GetMask(Uint rpcchannel);
2066     };

```

2047 *Source Code B.4: Description of C++ object Mapping used as a parser for the channel mapping and mask file.*

## 2048 B.4 Description of GIF++ setup within the Offline Analysis tool

2049 In the previous section, the tool input files have been discussed. The dimension file information is  
 2050 stored in a map hosted by the `IniFile` object. But this information is then used to create a series of  
 2051 new objects that helps defining the GIF++ infrastructure directly into the Offline Analysis. Indeed,  
 2052 from the `RPC`, to the more general `Infrastructure`, every element of the GIF++ infrastrucutre is  
 2053 recreated for each data analysis based on the information provided in input. All this information  
 2054 about the infrastructure will be used to assign each hit signal to a specific strip channel of a specific  
 2055 detector, and having a specific active area. This way, rate per unit area calculation is possible.  
 2056

### 2057 B.4.1 RPC objects

2058 `RPC` objects have been developped to represent physical active detectors in GIF++ at the moment  
 2059 of data taking. Thus, there are as many `RPC` objects created during the analysis than there were  
 2060 active `RPCs` tested during a run. Each `RPC` hosts the information present in the corresponding INI  
 2061 slot group, as shown in B.3, and organises it using a similar architecture. This can be seen from  
 2062 `Source Code B.5`.

2063 To make the object more compact, the lists of gap labels, of gap active areas and strip active  
 2064 areas are stored into `vector` dynamical containers. `RPC` objects are always contructed thanks to the  
 2065 dimension file information stored into the `IniFILE` and their ID, using the format `TtSs`. Using the  
 2066 `RPC` ID, the constructor calls the methods of `IniFILE` to initialise the `RPC`. The other constructors  
 2067 are not used but exist in case of need. Finally, some getters have been written to access the different  
 2068 private parameters storing the detector information.

```

2069 class RPC{
2070     private:
2071         string      name;           //RPC name as in webDCS database
2072         Uint        nGaps;          //Number of gaps in the RPC
2073         Uint        nPartitions;    //Number of partitions in the RPC
2074         Uint        nStrips;        //Number of strips per partition
2075         vector<string> gaps;       //List of gap labels (BOT, TOP, etc...)
2076         vector<float>  gapGeo;        //List of gap active areas
2077         vector<float>  stripGeo;      //List of strip active areas
2078
2079     public:
2080         RPC();
2081         RPC(string ID, IniFile* geofile);
2082         RPC(const RPC& other);
2083         ~RPC();
2084         RPC& operator=(const RPC& other);
2085
2086         string GetName();
2087         Uint GetNGaps();
2088         Uint GetNPartitions();
2089         Uint GetNStrips();
2090         string GetGap(Uint g);
2091         float GetGapGeo(Uint g);
2092         float GetStripGeo(Uint p);
2093     };

```

2071 *Source Code B.5: Description of C++ objects RPC that describe each active detectors used during data taking.*

## 2072 B.4.2 Trolley objects

2073 Trolley objects have been developped to represent physical active trolleys in GIFT++ at the moment  
 2074 of data taking. Thus, there are as many trolley objects created during the analysis than there were  
 2075 active trolleys hosting tested RPCs during a run. Each Trolley hosts the information present in the  
 2076 corresponding INI trolley group, as shown in B.2, and organises it using a similar architecture. In  
 2077 addition to the information hosted in the INI file, these object have a dynamical container of RPC  
 2078 objects, representing the active detectors the active trolley was hosting at the time of data taking.  
 2079 This can been seen from Source Code B.6.

2080 Trolley objects are always contructed thanks to the dimension file information stored into the  
 2081 IniFILE and their ID, using the format Tt. Using the Trolley ID, the constructor calls the methods  
 2082 of IniFILE to initialise the Trolley. Retrieving the information of the RPC IDs via SlotsID, a new  
 2083 RPC is constructed and added to the container RPCs for each character in the ID string. The other  
 2084 constructors are not used but exist in case of need. Finally, some getters have been written to access  
 2085 the different private parameters storing the trolley and detectors information.

```

2086
class Trolley{
    private:
        Uint          nSlots; //Number of active RPCs in the considered trolley
        string        SlotsID; //Active RPC IDs written into a string
        vector<RPC*> RPCs;   //List of active RPCs

    public:
        //Constructors, destructor and operator =
        Trolley();
        Trolley(string ID, IniFile* geofile);
        Trolley(const Trolley& other);
        ~Trolley();
        Trolley& operator=(const Trolley& other);

        //Get GIFTrolley members
        Uint  GetNSlots();
        string GetSlotsID();
        Uint   GetSlotID(Uint s);

        //Manage RPC list
        RPC*  GetRPC(Uint r);
        void  DeleteRPC(Uint r);

        //Methods to get members of RPC objects stored in RPCs
        string GetName(Uint r);
        Uint   GetNGaps(Uint r);
        Uint   GetNPartitions(Uint r);
        Uint   GetNStrips(Uint r);
        string GetGap(Uint r, Uint g);
        float  GetGapGeo(Uint r, Uint g);
        float  GetStripGeo(Uint r, Uint p);
    };

```

*Source Code B.6: Description of C++ objects `Trolley` that describe each active trolley used during data taking.*

### 2089    B.4.3 Infrastructure object

2090    The `Infrastructure` object has been developped to represent the GIFT++ bunker area dedicated to  
 2091    CMS RPC experiments. With this very specific object, all the information about the CMS RPC  
 2092    setup within GIFT++ at the moment of data taking is stored. It hosts the information present in the  
 2093    corresponding INI general group, as shown in B.1, and organises it using a similar architecture. In  
 2094    addition to the information hosted in the INI file, this object have a dynamical container of `Trolley`  
 2095    objects, representing the active tolleys in GIFT++ area. This can be seen from Source Code B.7.

2096    The `Infrastructure` object is always contructed thanks to the dimension file information stored  
 2097    into the `IniFILE`. Retrieving the information of the trolley IDs via `TrolleysID`, a new `Trolley` is  
 2098    constructed and added to the container `Trolleys` for each character in the ID `string`. By extension,  
 2099    it is easy to understand that the process described in Section B.4.2 for the construction of RPCs  
 2100    takes place when a trolley is constructed. The other constructors are not used but exist in case of  
 2101    need. Finally, some getters have been written to access the different private parameters storing the  
 2102    infrastructure, tolleys and detectors information.

```

2103
class Infrastructure {
    private:
        Uint             nTrolleys;   //Number of active Trolleys in the run
        string          TrolleysID; //Active trolley IDs written into a string
        vector<Trolley*> Trolleys; //List of active Trolleys (struct)

    public:
        //Constructors and destructor
        Infrastructure();
        Infrastructure(IniFile* geofile);
        Infrastructure(const Infrastructure& other);
        ~Infrastructure();
        Infrastructure& operator=(const Infrastructure& other);

        //Get Infrastructure members
        Uint  GetNTrolleys();
        string GetTrolleysID();
        Uint  GetTrolleyID(Uint t);

2104
        //Manage Trolleys
        Trolley* GetTrolley(Uint t);
        void     DeleteTrolley(Uint t);

        //Methods to get members of GIFTrolley objects stored in Trolleys
        Uint  GetNSlots(Uint t);
        string GetSlotsID(Uint t);
        Uint  GetSlotID(Uint t, Uint s);
        RPC*  GetRPC(Uint t, Uint r);

        //Methods to get members of RPC objects stored in RPCs
        string GetName(Uint t, Uint r);
        Uint  GetNGaps(Uint t, Uint r);
        Uint  GetNPartitions(Uint t, Uint r);
        Uint  GetNStrips(Uint t, Uint r);
        string GetGap(Uint t, Uint r, Uint g);
        float  GetGapGeo(Uint t, Uint r, Uint g);
        float  GetStripGeo(Uint t, Uint r, Uint p);
    };

```

Source Code B.7: Description of C++ object *Infrastructure* that contains the full information about CMS RPC experiment in GIF++.

## 2106 B.5 Handeling of data

2107 As discussed in Appendix A.4.2, the raw data as a `TTree` architecture where every entry is related to  
 2108 a trigger signal provided by a muon or a random pulse, whether the goal of the data taking was to  
 2109 measure the performance of the detector or the noise/gamma background respectively. Each of these  
 2110 entries, referred also as events, contain a more or less full list of hits in the TDC channels to which  
 2111 the detectors are connected. To this list of hits corresponds a list of time stamps, marking the arrival  
 2112 of the hits within the TDC channel.

2113 The infrastructure of the CMS RPC experiment within GIF++ being defined, combining the  
 2114 information about the raw data with the information provided by both the mapping/mask file and the  
 2115 dimension file allows to build new physical objects that will help in computing efficiency or rates.

### 2116 B.5.1 RPC hits

2117 The raw data stored in the ROOT file as output of the GIFT++ DAQ, is readout by the analysis tool  
 2118 using the structure `RAWData` presented in Source Code B.9 that differs from the structure presented  
 2119 in Appendix A.4.2 as it is not meant to hold all of the data contained in the ROOT file. In this sense,  
 2120 this structure is in the case of the offline analysis tool not a dynamical object and will only be storing  
 2121 a single event contained in a single entry of the `TTree`.

```
2122
2123 class RPCHit {
2124     private:
2125         Uint Channel;      //RPC channel according to mapping (5 digits)
2126         Uint Trolley;      //0, 1 or 3 (1st digit of the RPC channel)
2127         Uint Station;      //Slot where is held the RPC in Trolley (2nd digit)
2128         Uint Strip;        //Physical RPC strip where the hit occurred (last 3
2129             digits)
2130         Uint Partition;    //Readout partition along eta segmentation
2131         float TimeStamp;   //Time stamp of the arrival in TDC
2132
2133     public:
2134         //Constructors, destructor & operator =
2135         RPCHit();
2136         RPCHit(Uint channel, float time, Infrastructure* Infra);
2137         RPCHit(const RPCHit& other);
2138         ~RPCHit();
2139         RPCHit& operator=(const RPCHit& other);
2140
2141         //Get RPCHit members
2142         Uint GetChannel();
2143         Uint GetTrolley();
2144         Uint GetStation();
2145         Uint GetStrip();
2146         Uint GetPartition();
2147         float GetTime();
2148     };
2149
2150     typedef vector<RPCHit> HitList;
2151     typedef struct GIFHitList { HitList rpc[NTROLLEYS][NSLOTS][NPARTITIONS]; } →
2152         GIFHitList;
2153
2154     bool SortHitbyStrip(RPCHit h1, RPCHit h2);
2155     bool SortHitbyTime(RPCHit h1, RPCHit h2);

```

2124 *Source Code B.8: Description of C++ object RPCHit.*

```
2125
2126     struct RAWData{
2127         int iEvent;          //Event i
2128         int TDCNHits;       //Number of hits in event i
2129         int QFlag;           //Quality flag list (1 flag digit per TDC)
2130         vector<Uint> *TDCCh; //List of channels giving hits per event
2131         vector<float> *TDCTS; //List of the corresponding time stamps
2132     };

```

2126 *Source Code B.9: Description of C++ structure RAWData.*

2127 Each member of the structure is then linked to the corresponding branch of the ROOT data tree,  
 2128 as shown in the example of Source Code B.10, and using the method `GetEntry(int i)` of the ROOT  
 2129 class `TTree` will update the state of the members of `RAWData`.

```

2130 TTree* dataTree = (TTree*)dataFile.Get("RAWData");
2131 RAWData data;
2132
2133 dataTree->SetBranchAddress("EventNumber", &data.iEvent);
2134 dataTree->SetBranchAddress("number_of_hits", &data.TDCNHits);
2135 dataTree->SetBranchAddress("Quality_flag", &data.QFlag);
2136 dataTree->SetBranchAddress("TDC_channel", &data.TDCCh);
2137 dataTree->SetBranchAddress("TDC_TimeStamp", &data.TDCTS);

```

2132       *Source Code B.10: Example of link in between RAWData and TTree.*

2133       The data is then analysed entry by entry and to each element of the TDC channel list, a `RPCHit` is  
 2134       constructed by linking each TDC channel to the corresponding RPC channel thanks to the `Mapping`  
 2135       object. The information carried by the RPC channel format allows to easily retrieve the trolley and  
 2136       slot from which the hit was recorded (see section B.3.2). Using these 2 values, the readout partition  
 2137       can be found by knowing the strip channel and comparing it with the number of partitions and strips  
 2138       per partition stored into the `Infrastructure` object.

2139       Thus `RPCHit` objects are then stored into 3D dynamical list called `GIFHitList` (Source Code B.9)  
 2140       where the 3 dimensions refer to the 3 layers of the readout in `GIF++` : in the bunker there are *trolleys*  
 2141       ( $\tau$ ) holding detectors in *slots* ( $s$ ) and each detector readout is divided into 1 or more pseudo-rapidity  
 2142       *partitions* ( $p$ ). Using these 3 information allows to assign an address to each readout partition and  
 2143       this address will point to a specific hit list.

2144

## 2145       **B.5.2 Clusters of hits**

2146       All the hits contained in the ROOT file have been sorted into the different hit lists through the  
 2147       `GIFHitList`. At this point, it is possible to start looking for clusters. A cluster is a group of adjacent  
 2148       strips getting hits within a time window of 25 ns. These strips are then assumed to be part of the same  
 2149       physical avalanche signal generated by a muon passing through the chamber or by the interaction of  
 2150       a gamma stopping into the electrodes of the RPCs.

2151       To keep the cluster information, `RPCCluster` objects have been defined as shown in Source  
 2152       Code B.11. Using the information of each individual `RPCHit` taken out of the hit list, it stores  
 2153       the cluster size (number of adjacent strips composing the cluster), the first and last hit, the center for  
 2154       spatial reconstruction and finally the start and stop time stamps as well as te time spread in between  
 2155       the first and last hit.

```
2156
class RPCCluster{
    private:
        Uint ClusterSize; //Size of cluster #ID
        Uint FirstStrip; //First strip of cluster #ID
        Uint LastStrip; //Last strip of cluster #ID
        float Center; //Center of cluster #ID ((first+last)/2)
        float StartStamp; //Time stamp of the earliest hit of cluster #ID
        float StopStamp; //Time stamp of the latest hit of cluster #ID
        float TimeSpread; //Time difference between earliest and latest hits
                           //of cluster #ID

    public:
        //Constructors, destructor & operator =
        RPCCluster();
        RPCCluster(HitList List, Uint cID, Uint cSize, Uint first, Uint firstID);
        RPCCluster(const RPCCluster& other);
        ~RPCCluster();
        RPCCluster& operator=(const RPCCluster& other);

        //Get Cluster members
        Uint GetID();
        Uint GetSize();
        Uint GetFirstStrip();
        Uint GetLastStrip();
        float GetCenter();
        float GetStart();
        float GetStop();
        float GetSpread();
};

typedef vector<RPCCluster> ClusterList;

//Other functions to build cluster lists out of hit lists
void BuildClusters(HitList &cluster, ClusterList &clusterList);
void Clusterization(HitList &hits, TH1 *hcSize, TH1 *hcMult);
```

*Source Code B.11: Description of C++ object cluster.*

To investigate the hit list of a given detector partition, the function `Clusterization()` defined in `include/Cluster.h` needs the hits in the list to be time sorted. This is achieved by calling function `sort()` of library `<algorithm>` using the comparator `SortHitbyTime(RPCHit h1, RPCHit h2)` defined in `include/RPCHit.h` that returns `true` if the time stamp of hit `h1` is lower than that of `h2`. A first isolation of strips is made only based on time information. All the hits within the 25 ns window are taken separately from the rest. Then, this sub-list of hits is sorted this time by ascending strip number, using this time the comparator `SortHitbyStrip(RPCHit h1, RPCHit h2)`. Finally, the groups of adjacent strips are used to construct `RPCCluster` objects that are then stored in a temporary list of clusters that is at the end of the process used to know how many clusters were reconstructed and to fill their sizes into an histogram that will allows to know the mean size of muon or gamma clusters.

## **2171 B.6 DAQ data Analysis**

All the ingredients to analyse GIF++ data have been defined. This section will focus on the different part of the analysis performed on the data, from determining the type of data the tool is dealing with

2174 to calculating the rate in each detector or reconstructing muon or gamma clusters.

### 2175 B.6.1 Determination of the run type

2176 In GIF++, both the performance of the detectors in detecting muons in an irradiated environment and  
 2177 the gamma background can be independantly measured. These corresponds to different run types  
 2178 and thus, to different TDC settings giving different data to look at.

2179

2180 In the case of performance measurements, the trigger for data taking is provided by the coïncidence  
 2181 of several scintillators when muons from the beam passing through the area are detected. Data  
 2182 is collected in a 600 ns wide window around the arrival of muons in the RPCs. The expected time  
 2183 distribution of hits is shown in Figure B.1a. The muon peak is clearly visible in the center of the  
 2184 distribution and is to be extracted from the gamma background that composes the flat part of the  
 2185 distribution.

2186 On the other hand, gamma background or noise measurements are focussed on the non muon  
 2187 related physics and the trigger needs to be independant from the muons to give a good measurement  
 2188 of the gamma/noise distribution as seen by the detectors. The trigger is then provided by a pulse  
 2189 generator at a frequency of 300 Hz whose pulse is not likely to be on time with a muon. In order  
 2190 to increase the integrated time without increasing the acquisition time too much, the width of the  
 2191 acquisition windows are increased to 10  $\mu$ s. The time distribution of the hits is expected to be flat, as  
 2192 shown by Figure B.1b.

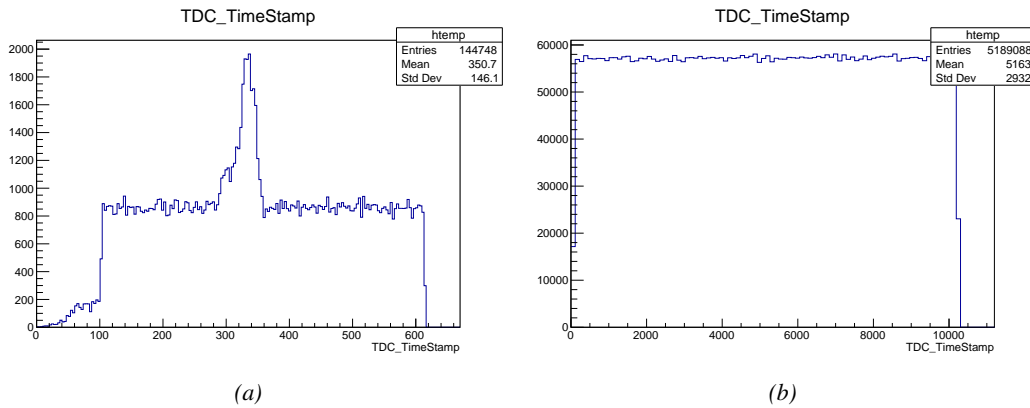


Figure B.1: Example of expected hit time distributions in the cases of efficiency (Figure B.1a) and noise/gamma rate per unit area (Figure B.1b) measurements as extracted from the raw ROOT files. The unit along the x-axis corresponds to ns. The fact that "the" muon peak is not well defined in Figure B.1a is due to the contribution of all the RPCs being tested at the same time that don't necessarily have the same signal arrival time. Each individual peak can have an offset with the ones of other detectors. The inconsistency in the first 100 ns of both time distributions is an artefact of the TDCs and are systematically rejected during the analysis.

2193 The ROOT files include a TTree called RunParameters containing, among other things, the in-  
 2194 formation related to the type of run. The run type can then be accessed as described by Source  
 2195 Code B.12 and the function IsEfficiencyRun() is then used to determine if the run file is an effi-  
 2196 ciency run or, on the contrary, another type of run (noise or gamma measurement).

```

2197     TTree* RunParameters = (TTree*)dataFile.Get("RunParameters");
2198     TString* RunType = new TString();
2199     RunParameters->SetBranchAddress("RunType", &RunType);
2200     RunParameters->GetEntry(0);

```

2199       *Source Code B.12: Access to the run type contained in TTree\* RunParameters.*

2200       Finally, the data files will have a slightly different content whether it was collected before or after  
 2201 October 2017 and the upgrade of the DAQ software that brought a new information into the ROOT  
 2202 output. This is discussed in Appendix A.4.3 and implies that the analysis will differ a little depending  
 2203 on the data format. Indeed, as no information on the data quality is stored, in older data files, the cor-  
 2204 rections for missing events has to be done at the end of the analysis. The information about the type  
 2205 of data format is stored in the variable **bool** `isNewFormat` by checking the list of branches contained  
 2206 in the data tree via the methods `TTree::GetListOfBranches()` and `TCollection::Contains()`.

## 2207       **B.6.2 Beam time window calculation for efficiency runs**

2208       Knowing the run type is important first of all to know the width of the acquisition window to be used  
 2209 for the rate calculation and finally to be able to seek for muons. Indeed, the peak that appears in the  
 2210 time distribution for each detectors is then fitted to extract the most probable time window in which  
 2211 the tool should look for muon hits. The data outside of this time window is then used to evaluate the  
 2212 noise or gamma background the detector was subjected to during the data taking. Computing the  
 2213 position of the peak is done calling the function `SetBeamWindow()` defined in file `src/RPCHit.cc` that  
 2214 loops a first time on the data. The data is first sorted in a 3D array of 1D histograms (`GIFH1Array`, see  
 2215 `include/types.h`). Then the location of the highest bin is determined using `TH1::GetMaximumBin()`  
 2216 and is used to define a window in which a gaussian fit will be applied to compute the peak width.  
 2217 This window is a 80 ns defined by Formula B.1 around the central bin.

$$t_{center}(ns) = bin \times width_{bin}(ns) \quad (\text{B.1a})$$

$$[t_{low}; t_{high}] = [t_{center} - 40; t_{center} + 40] \quad (\text{B.1b})$$

2218       Before the fit is performed, the average number of noise/gamma hits per bin is evaluated using  
 2219 the data outside of the fit window. Excluding the first 100 ns, the average number of hits per bin  
 2220 due to the noise or gamma is defined by Formula B.2 after extracting the amount of hits in the time  
 2221 windows  $[100; t_{low}]$  and  $[t_{high}; 600]$  thanks to the method `TH1::Integral()`. This average number  
 2222 of hits is then subtracted to every bin of the 1D histogram, in order to *clean* it from the noise or  
 2223 gamma contribution as much as possible to improve the fit quality. Bins where  $\langle n_{hits} \rangle$  is greater  
 2224 than the actual bin content are set to 0.

$$\Delta t_{noise}(ns) = 600 \overbrace{-t_{high} + t_{low}}^{-80ns} - 100 = 420ns \quad (\text{B.2a})$$

$$\langle n_{hits} \rangle = width_{bin}(ns) \times \frac{\sum_{t=100}^{t_{low}} + \sum_{t=t_{high}}^{600}}{\Delta t_{noise}(ns)} \quad (\text{B.2b})$$

2225       Finally, the fit parameters are extracted and saved for each detector in 3D arrays of **float**  
 2226 (`muonPeak`, see `include/types.h`), a first one for the mean arrival time of the muons, `PeakTime`,

2227 and a second one for the width of the peak, `PeakWidth`. The width is defined as  $6\sigma$  of the gaussian  
 2228 fit. The same settings are applied to every partitions of the same detector. To determine which one  
 2229 of the detector's partitions is directly illuminated by the beam, the peak height of each partition is  
 2230 compared and the highest one is then used to define the peak settings.

### 2231 **B.6.3 Data loop and histogram filling**

2232 3D arrays of histogram are created to store the data and display it on the DQM of GIF++ webDCS  
 2233 for the use of shifters. These histograms, presented in section B.2.1.1, are filled while looping on  
 2234 the data. Before starting the analysis loop, it is necessary to control the entry quality for the new  
 2235 file formats featuring `QFlag`. If the `QFlag` value for this entry shows that 1 TDC or more have a  
 2236 `CORRUPTED` flag, then this event is discarded. The loss of statistics is low enough to be neglected.  
 2237 `QFlag` is controled using the function `IsCorruptedEvent()` defined in `src/utils.cc`. As explained  
 2238 in Appendix A.4.3, each digit of this integer represent a TDC flag that can be 1 or 2. Each 2 is  
 2239 the sign of a `CORRUPTED` state. Then, the data is accessed entry by entry in the ROOT `TTree` using  
 2240 `RAWData` and each hit in the hit list is assigned to a detector channel and saved in the corresponding  
 2241 histograms. In the first part of the analysis, in which the loop over the ROOT file's content is  
 2242 performed, the different steps are:

2243 **1- RPC channel assignment and control:** a check is done on the RPC channel extracted thanks  
 2244 to the mapping via the method `Mapping::GetLink()`. If the channel is not initialised and is 0, or if  
 2245 the TDC channel was greater than 5127, the hit is discarded. This means there was a problem in the  
 2246 mapping. Often a mapping problem leads to the crash of the offline tool.

2247 **2- Creation of a `RPCHit` object:** to easily get the trolley, slot and partition in which the hit has  
 2248 been assigned, this object is particularly helpful.

2249 **3- General histograms are filled:** the hit is filled into the time distribution and the general hit  
 2250 distribution histograms, and if the arrival time is within the first 100 ns, it is discarded and nothing  
 2251 else happens and the loop proceeds with the next hit in the list.

2252 **4- Multiplicity counter:** the hit multiplicity counter of the corresponding detectors incremented.

2253 **5-a- Efficiency runs - Is the hit within the peak window? :** if the peak is contained in the peak  
 2254 window previously defined in section B.6.2, the hit is filled into the beam hit profile histogram of  
 2255 the corresponding chamber, added into the list of muon hits and increments the counter of *in time*  
 2256 hits. The term *in time* here refers to the hits that are likely to be muons by arriving in the expected  
 2257 time window. If the hit is outside of the peak window, it is filled into the noise profile histogram  
 2258 of the corresponding detector, added into the list of noise/gamma hits and increments the counter of  
 2259 noise/gamma hits.

2260 **5-b- Noise/gamma rate runs - Noise histograms are filled:** the hit is filled into the noise profile  
 2261 histogram of the corresponding detector, added into the list of noise/gamma hits and increments the  
 2262 counter of noise/gamma hits.

2263

2264 After the loop on the hit list of the entry is over, the next step is to clusterize the 3D lists filled  
 2265 in the previous steps. A 3D loop is then started over the active trolley, slot and RPC partitions to  
 2266 access these objects. Each `NoiseHitList` and `MuonHitList`, in case of efficiency run, are clusterized  
 2267 as described in section B.5.2. There corresponding cluster size and multiplicity histograms are filled  
 2268 at the end of the clustering process. Then, the efficiency histogram is filled in case of efficiency run.  
 2269 The selection is simply made by checking whether the RPC detected signals in the peak window  
 2270 during this event. Nevertheless, it is useful to highlight that at this level, it is not possible yet to  
 2271 discriminate in between a muon hit and noise or gamma hit. Thus, `MuonCSize_H`, `MuonCMult_H`  
 2272 and `Efficiency0_H` are subjected to noise and gamma contamination. This contamination will be  
 2273 estimated and corrected at the moment the results will be written into output CSV files. Finally, the  
 2274 loop ends on the filling of the general hit multiplicity histogram.

#### 2275 **B.6.4 Results calculation**

2276 As mentioned in section B.2.1, the analysis of DAQ data provides the user with 3 CSV files and  
 2277 a ROOT file associated to each and every ROOT data file. The fourth CSV file is provided by the  
 2278 extraction of the CEAN main frame data monitored during data taking and will be discussed later.  
 2279 After looping on the data in the previous part of the analysis macro, the output files are created and a  
 2280 3D loop on each RPC readout partitions is started to extract the histograms parameters and compute  
 2281 the final results.

2282

##### 2283 **B.6.4.1 Rate normalisation**

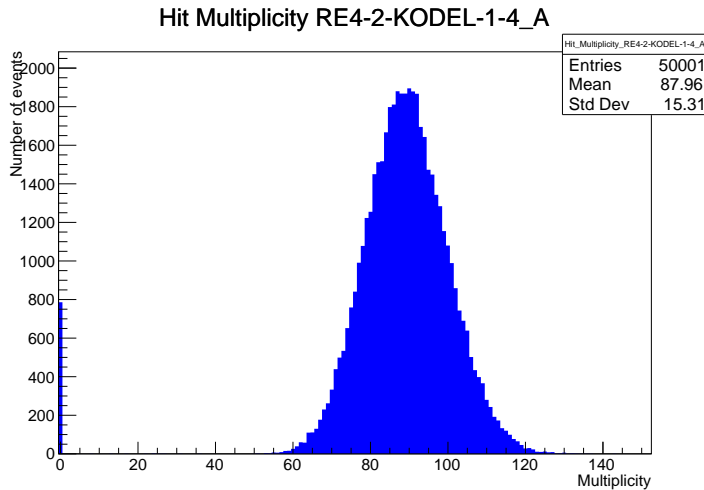


Figure B.2: The effect of the quality flag is explained by presenting the reconstructed hit multiplicity of a data file without `Quality_flag`. The artificial high content of bin 0 is the effect of corrupted data.

2284 To analyse old data format files, not containing any quality flag, it is needed to estimate the amount  
 2285 of corrupted data via a fit as the corrupted data will always fill events with a fake "0 multiplicity".  
 2286 Indeed, as no hits were stored in the DAQ ROOT files, these events artificially contribute to fill  
 2287 the bin corresponding to a null multiplicity, as shown in Figure B.2. In the case the mean of the

hit multiplicity distribution is high, the contribution of the corrupted data can easily be evaluated for later correction by comparing the level of the bin at multiplicity 0 and of a skew fit curve that should indicate a value consistent with 0. A skew fit has been chosen over a Poisson fit as it was giving better results for lower mean multiplicity values. Nevertheless, for low irradiation cases, as explained in Appendix A.4.3, the hit multiplicity distribution mean is, on the contrary, rather small and the probability to record events without hits can't be considered small anymore, leading to a difficult and non-reliable estimation of the corruption. As can be seen in Source Code B.13, conditions have been applied to prevent bad fits and wrong corruption estimation in cases where :

- The difference in between the data for multiplicity 1 and the corresponding fit value should be lower than 1% of the total amount of data :  $\frac{|n_{m=1} - sk(1)|}{N_{tot}} < 0.01$  where  $n_{m=1}$  is the number of entries with multiplicity 1,  $sk(1)$  the value of the skew fit, as defined by Formula 4.3, for multiplicity 1 and  $N_{tot}$  the total number of entries.

- The amount of data contained in the multiplicity 0 bin should not exceed 40% :  $\frac{n_{m=0}}{N_{tot}} \leq 0.4$  where  $n_{m=0}$  is the number of entries with multiplicity 0. This number has been determined to be the maximum to be able to separate the excess of data due to corruption from the hit multiplicity distribution.

Those 2 conditions need to be fulfilled to estimate the corruption of old data format files. If the fit was successful, the level of corruption is written in `Offline-Corrupted.csv` and the number of corrupted entries, refered as the integer `nEmptyEvent`, is subtracted from the total number of entries when the rate normalisation factor is computed as explicit in Source Code B.13. Note that for new data format files, the number of corrupted entries being set to 0, the definition of `rate_norm` stays valid.

```

2310
    if(!isNewFormat){
        TF1* GaussFit = new TF1("gaussfit","[0]*exp(-0.5*((x-[1])/[2])**2)",0,Xmax);
        GaussFit->SetParameter(0,100);
        GaussFit->SetParameter(1,10);
        GaussFit->SetParameter(2,1);
        HitMultiplicity_H.rpc[T][S][p]->Fit(GaussFit,"LIQR","","",0.5,Xmax);

        TF1* SkewFit = new TF1("skewfit","[0]*exp(-0.5*((x-[1])/[2])**2) / (1 +
→      exp(-[3]*(x-[4])))",0,Xmax);
        SkewFit->SetParameter(0,GaussFit->GetParameter(0));
        SkewFit->SetParameter(1,GaussFit->GetParameter(1));
        SkewFit->SetParameter(2,GaussFit->GetParameter(2));
        SkewFit->SetParameter(3,1);
        SkewFit->SetParameter(4,1);
        HitMultiplicity_H.rpc[T][S][p]->Fit(SkewFit,"LIQR","","",0.5,Xmax);

        double fitValue = SkewFit->Eval(1,0,0,0);
        double dataValue = (double)HitMultiplicity_H.rpc[T][S][p]->GetBinContent(2);
        double difference = TMath::Abs(dataValue - fitValue);
        double fitTOdataVSentries_ratio = difference / (double)nEntries;
        bool isFitGOOD = fitTOdataVSentries_ratio < 0.01;

2311
        double nSinglehit = (double)HitMultiplicity_H.rpc[T][S][p]->GetBinContent(1);
        double lowMultRatio = nSinglehit / (double)nEntries;
        bool isMultLOW = lowMultRatio > 0.4;

        if(isFitGOOD && !isMultLOW){
            nEmptyEvent = HitMultiplicity_H.rpc[T][S][p]->GetBinContent(1);
            nPhysics = (int)SkewFit->Eval(0,0,0,0);
            if(nPhysics < nEmptyEvent)
                nEmptyEvent = nEmptyEvent-nPhysics;
        }
    }

    double corrupt_ratio = 100.*(double)nEmptyEvent / (double)nEntries;
    outputCorrCSV << corrupt_ratio << '\t';

    float rate_norm = 0.;
    float stripArea = GIFIInfra->GetStripGeo(tr,sl,p);

    if(IsEfficiencyRun(RunType)){
        float noiseWindow = BMTDCWINDOW - TIMEREJECT - 2*PeakWidth.rpc[T][S][p];
        rate_norm = (nEntries-nEmptyEvent)*noiseWindow*1e-9*stripArea;
    } else
        rate_norm = (nEntries-nEmptyEvent)*RDMNOISEWDW*1e-9*stripArea;

```

*Source Code B.13: Definition of the rate normalisation variable. It takes into account the number of non corrupted entries and the time window used for noise calculation, to estimate the total integrated time, and the strip active area to express the result as rate per unit area.*

#### 2313 B.6.4.2 Rate and activity

2314 At this point, the strip rate histograms, StripNoiseProfile\_H.rpc[T][S][p], only contain an in-  
 2315 formation about the total number of noise or rate hits each channel received during the data taking.  
 2316 As described in Source Code B.14, a loop on the strip channels will be used to normalise the content  
 2317 of the rate distribution histogram for each detector partitions. The initial number of hits recorded for  
 2318 a given bin will be extracted and 2 values will be computed:

- 2319     ● the strip rate, defined as the number of hits recorded in the bin normalised like described in  
 2320       the previous section, using the variable `rate_norm`, and

- 2321     ● the strip activity, defined as the number of hits recorded in the bin normalised to the average  
 2322       number of hits per bin contained in the partition histogram, using the variable `averageNhit`.  
 2323       This value provides an information on the homogeneity of the detector response to the gamma  
 2324       background or of the detector noise. An activity of 1 corresponds to an average response.  
 2325       Above 1, the channel is more active than the average and bellow 1, the channel is less active.

```

int nNoise = StripNoiseProfile_H.rpc[T][S][p]->GetEntries();
float averageNhit = (nNoise>0) ? (float)(nNoise/nStripsPart) : 1.;

for(Uint st = 1; st <= nStripsPart; st++){
    float stripRate =
        StripNoiseProfile_H.rpc[T][S][p]->GetBinContent(st)/rate_norm;
    float stripAct =
        StripNoiseProfile_H.rpc[T][S][p]->GetBinContent(st)/averageNhit;

    StripNoiseProfile_H.rpc[T][S][p]->SetBinContent(st,stripRate);
    StripActivity_H.rpc[T][S][p]->SetBinContent(st,stripAct);
}

```

2327 *Source Code B.14: Description of the loop that allows to set the content of each strip rate and strip activity  
 channel for each detector partition.*

2328     On each detector partitions, which are readout by a single FEE, all the channels are not processed  
 2329     by the same chip. Each chip can give a different noise response and thus, histograms using a chip  
 2330     binning are used to investigate chip related noise behaviours. The average values of the strip rate  
 2331     or activity grouped into a given chip are extracted using the using the function `GetChipBin()` and  
 2332     stored in dedicated histograms as described in Source Codes B.15 and B.16 respectively.

```

float GetChipBin(TH1* H, Uint chip){
    Uint start = 1 + chip*NSTRIPSCHIP;
    int nActive = NSTRIPSCHIP;
    float mean = 0.;

    for(Uint b = start; b <= (chip+1)*NSTRIPSCHIP; b++){
        float value = H->GetBinContent(b);
        mean += value;
        if(value == 0.) nActive--;
    }

    if(nActive != 0) mean /= (float)nActive;
    else mean = 0.;

    return mean;
}

```

2335 *Source Code B.15: Function used to compute the content of a bin for an histogram using chip binning.*

```

2336   for(UInt ch = 0; ch < (nStripsPart/NSTRIPSCHIP); ch++) {
2337     ChipMeanNoiseProf_H.rpc[T][S][p]->
2338       SetBinContent(ch+1,GetChipBin(StripNoiseProfile_H.rpc[T][S][p],ch));
2339     ChipActivity_H.rpc[T][S][p]->
2340       SetBinContent(ch+1,GetChipBin(StripActivity_H.rpc[T][S][p],ch));
2341   }

```

*Source Code B.16: Description of the loop that allows to set the content of each chip rate and chip activity bins for each detector partition knowing the information contained in the corresponding strip distribution histograms.*

The activity variable is used to evaluate the homogeneity of the detector response to background or of the detector noise. The homogeneity  $h_p$  of each detector partition can be evaluated using the formula  $h_p = \exp(-\sigma_p^R / \langle R \rangle_p)$ , where  $\langle R \rangle_p$  is the partition mean rate and  $\sigma_p^R$  is the rate standard deviation calculated over the partition channels. The more homogeneously the rates are distributed and the smaller will  $\sigma_p^R$  be, and the closer to 1 will  $h_p$  get. On the contrary, if the standard deviation of the channel's rates is large,  $h_p$  will rapidly get to 0. This value is saved into histograms as shown in Source Code B.17 and could in the future be used to monitor through time, once extracted, the evolution of every partition homogeneity. This could be of great help to understand the apparition of eventual hot spots due to ageing of the chambers subjected to high radiation levels. The monitored homogeneity information could then be combined with a monitoring of the activity of each individual channel in order to have a finer information. Monitoring tools have been suggested and need to be developed for this purpose.

```

2348
2349
2350   float MeanPartSDev = GetTH1StdDev(StripNoiseProfile_H.rpc[T][S][p]);
2351   float strip_homog = (MeanPartRate==0)
2352     ? 0.
2353     : exp(-MeanPartSDev/MeanPartRate);
2354   StripHomogeneity_H.rpc[T][S][p]->Fill("exp -#left(#frac{\#sigma_{Strip}
2355     \rightarrow Rate}{\#mu_{Strip Rate}}\#right)",strip_homog);
2356   StripHomogeneity_H.rpc[T][S][p]->GetYaxis()->SetRangeUser(0.,1.);
2357
2358   float ChipStDevMean = GetTH1StdDev(ChipMeanNoiseProf_H.rpc[T][S][p]);
2359   float chip_homog = (MeanPartRate==0)
2360     ? 0.
2361     : exp(-ChipStDevMean/MeanPartRate);
2362   ChipHomogeneity_H.rpc[T][S][p]->Fill("exp -#left(#frac{\#sigma_{Chip}
2363     \rightarrow Rate}{\#mu_{Chip Rate}}\#right)",chip_homog);
2364   ChipHomogeneity_H.rpc[T][S][p]->GetYaxis()->SetRangeUser(0.,1.);

```

*Source Code B.17: Storage of the homogeneity into dedicated histograms.*

### B.6.4.3 Strip masking tool

The offline tool is automatically called at the end of each data taking to analyse the data and offer the shifter DQM histograms to control the data quality. After the histograms have been published online in the DQM page, the shifter can decide to mask noisy or dead channels that will contribute to bias the final rate calculation by editing the mask column of `ChannelsMapping.csv` as can be seen in Figure B.3.

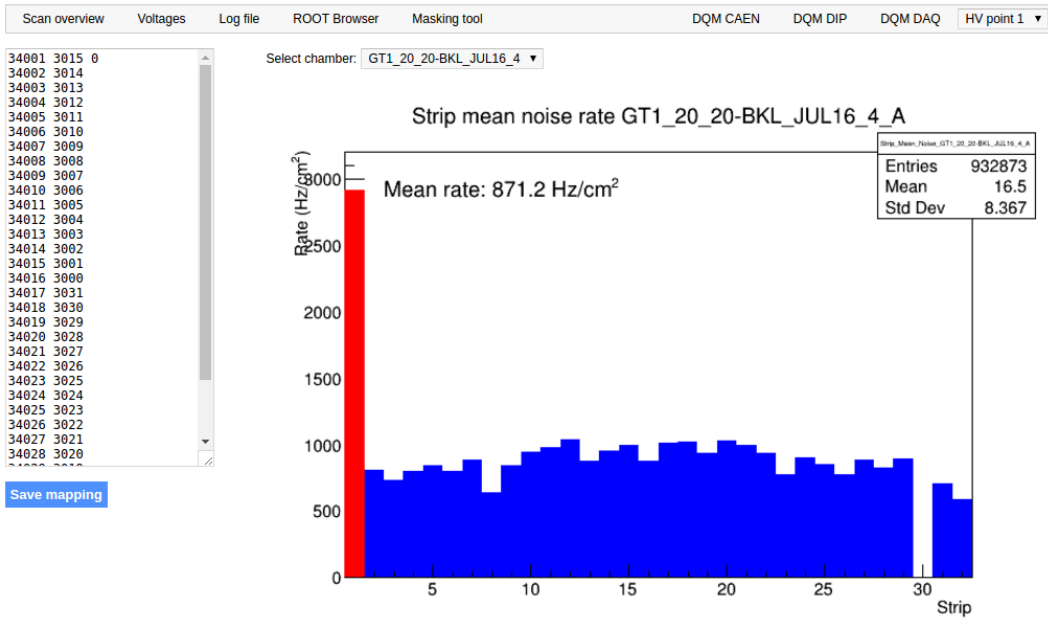


*Figure B.3: Display of the masking tool page on the webDCS. The window on the left allows the shifter to edit ChannelsMapping.csv. To mask a channel, it only is needed to set the 3rd field corresponding to the strip to mask to 0. It is not necessary for older mapping file formats to add a 1 for each strip that is not masked as the code is versatile and the default behaviour is to consider missing mask fields as active strips. The effect of the mask is directly visible for noisy channels as the corresponding bin turns red. The global effect of masking strips will be an update of the rate value showed on the histogram that will take into consideration the rejected channels.*

2359        From the code point of view, the function `GetTH1Mean()` is used to retrieve the mean rate par-  
 2360        tition by partition after the rates have been calculated strip by strip and filled into the histograms  
 2361        `StripNoiseProfile_H.rpc[T][S][p]`, as described through Source Code B.18.

2362        Once the mask for each rejected channel has been updated, the shifter can manually run the of-  
 2363        fline tool again to update the DQM plots, now including the masked strips, as well the rate results  
 2364        written in the output CSV file `Offline-Rate.csv`. If not done during the shifts, the strip masking  
 2365        procedure needs to be carefully done by the person in charge of data analysis on the scans that were  
 2366        selected to produce the final results.

2367

```

float GetTH1Mean(TH1* H) {
    int nBins = H->GetNbinsX();
    int nActive = nBins;
    float mean = 0.;

    for(int b = 1; b <= nBins; b++) {
        float value = H->GetBinContent(b);
        mean += value;
        if(value == 0.) nActive--;
    }

    if(nActive != 0) mean /= (float)nActive;
    else mean = 0.;

    return mean;
}

```

2368

*Source Code B.18: The function `GetTH1Mean()` is used to return the mean along the y-axis of `TH1` histograms containing rate information. In order to take into account masked strips whose rate is set to 0, the function looks for masked channels and decrement the number of active channels for each null value found.*

2370

#### B.6.4.4 Output CSV files filling

2371

All the histograms have been filled. Parameters will then be extracted from them to compute the final results that will later be used to produce plots. Once the results have been computed, the very last step of the offline macro is to write these values into the corresponding CSV outputs. Aside of the file `Offline-Corrupted.csv`, 2 CSV files are being written by the macro `offlineAnalysis()`, `Offline-Rates.csv` and `Offline-L0-EffCl.csv` that respectively contain information about noise or gamma rates, cluster size and multiplicity, and about level 0 reconstruction of the detector efficiency, muon cluster size and multiplicity. Details on the computation and file writing are respectively given in Sources Codes B.19 and B.20.

2379

**Noise/gamma background variables** are computed and written in the output file for each detector partitions. A detector average of the hit and cluster rate is also provided, as shown through Sources Code B.19. The variables that are written for each partition are:

2382

- The mean partition hit rate per unit area, `MeanPartRate`, that is extracted from the histogram `StripNoiseProfile_H` as the mean value along the y-axis, as described in section B.6.4.3. No error is recorded for the hit rate as this is considered a single measurement. No statistical error can be associated to it and the systematics are unknown.
- The mean cluster size, `cSizePart`, is extracted from the histogram `NoiseCSize_H` and it's statistical error, `cSizePartErr`, is taken to be  $2\sigma$  of the total distribution.
- The mean cluster multiplicity per trigger, `cMultPart`, is extracted from the histogram `NoiseCMult_H` and it's statistical error, `cMultPartErr`, is taken to be  $2\sigma$  of the total distribution. It is important to point to the fact that this variable gives an information that is dependent on the buffer window width used for each trigger for the calculation.
- The mean cluster rate per unit area, `ClustPartRate`, is defined as the mean hit rate normalised

2392

2393 to the mean cluster size and it's statistical error, `ClustPartRateErr`, is then obtained using the  
 2394 relative statistical error on the mean cluster size.

```

for (UInt tr = 0; tr < GIFInfra->GetNTrolleys(); tr++) {
  UInt T = GIFInfra->GetTrolleyID(tr);

  for (UInt sl = 0; sl < GIFInfra->GetNSlots(tr); sl++) {
    UInt S = GIFInfra->GetSlotID(tr,sl) - 1;

    float MeanNoiseRate = 0.;
    float ClusterRate = 0.;
    float ClusterSDev = 0.;

    for (UInt p = 0; p < GIFInfra->GetNPartitions(tr,sl); p++) {
      float MeanPartRate = GetTH1Mean(StripNoiseProfile_H.rpc[T][S][p]);
      float cSizePart = NoiseCSIZE_H.rpc[T][S][p]->GetMean();
      float cSizePartErr = (NoiseCSIZE_H.rpc[T][S][p]->GetEntries()==0)
        ? 0.
        : 2*NoiseCSIZE_H.rpc[T][S][p]->GetStdDev() /
          sqrt(NoiseCSIZE_H.rpc[T][S][p]->GetEntries());
      float cMultPart = NoiseCMult_H.rpc[T][S][p]->GetMean();
      float cMultPartErr = (NoiseCMult_H.rpc[T][S][p]->GetEntries()==0)
        ? 0.
        : 2*NoiseCMult_H.rpc[T][S][p]->GetStdDev() /
          sqrt(NoiseCMult_H.rpc[T][S][p]->GetEntries());
      float ClustPartRate = (cSizePart==0) ? 0.
        : MeanPartRate/cSizePart;
      float ClustPartRateErr = (cSizePart==0) ? 0.
        : ClustPartRate * cSizePartErr/cSizePart;

      outputRateCSV << MeanPartRate << '\t'
        << cSizePart << '\t' << cSizePartErr << '\t'
        << cMultPart << '\t' << cMultPartErr << '\t'
        << ClustPartRate << '\t' << ClustPartRateErr << '\t';

      RPCarea += stripArea * nStripsPart;
      MeanNoiseRate += MeanPartRate * stripArea * nStripsPart;
      ClusterRate += ClustPartRate * stripArea * nStripsPart;
      ClusterSDev += (cSizePart==0)
        ? 0.
        : ClusterRate*cSizePartErr/cSizePart;
    }

    MeanNoiseRate /= RPCarea;
    ClusterRate /= RPCarea;
    ClusterSDev /= RPCarea;

    outputRateCSV << MeanNoiseRate << '\t'
      << ClusterRate << '\t' << ClusterSDev << '\t';
  }
}

```

2395 *Source Code B.19: Description of rate result calculation and writing into the CSV output Offline-Rate.csv. Are saved into the file for each detector, the mean partition rate, cluster size and cluster mutiplicity, along with their errors, for each partition and as well as a detector average.*

2397 **Muon performance variables** are computed and written in the output file for each detector parti-  
 2398 tions as shown through Sources Code B.20. The variables that are written for each partition are:

- 2399     ● The muon efficiency, `eff`, extracted from the histogram `Efficiency0_H`. It is reminded that  
2400       this offline tool doesn't include any tracking algorithm to identify muons from the beam and  
2401       only relies on the hits arriving in the time window corresponding to the beam time. The con-  
2402       tent of the efficiency histogram is thus biased by the noise/gamma background contribution  
2403       into this window and is thus corrected by estimating the muon data content in the peak re-  
2404       gion knowing the noise/gamma content in the rate calculation region. Both time windows  
2405       being different, the choice was made to normalise the noise/gamma background calculation  
2406       window to it's equivalent beam window in order to have comparable values using the variable  
2407       `windowRatio`. Finally, to estimate the data ratio in the peak region, the variable `DataRatio`  
2408       is defined as the ratio in between the estimated mean cluster multiplicity of the muons in the  
2409       peak region, `MuonCM`, and of the total mean cluster multiplicity in the peak region, `PeakCM`.  
2410       `MuonCM` is itself defined as the difference in between the total mean cluster multiplicity in the  
2411       peak region and the normalised mean noise/gamma cluster multiplicity calculated outside of  
2412       the peak region. The statistical error related to the efficiency, `eff_err`, is computed using a  
2413       binomial distribution, as the efficiency measure the probability of "success" and "failure" to  
2414       detect muons.
- 2415     ● The mean muon cluster size, `MuonCS`, is calculated using the total mean cluster size and multi-  
2416       plicity in the peak region, respectively extracted from histograms `MuonCSize_H` and `MuonCMult_H`,  
2417       the noise/gamma background mean cluster size and normalised multiplicity, extracted from  
2418       `NoiseCSize_H` and `NoiseCMult_H`, and of the estimated muon cluster multiplicity `MuonCM` pre-  
2419       viously explicated. The associated statistical error, `MuonCM_err`, is calculated using the propa-  
2420       gation of errors of the mentioned variables.
- 2421     ● The mean muon cluster multiplicity in the peak region, `MuonCM`, explicated above whose sta-  
2422       tistical error, `MuonCM_err`, is the sum of statistical error associated to the total mean clus-  
2423       ter multiplicity in the peak reagion, `PeakCM_err`, and of the mean noise/gamma cluster size,  
2424       `NoiseCM_err`.

2425       In addition to these 2 CSV files, the histograms are saved in ROOT file `Scan00XXXX_HVY_Offline.root`  
2426       as explained in section B.2.1.1.

2427

```

for (UInt tr = 0; tr < GIFInfra->GetNTrolleys(); tr++) {
    UInt T = GIFInfra->GetTrolleyID(tr);
    for (UInt sl = 0; sl < GIFInfra->GetNSlots(tr); sl++) {
        UInt S = GIFInfra->GetSlotID(tr,sl) - 1;
        for (UInt p = 0; p < GIFInfra->GetNPartitions(tr,sl); p++) {
            float noiseWindow =
                BMTDCWINDOW - TIMEREJECT - 2*PeakWidth.rpc[T][S][p];
            float peakWindow = 2*PeakWidth.rpc[T][S][p];
            float windowRatio = peakWindow/noiseWindow;

            float PeakCM = MuonCMult_H.rpc[T][S][p]->GetMean();
            float PeakCS = MuonCSize_H.rpc[T][S][p]->GetMean();
            float NoiseCM = NoiseCMult_H.rpc[T][S][p]->GetMean() *windowRatio;
            float NoiseCS = NoiseCSize_H.rpc[T][S][p]->GetMean();
            float MuonCM = (PeakCM<NoiseCM) ? 0. : PeakCM-NoiseCM;
            float MuonCS = (MuonCM==0 || PeakCM*PeakCS<NoiseCM*NoiseCS)
                ? 0.
                : (PeakCM*PeakCS-NoiseCM*NoiseCS) / MuonCM;
            float PeakCM_err = (MuonCMult_H.rpc[T][S][p]->GetEntries()==0.)
                ? 0.
                : 2*MuonCMult_H.rpc[T][S][p]->GetStdDev() /
                    sqrt(MuonCMult_H.rpc[T][S][p]->GetEntries());
            float PeakCS_err = (MuonCSize_H.rpc[T][S][p]->GetEntries()==0.)
                ? 0.
                : 2*MuonCSize_H.rpc[T][S][p]->GetStdDev() /
                    sqrt(MuonCSize_H.rpc[T][S][p]->GetEntries());
            float NoiseCM_err = (NoiseCMult_H.rpc[T][S][p]->GetEntries()==0.)
                ? 0.
                : windowRatio*2*NoiseCMult_H.rpc[T][S][p]->GetStdDev() /
                    sqrt(NoiseCMult_H.rpc[T][S][p]->GetEntries());
            float NoiseCS_err = (NoiseCSize_H.rpc[T][S][p]->GetEntries()==0.)
                ? 0.
                : 2*NoiseCSize_H.rpc[T][S][p]->GetStdDev() /
                    sqrt(NoiseCSize_H.rpc[T][S][p]->GetEntries());
            float MuonCM_err = (MuonCM==0) ? 0. : PeakCM_err+NoiseCM_err;
            float MuonCS_err = (MuonCS==0 || MuonCM==0) ? 0.
                : (PeakCS*PeakCM_err + PeakCM*PeakCS_err +
                    NoiseCS*NoiseCM_err + NoiseCM*NoiseCS_err +
                    MuonCS*MuonCM_err) / MuonCM;

            float DataRatio = MuonCM/PeakCM;
            float DataRatio_err = (MuonCM==0) ? 0.
                : DataRatio*(MuonCM_err/MuonCM + PeakCM_err/PeakCM);
            float eff = DataRatio*Efficiency0_H.rpc[T][S][p]->GetMean();
            float eff_err = DataRatio*2*Efficiency0_H.rpc[T][S][p]->GetStdDev() /
                sqrt(Efficiency0_H.rpc[T][S][p]->GetEntries()) +
                Efficiency0_H.rpc[T][S][p]->GetMean()*DataRatio_err;

            outputEffCSV << eff << '\t' << eff_err << '\t'
                << MuonCS << '\t' << MuonCS_err << '\t'
                << MuonCM << '\t' << MuonCM_err << '\t';
        }
    }
}

```

2428

2429

*Source Code B.20: Description of efficiency result calculation and writing into the CSV output Offline-L0-EffCl.csv. Are saved into the file for each detector, the efficiency, corrected taking into account the background in the peak window of the time profile, muon cluster size and muon cluster multiplicity, along with their errors, for each partition and as well as a detector average.*

## 2430 B.7 Current data Analysis

2431 Detectors under test at GIF++ are connected both to a CAEN HV power supply and to a CAEN  
2432 ADC that reads the currents inside of the RPC gaps bypassing the supply cable. During data tak-  
2433 ing, the webDCS records into a ROOT file called `Scan00XXXX_HVY_CAEN.root` histograms with the  
2434 monitored parameters of both CAEN devices. Are recorded for each RPC channels (in most cases,  
2435 a channel corresponds to an RPC gap):

- 2436 • the effective voltage,  $HV_{eff}$ , set by the webDCS using the PT correction on the CAEN power  
2437 supply,
- 2438 • the applied voltage,  $HV_{app}$ , monitored by the CAEN power supply, and the statistical error  
2439 related to the variations of this value through time to follow the variation of the environmental  
2440 parameters defined as the RMS of the histogram divided by the square root of the number of  
2441 recorded points,
- 2442 • the monitored current,  $I_{mon}$ , monitored by the CAEN power supply, and the statistical error  
2443 related to the variations of this value through time to follow the variation of the environmental  
2444 parameters defined as the RMS of the histogram divided by the square root of the number of  
2445 recorded points,
- 2446 • the corresponding current density,  $J_{mon}$ , defined as the monitored current per unit area,  
2447  $J_{mon} = I_{mon}/A$ , where  $A$  is the active area of the corresponding gap,
- 2448 • the ADC current,  $I_{ADC}$ , recorded through the CAEN ADC module that monitors the dark  
2449 current in the gap itself. First of all, the resolution of such a module is better than that of  
2450 CAEN power supplies and moreover, the current is not read-out through the HV supply line  
2451 but directly at the chamber level giving the real current inside of the detector. The statistical  
2452 error is defined as the RMS of the histogram distribution divided by the square root of the  
2453 number of recorded points.

2454 Once extracted through a loop over the element of GIF++ infrastructure via the C++ macro  
2455 `GetCurrent()`, these parameters, organised in 9 columns per detector HV supply line, are written in  
2456 the output CSV file `Offline-Current.csv`. The macro can be found in the file `Current.cc`.

## References

2457

- 2458 [1] T. Massam et al. “Experimental observation of antideuteron production”. In: *Il Nuovo Cimento A* 63 (1965), pp. 10–14.
- 2459
- 2460 [2] UA1 Collaboration. “Experimental observation of isolated large transverse energy electrons with associated missing energy at  $s = 540 \text{ GeV}$ ”. In: *Physics Letters B* 122 (1983), pp. 103–116.
- 2461
- 2462
- 2463 [3] UA2 Collaboration. “Observation of single isolated electrons of high transverse momentum in events with missing transverse energy at the CERN pp collider”. In: *Physics Letters B* 122 (1983), pp. 476–485.
- 2464
- 2465
- 2466 [4] UA1 Collaboration. “Experimental observation of lepton pairs of invariant mass around  $95 \text{ GeV}/c^2$  at the CERN SPS collider”. In: *Physics Letters B* 126 (1983), pp. 398–410.
- 2467
- 2468 [5] UA2 Collaboration. “Evidence for  $Z_0 \rightarrow e^+e^-$  at the CERN pp collider”. In: *Physics Letters B* 129 (1983), pp. 130–140.
- 2469
- 2470 [6] ALEPH Collaboration. “Determination of the number of light neutrino species”. In: *Physics Letters B* 231 (1989), pp. 519–529.
- 2471
- 2472 [7] CERN, ed. (1985).
- 2473 [8] CERN, ed. (1986).
- 2474 [9] CERN, ed. (1994).
- 2475 [10] CERN, ed. (1998).
- 2476 [11] CERN, ed. (1999).
- 2477 [12] CERN. Geneva. LHC Experiments Committee. *Letter of Intent for A Large Ion Collider Experiment [ALICE]*, note = CERN-LHCC-93-016. Tech. rep. ALICE Collaboration, 1993.
- 2478
- 2479 [13] CERN. Geneva. LHC Experiments Committee. *ATLAS : technical proposal for a general-purpose pp experiment at the Large Hadron Collider at CERN*, note = CERN-LHCC-94-43. Tech. rep. ATLAS Collaboration, 1994.
- 2480
- 2481
- 2482 [14] CERN. Geneva. LHC Experiments Committee. *CMS : letter of intent by the CMS Collaboration for a general purpose detector at LHC*, note = CERN-LHCC-92-003. Tech. rep. CMS Collaboration, 1992.
- 2483
- 2484
- 2485 [15] CERN. Geneva. LHC Experiments Committee. *LHCb : letter of intent*. Tech. rep. CERN-LHCC-95-5. LHCb Collaboration, 1995.
- 2486
- 2487 [16] L. Evans and P. Bryant. “LHC Machine”. In: *JINST* 3 (2008). S08001.
- 2488
- 2489 [17] CMS Collaboration ATLAS Collaboration. “Combined Measurement of the Higgs Boson Mass in  $pp$  Collisions at  $\sqrt{s} = 7$  and  $8 \text{ TeV}$  with the ATLAS and CMS Experiments”. In: *Physical Review Letters* 114 (2015). 191803.
- 2490
- 2491 [18] LHCb Collaboration. “Observation of  $J/\psi p$  Resonances Consistent with Pentaquark States in  $\Lambda_b^0 \rightarrow J/\psi K^- p$  Decays”. In: *Physical Review Letters* 115 (2015). 072001.
- 2492

- 2493 [19] LHCb Collaboration. “Observation of  $J/\psi\phi$  Structures Consistent with Exotic States from  
2494 Amplitude Analysis of  $B^+ \rightarrow J/\psi\phi K^+$  Decays”. In: *Physical Review Letters* 118 (2017).  
2495 022003.
- 2496 [20] CERN. Geneva. *High-Luminosity Large Hadron Collider (HL-LHC) Technical Design Re-*  
2497 *port V. 0.1*. Tech. rep. CERN-2017-007-M. 2017.
- 2498 [21] CERN. Geneva. LHC Experiments Committee. *The CMS muon project : Technical Design*  
2499 *Report*. Tech. rep. CERN-LHCC-97-032. CMS Collaboration, 1997.
- 2500 [22] CERN. Geneva. LHC Experiments Committee. *Technical Proposal for the Phase-II Upgrade*  
2501 *of the CMS Detector*. Tech. rep. CERN-LHCC-2015-010. CMS Collaboration, 2015.
- 2502 [23] CERN. Geneva. LHC Experiments Committee. *CMS, the Compact Muon Solenoid : technical*  
2503 *proposal*. Tech. rep. CERN-LHCC-94-38. CMS Collaboration, 1994.
- 2504 [24] R. Santonico and R. Cardarelli. “Development of resistive plate counters”. In: *Nucl. Instr.*  
2505 *Meth. Phys. Res.* 187 (1981), pp. 377–380.
- 2506 [25] Yu.N. Pestov and G.V. Fedotovich. *A picosecond time-of-flight spectrometer for the VEPP-2M*  
2507 *based on local-discharge spark counter*. Tech. rep. SLAC-TRANS-0184. SLAC, 1978.
- 2508 [26] W.W. Ash, ed. *Spark Counter With A Localized Discharge*. Vol. SLAC-R-250. 1982, pp. 127–  
2509 131.
- 2510 [27] I. Crotty et al. “The non-spark mode and high rate operation of resistive parallel plate cham-  
2511 bers”. In: *NIMA* 337 (1993), pp. 370–381.
- 2512 [28] I. Crotty et al. “Further studies of avalanche mode operation of resistive parallel plate cham-  
2513 bers”. In: *NIMA* 346 (1994), pp. 107–113.
- 2514 [29] R. Cardarelli et al. “Avalanche and streamer mode operation of resistive plate chambers”. In:  
2515 *NIMA* 382 (1996), pp. 470–474.
- 2516 [30] E. Cerron Zeballos et al. “A new type of resistive plate chamber: The multigap RPC”. In:  
2517 *NIMA* 374 (1996), pp. 132–135.
- 2518 [31] M.C.S. Williams. “The development of the multigap resistive plate chamber”. In: *Nucl. Phys.*  
2519 *B* 61 (1998), pp. 250–257.
- 2520 [32] H. Czyrkowski et al. “New developments on resistive plate chambers for high rate operation”.  
2521 In: *NIMA* 419 (1998), pp. 490–496.
- 2522 [33] P. Camarri et al. “Streamer suppression with SF6 in RPCs operated in avalanche mode”. In:  
2523 *NIMA* 414 (1998), pp. 317–324.
- 2524 [34] E. Cerron Zeballos et al. “Effect of adding SF6 to the gas mixture in a multigap resistive plate  
2525 chamber”. In: *NIMA* 419 (1998), pp. 475–478.
- 2526 [35] CERN. Geneva. LHC Experiments Committee. *ATLAS muon spectrometer: Technical design*  
2527 *report*. Tech. rep. CERN-LHCC-97-22. ATLAS Collaboration, 1997.
- 2528 [36] CERN. Geneva. LHC Experiments Committee. *ALICE Time-Of-Flight system (TOF) : Tech-*  
2529 *nical Design Report*. Tech. rep. CERN-LHCC-2000-012. ALICE Collaboration, 2000.
- 2530 [37] The CALICE collaboration. “First results of the CALICE SDHCAL technological proto-  
2531 type”. In: *JINST* 11 (2016).
- 2532 [38] PoS, ed. *Density Imaging of Volcanoes with Atmospheric Muons using GRPCs*. International  
2533 Europhysics Conference on High Energy Physics - HEP 2011. 2011.
- 2534 [39] C. Lippmann. “Detector Physics of Resistive Plate Chambers”. PhD thesis. Johann Wolfgang  
2535 Goethe-Universität, 2003.

## BIBLIOGRAPHY

---

- 2536 [40] M. Abbrescia et al. “Properties of C<sub>2</sub>H<sub>2</sub>F<sub>4</sub>-based gas mixture for avalanche mode operation  
2537 of resistive plate chambers”. In: *NIMA* 398 (1997), pp. 173–179.
- 2538 [41] G.Battistoni et al. “Sensitivity of streamer mode to single ionization electrons”. In: *NIMA*  
2539 235 (1985), pp. 91–97.
- 2540 [42] W. Riegler. “Induced signals in resistive plate chambers”. In: *NIMA* 491 (2002), pp. 258–271.
- 2541 [43] E. Cerron Zeballos et al. “A comparison of the wide gap and narrow gap resistive plate  
2542 chamber”. In: *NIMA* 373 (1996), pp. 35–42.
- 2543 [44] M. Abbrescia et al. “Cosmic ray tests of double-gap resistive plate chambers for the CMS  
2544 experiment”. In: *NIMA* 550 (2005), pp. 116–126.
- 2545 [45] ALICE Collaboration. “A study of the multigap RPC at the gamma irradiation facility at  
2546 CERN”. In: *NIMA* 490 (2002), pp. 58–70.
- 2547 [46] B. Bonner et al. “A multigap resistive plate chamber prototype for time-of-flight for the STAR  
2548 experiment at RHIC”. In: *NIMA* 478 (2002), pp. 176–179.
- 2549 [47] S. Yang et al. “Test of high time resolution MRPC with different readout modes for the  
2550 BESIII upgrade”. In: *NIMA* 763 (2014), pp. 190–196.
- 2551 [48] A. Akindinov et al. “RPC with low-resistive phosphate glass electrodes as a candidate for  
2552 the CBM TOF”. In: *NIMA* 572 (2007), pp. 676–681.
- 2553 [49] JINST, ed. *Development of the MRPC for the TOF system of the MultiPurpose Detector.*  
2554 RPC2016: XII Workshop on Resistive Plate Chambers and Related Detectors. 2016.
- 2555 [50] M.C.S. Williams. “Particle identification using time of flight”. In: *Journal of Physics G* 39  
2556 (2012).
- 2557 [51] A. Alici et al. “Aging and rate effects of the Multigap RPC studied at the Gamma Irradiation  
2558 Facility at CERN”. In: *NIMA* 579 (2007), pp. 979–988.
- 2559 [52] M. Abbrescia et al. “The simulation of resistive plate chambers in avalanche mode: charge  
2560 spectra and efficiency”. In: *NIMA* 431 (1999), pp. 413–427.
- 2561 [53] M. Abbrescia et al. “Study of long-term performance of CMS RPC under irradiation at the  
2562 CERN GIF”. In: *NIMA* 533 (2004), pp. 102–106.
- 2563 [54] H.C. Kim et al. “Quantitative aging study with intense irradiation tests for the CMS forward  
2564 RPCs”. In: *NIMA* 602 (2009), pp. 771–774.
- 2565 [55] S. Agosteo et al. “A facility for the test of large-area muon chambers at high rates”. In: *NIMA*  
2566 452 (2000), pp. 94–104.
- 2567 [56] PoS, ed. *CERN GIF ++ : A new irradiation facility to test large-area particle detectors for*  
2568 *the high-luminosity LHC program.* Vol. TIPP2014. 2014, pp. 102–109.
- 2569 [57] A. Fagot. *GIF++ DAQ v4.0*. 2017. URL: [https://github.com/afagot/GIF\\_DAQ](https://github.com/afagot/GIF_DAQ).
- 2570 [58] CAEN. *Mod. V1190-VX1190 A/B, 128/64 Ch Multihit TDC*. 14th ed. 2016.
- 2571 [59] CAEN. *Mod. V1718 VME USB Bridge*. 9th ed. 2009.
- 2572 [60] W-Ie-Ne-R. *VME 6021-23 VXI*. 5th ed. 2016.
- 2573 [61] Wikipedia. *INI file*. 2017. URL: [https://en.wikipedia.org/wiki/INI\\_file](https://en.wikipedia.org/wiki/INI_file).
- 2574 [62] S. Carrillo A. Fagot. *GIF++ Offline Analysis v6*. 2017. URL: [https://github.com/afagot/GIF\\_OfflineAnalysis](https://github.com/afagot/GIF_OfflineAnalysis).